Terminal Control of a Variable-Stability Slender Reentry Vehicle

by

Matthew Thomas Karmondy

B.S., Aeronautical Engineering
United States Air Force Academy, 2006

Submitted to the Department of Aeronautics and Astronautics in Partial Fulfillment of the Requirements for the Degree of

MASTER OF SCIENCE
at the
MASSACHUSETTS INSTITUTE OF TECHNOLOGY June 2008

Signature of the Author .....
Department of Aeronautics and Astronautics
May 23, 2008

Certified by .....
John J. Deyst, Jr.
Professor of Aeronautics and Astronautics
Thesis Advisor

Certified by .....
Laurent Duchesne
Charles Stark Draper Laboratory Thesis Supervisor

Accepted by .....
Prof. David L. Darmofal
Associate Department Head
Chair, Committee on Graduate Students

This page intentionally left blank.

Terminal Control of a Variable-Stability Slender Reentry Vehicle

by

Matthew Thomas Karmondy

Submitted to the Department of Aeronautics and Astronautics on May 23, 2008 in Partial Fulfillment of the Requirements for the Degree of Master of Science in Aeronautics and Astronautics.

ABSTRACT

Various terminal control schemes are applied to a proposed slender reentry vehicle, controlled by two separately-articulating flaps. The flap deflections are summarized as symmetric and asymmetric flap deflections; the former manipulates the drag, lift-curve slope, and static margin; the latter controls the vehicle trim characteristics. The control problem is interesting because the static margin can be actively controlled from statically stable in pitch to statically unstable in pitch. Deflection limits on the flaps present a control saturation that must be considered in control system design. A baseline, angle of attack tracking linear-quadratic servo (LQ-servo) controller is detailed, including an analysis of actuator dynamics and a lead compensator. Desired time response characteristics and robustness to center of pressure uncertainty, reduced control effectiveness, and external pitch accelerations drive the selection of a symmetric deflection at specified points on the reentry trajectory. A hybrid switching-linear controller (SLC) is developed to reduce the peak overshoot and settling time. A saturated control drives the phase plane trajectory toward a region of satisfactory linear control, where the LQ-servo controller is properly initialized and controls the phase plane trajectory to the reference command. SLC does not provide appreciable robustness gains compared to the LQ-servo controller. A model-reference adaptive controller is described. Saturation effects prevent the adaptive controller from providing additional robustness. A method to adaptively control both the symmetric and asymmetric flap deflections is proposed.

Thesis Advisor: John J. Deyst, Jr., Professor of Aeronautics and Astronautics
Thesis Supervisor: Laurent Duchesne, C.S. Draper Laboratory

This page intentionally left blank.

Acknowledgments

It really is amazing that two years have already passed and I have a complete thesis sitting in front of me. Although I am not totally convinced my research will change the face of aerospace engineering (although all graduate students secretly hope their work will), the MIT/Draper experience was incredible. Moreover, I am indebted to everyone who helped all along the way to the final publication the 100-plus page "What I Did for Two Years in Boston." I cannot thank you all enough for your technical expertise, moral support, and constant reassurance that pilot training is not too far off.

Laurent Duchesne must be thanked first. His guidance, from the most basic classical control strategy, through the murky waters of discrete signal processing, to our vain attempts at a μ controller, was truly the cornerstone upon which I built my two years of research. Despite my relative inexperience in controls engineering, Laurent was inordinately helpful in narrowing the formidable field of "high-speed control" to a workable, Master's Degree thesis. His constant demand to ensure we really understood the problem is probably the primary reason I am pleased with my final thesis—it is not a mess of math and theory, but rather a logical (if technical) solution to an exciting problem. Naturally, the aid of Professor John Deyst must be recognized, too. From the first time I approached Professor Deyst, his excitement about the problem was contagious. His vast experience in controls was a veritable fountain of ideas that, given another 5 years, I still would never have even imagined. The degree of autonomy he provided, combined with his keen insight, helped me generate a final product of which I am proud.

The Draper staff provided such a huge measure of support, and I cannot thank them enough. Sean George and his aerodynamic knowledge at our weekly meetings helped tame the wild woods of hypersonics. My Division Leader, Dr. Brent Appleby, ensured all us Draper Fellows were set up for success from Day 1. And of course, the other fellows here. The assistance with classes, enlightened discussions about thesis work, the occasional griping followed by a moment of realization, and the "controls-free" lunches kept me sane (and kept me from failing out).

Where would I be without the other lieutenants here? Without you guys, nothing would have broken up the monotony of classes and MATLAB code. Most of all, I have got to hand it to my roommate. Living with me through the ups and downs of MIT, research, and squirrels in the wall probably qualifies you for an award...I'll work on that paperwork.

Finally, my family provided constant support (and dinner recipes). Sunday night always seemed a little less daunting knowing I would be talking to you rather than hiding from Monday's looming head.

This thesis was prepared at the Charles Stark Draper Laboratory, Inc., under Contract N00014-06-D-0171 for the Office of Naval Research.

Matthew T. Karmondy, 2d Lt, USAF
23 May 2008

Contents

This page intentionally left blank.

List of Figures

List of Tables

This page intentionally left blank.

Nomenclature

$[\alpha^c \quad q^c]^T$	centroid of unsaturated control region
α	angle of attack [rad]
$\bar{q}$	dynamic pressure [N/m^2]
δ_1	deflection of flap 1 [deg]
δ_2	deflection of flap 2 [deg]
Δ_a	excess commanded asymmetric control deflection [deg]
δ_a	asymmetric flap deflection [deg]
δ_s	symmetric flap deflection [deg]
ϵ	slope of final error integral curve [s]
Γ_I	error integral adaptation rate
γ_{air}	ratio of specific heats for air [unitless]
$\hat{\delta}_a$	commanded control deflection [deg]
$\hat{\mathbf{K}}$	adaptive state gain
$\hat{k}_I$	adaptive integrated error gain
λ	control effectiveness uncertainty
$\mathbf{\Gamma}_x$	state adaptation rate matrix
$\mathbf{A}$	open loop dynamics matrix

$\mathbf{B}$	input matrix
$\mathbf{C}$	output matrix
$\mathbf{e}$	model-reference error vector
$\mathbf{K}$	full-state feedback gain matrix
$\mathbf{Q}$	state weighting matrix
$\mathbf{R}$	control weighting matrix
$\mathbf{r}$	position vector
$\mathbf{u}$	input vector
$\mathbf{V}$	velocity vector
$\mathbf{x}$	state vector
$\mathbf{y}$	output vector
$\mathcal{L}$	Lyapunov function
μ	gravitational constant [m^3/s^2]
ω_E	rotation rate of Earth [rad/s]
ρ	atmospheric density [kg/m^3]
$\frac{X_{cg}}{l}$	normalized center of gravity location [unitless]
$\frac{X_{cp}}{l}$	normalized center of pressure location [unitless]
a	speed of sound, $\sqrt{\gamma_{\text{air}} RT}$ [m/s]
A_{ref}	reference closed-loop dynamics matrix
C_L	lift coefficient [unitless]
C_M	pitching moment coefficient [unitless]
C_D	drag coefficient [unitless]
C_{L_0}	zero-angle lift coefficient [unitless]
C_{L_α}	lift-curve slope [1/rad]

C_{M_0} zero angle pitching moment coefficient [unitless]

C_{M_α} pitch static stability derivative [1/rad]

C_{M_q} pitch damping derivative [1/rad]

D drag [N]

d_{ref} reference length [m]

e_I integrated tracking error [rad-s]

e_{I_0} initial error integral [rad-s]

e_{I_f} final error integral [rad-s]

F_g weight [N]

g gravitational acceleration [m/s^2]

gm gain margin [dB]

gm_{des} desired gain margin [dB]

L lift [N]

l vehicle length [m]

M Mach number [unitless]

m vehicle mass [kg]

m^* control switching curve slope

m_p magnitude of peak overshoot [%]

q pitch rate [rad/s]

q^* saturated control switching curve

q^s nonlinear-linear switching curve

R ideal gas constant for air [$\frac{J}{\text{kg}-\text{K}^2}$]

r reference angle of attack command [rad]

R_0 distance from center of Earth to vehicle [m]

R_e radius of Earth [m]

S_{ref} reference area [m^2]

S_{flap} effective area of flap [m^2]

SM static margin [unitless]

T air temperature [K]

t_r 10%-90% rise time [sec]

t_s 5% settling time [sec]

$t_{r_{\text{des}}}$ desired rise time [sec]

tol specified tolerance

V velocity [m/s]

x_d downrange distance [m]

Chapter 1

Background

1.1 Motivation

The advent of man-made reentry vehicles can be found in the Cold War, when tension between the Soviet Union and United States led both countries to develop ballistic missiles and manned space exploration programs. With reentry vehicle experience compounding, the technology was applied to additional pursuits: reconnaissance satellites, the Galileo Jovian atmosphere probe, numerous Martian landers. The pursuit of these systems necessitated investigation into high-Mach flow, viscous-inviscid interactions, rarefied atmospheric dynamics, high-temperature materials, and other aerospace environments previously unexplored.[1] The rigorous demands of atmospheric reentry environment often drive vehicle designs, which vary from the conical capsules of Project Mercury, Gemini, and Apollo to the winged Space Shuttle and X-15.

With recent developments in thermal-protections systems [2], previously impractical reentry vehicle shapes are now viable. This effort considers a class of slender reentry vehicles (SRVs). Depending on vehicle design parameters, the SRV may be statically stable or unstable in pitch. If the vehicle is in fact unstable, a flight control system is necessary for vehicle operation. Furthermore, a reentry flight control system permits a greater payload-delivery footprint. The SRV considered in this effort is controlled by articulating flaps rather than conventional fins or reaction motors. Control flaps are advantageous over conventional fins that project from the vehicle body when severe control surface ablation is expected. Reaction motors must carry a sufficient supply of fuel to induce moments on the vehicle over the course of the entire reentry, severely limiting payload carriage and vehicle dimensions. The difficulties with control flaps lie in their small deflection envelope and potentially reduced time response; the vehicle payload and sizing constraints also limit the flap deflections. Consequently, satisfactory time response characteristics in the face of control saturation is an important consideration in this control system development.

Various reentry guidance and control methods have been suggested and employed for both operational and proposed systems. The Gemini and Apollo capsules utilized offset centers of gravity to trim at nonzero angles of attack, while reaction motors provided limited control over the landing footprint.[1] More recently, a time-varying linear quadratic control was applied to low lift/drag reentry vehicles [3], while Dukeman applied standard linear quadratic regulator guidance scheme to the X-33.[4] Bibeau and Rubinstein discussed nonlinear trajectory and guidance planning schemes.[5] The control of some reentry vehicles, including the SRV considered in this effort, is often motivated by statically unstable systems. Sinar et al. discussed a spin-stabilized reentry controlled with dynamic inversion and proportional-integral-derivative (PID) control.[6] Winged reentry vehicles, like the reusable United States Space Shuttle and Russian Energia/Buran, are often attractive because they permit great control over landing areas. The successors to both of these systems are generally manned vehicles flown to a conventional landing on a conventional runway. An adaptive controller for the Horus winged reentry vehicle was proposed by Mooij et al.[7]

A similar, Shuttle-like winged reentry vehicle was discussed by Lu in his proposed nonlinear reference drag profile controller.[8] Shtessal et al. utilize a sliding controller for yet another reusable launch vehicle.[9] Burkhardt and Schoettle applied predictive guidance schemes to ballistic reentry vehicles controlled to specified landing sites.[10]

The historic stumbling blocks to high-speed vehicles are the "unknown-unknowns" described by Bertin.[1] While a significant amount of computational and wind tunnel tests and simulations can be conducted, high-speed flight is difficult to model, and previously unconsidered variations often become apparent. Bertin points out the Space Shuttle pitching moment was not well understood before the maiden STS-1, requiring a body flap deflection twice the value predicted during ground testing and the approach and landing flight testing. Casey points out slender reentry vehicles are susceptible to large changes in pitching moment coefficient from small ablation.[11] These difficulties motivate the need for a controller with robustness to a (potentially) poorly-modeled plant.

1.2 Research Objectives

This effort aimed to develop a controller for a variable-stability slender reentry vehicle controlled by independently articulating flaps with significant deflection limits. The vehicle has two control inputs: symmetric and asymmetric flap deflection. The former changes the drag, lift-curve slope, and static margin; the latter changes the zero-angle lift and moment coefficients (trim conditions). Various simplifications are made to reduce the scope of this thesis, speed simulation time, and provide better insight into certain challenges inherent to slender reentry vehicles. Specifically, research objectives are as follows:

- To define an operating environment for a "typical" slender reentry vehicle and select representative design points for controller design and analysis.
- To simplify vehicle aerodynamics to a two input, single output system that tracks angle of attack commands while maintaining critical nonlinearities and limitations.
- To set the symmetric deflection (and thus static margin) at specified flight conditions so performance and robustness are satisfactory.
- To design a "baseline" tracking controller using well-established control design methods to understand system performance and control difficulties.
- To design a controller that improves upon the time response and robustness of the baseline controller.
- To identify shortcomings of the system and recommend further investigation to improve robust performance of slender reentry vehicle control.

1.3 Thesis Organization

Chapter 2 defines the aerodynamic characteristics of the SRV and defines the 3 degrees of freedom for longitudinal motion of a generic unpowered vehicle in a rotating coordinate frame. The variable stability characteristics of the SRV are discussed, as are the trim angle of attack limits imposed by control surface saturation.

Chapter 3 develops a Linear Quadratic Servo (LQ-servo) controller for angle of attack reference commands. After a simplification of the dynamics, three design points are selected along the ballistic trajectory. The progression of vehicle performance as actuator dynamics and a lead compensator are added to the system is

detailed. Robustness to static margin uncertainty and reduced control effectiveness is considered. Optimal symmetric deflection control inputs are selected at each flight condition.

Chapter 4 discusses the development of a hybrid switching-linear controller (SLC) to improve upon the Linear Quadratic Servo performance. The phase plane of the linear controller is analyzed to understand the difficulty of switching between saturated controls. This phase plane analysis motivated a switch logic that toggles between commanded saturated controls and the LQ-servo controller previously developed. A method to initialize the integrated tracking error software state is also developed and implemented.

Chapter 5 details a model-reference adaptive controller. In an attempt to provide additional robustness to the SRV, an adaptive controller is designed. A dual-input adaptive controller method is proposed as a baseline for future research.

Chapter 6 draws conclusions from this research effort and suggests areas of further investigation.

This page intentionally left blank.

Chapter 2

Problem Formulation

Before the terminal control can be devised, the vehicle aerodynamics and operating environment must be sufficiently defined. To simplify final control design, only longitudinal motion is considered, resulting in a 3 degrees of freedom (3DoF) model (pitch, downrange, and altitude). The aerodynamics are defined as quasi-linear (linear for constant Mach number and control deflections) over a sufficiently small range of angles, although the reentry dynamics are certainly highly nonlinear with large variations in Mach number and geopotential altitude inherent to a high-Mach reentry profile.

2.1 Vehicle Aerodynamics Model

The slender reentry vehicle (SRV) is controlled by two separately articulating flaps on the upper and lower aft sections of the vehicle, as shown in Figure 2.1. A quasi-linear

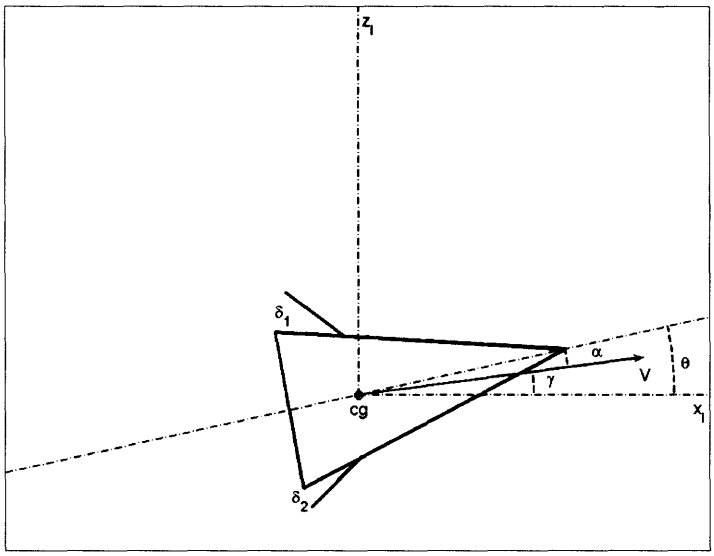

Figure 2.1: Slender reentry vehicle (not to scale)

aerodynamics model approximates the angle of attack in the range $\pm 10°$. Outside this range, the quasi-linear model is no longer assumed to be valid.

2.1.1 Control Surfaces

Each control surface, δ_1 and δ_2, can be deflected continuously in the range [0,10] degrees. These control saturations result from packaging limitations in a slender, conical reentry vehicle. Negative deflections are not possible, as this requires the control surface moving beneath the surface of the vehicle. Furthermore, maximum control deflections are limited not only by actuator range, but also by the high-Mach environment. Control deflections greater than 10 degrees may cause rapid control surface ablation. These control saturations are integral to the control system design.

Rather than express the control deflections as δ_1 and δ_2, symmetric and asymmetric control deflections are selected as the control inputs. Symmetric control deflection is assumed to affect the drag coefficient, lift-curve slope, and longitudinal static stability derivative. It is defined as

$$\delta_s = \frac{1}{2}(\delta_1 + \delta_2) \tag{2.1}$$

The asymmetric control deflection is assumed to impact the vehicle trim capabilities by changing the zero-angle-of-attack lift and pitching moment coefficients. It is defined as

$$\delta_a = \delta_2 - \delta_1 \tag{2.2}$$

From these definitions of δ_s and δ_a, the control saturation envelope is modified to that shown in Figure 2.2. Five degrees provide the maximum range of asymmetric deflection, while the minimum and maximum symmetric deflections provide no asymmetric deflection capability.

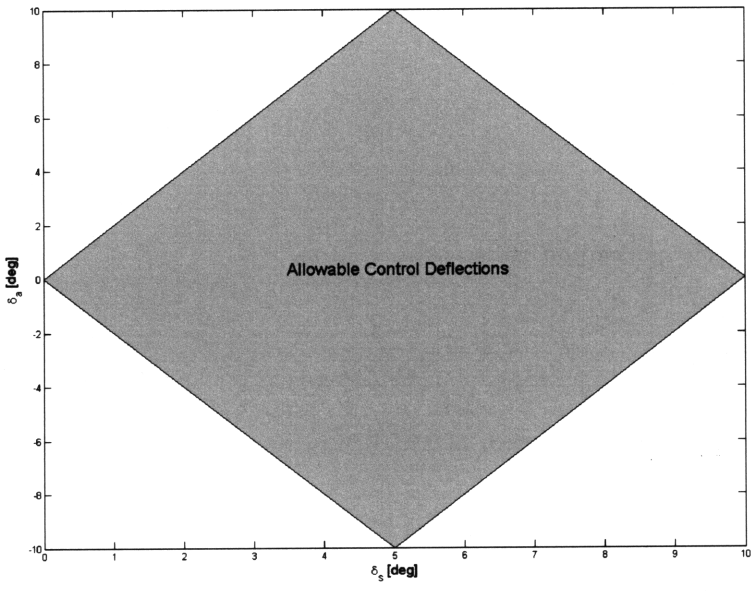

Figure 2.2: Control limits

2.1.2 Drag Coefficient

The drag coefficient, C_D, is defined as

$$C_D \triangleq \frac{D}{\frac{1}{2}\rho V^2 S_{\text{ref}}} \tag{2.3}$$

The SRV drag coefficient is a function of Mach number and the symmetric flap deflection. For Mach numbers between 3 and 8, the drag coefficient is approximated by

$$C_D = C_{D_0}(M) + C_{D_\delta}(M)\delta_s \tag{2.4}$$

Note for a constant Mach number, the drag coefficient is only affected by δ_s.

2.1.3 Lift Coefficient

The lift coefficient, C_L is defined as

$$C_L \triangleq \frac{L}{\frac{1}{2}\rho V^2 S_{\text{ref}}} \tag{2.5}$$

The SRV lift coefficient is a function of Mach number, δ_s, and δ_a as follows:

$$C_L = C_{L_0}(M, \delta_a) + C_{L_\alpha}(M, \delta_s)\alpha \tag{2.6}$$

The lift-curve slope is dependent on the symmetric flap deflection. Similar to Equation 2.4,

$$C_{L_\alpha} = C_{L_{\alpha_0}}(M) + C_{L_{\alpha_\delta}}(M)\delta_s \tag{2.7}$$

Constant Mach numbers yield a lift-curve slope that is only a function of symmetric flap deflection.

The zero-angle lift coefficient is assumed to be a function of asymmetric flap deflection at constant Mach numbers. The flap is modeled as a flat plate in supersonic flow at an angle of attack equal to δ_a. From [12], this leads to

$$C_{L_0} = \frac{4}{\sqrt{M^2 - 1}} \left(\frac{\pi}{180^\circ} \delta_a \right) \left(\frac{S_{\text{flap}}}{S_{\text{ref}}} \right) \tag{2.8}$$

where S_{flap} is the effective area of the flaps.

2.1.4 Pitching Moment Coefficient

The pitching moment, C_M, is defined as

$$C_M \triangleq \frac{M}{\frac{1}{2}\rho V^2 S_{\text{ref}} d_{\text{ref}}} \tag{2.9}$$

Similar to Equation 2.6, C_M is determined as

$$C_M = C_{M_0}(M, \delta_a) + C_{M_\alpha}(M, \delta_s)\alpha + C_{M_q}(M) q \frac{d}{2V} \tag{2.10}$$

where C_{M_q} is the pitch damping derivative. This term is strictly negative.

The ratio of pitch stability derivative and lift-curve slope is the vehicle static margin:

$$SM = -\frac{C_{M_\alpha}}{C_{L_\alpha}} \tag{2.11}$$

A positive static margin indicates static stability, while zero and negative static margins indicate neutral static stability and static instability, respectively.

The static margin is a function of Mach number as well as symmetric flap deflection, determined as

$$SM = \left[\left(\frac{X_{cp}}{l} \right)_0 (M) + \left(\frac{X_{cp}}{l} \right)_\delta (M)\delta_s - \frac{X_{cg}}{l} \right] \frac{l}{d_{\text{ref}}} \tag{2.12}$$

where l is the vehicle length and $\frac{X_{cg}}{l}$ and $\frac{X_{cp}}{l}$ are the normalized center of gravity and center of pressure locations, respectively. For a constant Mach number, increasing δ_s increases $\frac{X_{cp}}{l}$, moving the static margin from ahead of the center of gravity to behind the center of gravity (unstable to stable), as shown in Figure 2.3

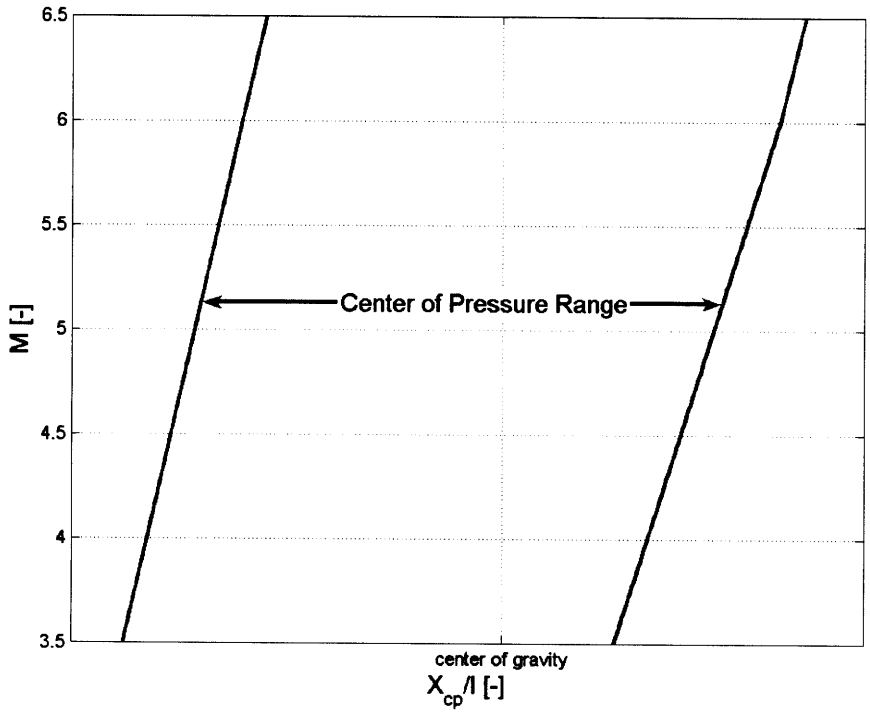

Figure 2.3: Variability in the center of pressure

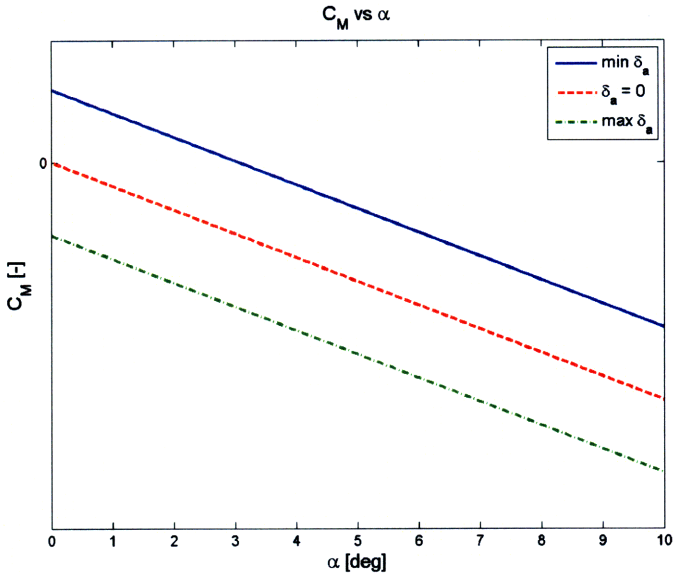

Figure 2.4: Pitching coefficient as δ_a varies, constant Mach number

Combining Equations 2.7, 2.11, and 2.12, the longitudinal static stability derivative is a quadratic function of δ_s for a constant Mach number:

$$C_{M_\alpha} = -\left[C_{L_{\alpha_0}}(M) + C_{L_{\alpha_\delta}}(M)\delta_s\right]\left[\left(\frac{X_{cp}}{l}\right)_0(M) + \right.$$
$$\left. + \left(\frac{X_{cp}}{l}\right)_\delta(M)\delta_s - \frac{X_{cg}}{l}\right]\frac{l}{d_{\text{ref}}} \tag{2.13}$$

The zero-angle pitching moment coefficient is found by applying Equation 2.8 at the centroid of the flap location (X_{flap}/l):

$$C_{M_0} = -\frac{4}{\sqrt{M^2-1}}\left(\frac{\pi}{180^\circ}\delta_a\right)\left(\frac{S_{\text{flap}}}{S_{\text{ref}}}\right)\left(\frac{X_{\text{flap}}}{l} - \frac{X_{cg}}{l}\right)\frac{l}{d_{\text{ref}}} \tag{2.14}$$

Consequently, C_{M_0} is linear in δ_a and zero only when δ_a is zero. Figure 2.4 shows the pitching moment coefficient versus angle of attack for a constant Mach number and symmetric deflection. Note the variation in δ_a changes only the value of C_{M_0}, the y-intercept of the pitching moment coefficient.

2.2 Equations of Motion

The longitudinal equations of motion are developed below for a generic, unpowered vehicle traveling in a rotating coordinate frame. For exoatmospheric flights at high Mach numbers, centripetal and Coriolis effects are often non-negligible; consequently, they were included in this development.

Following the development in [13], a stationary atmosphere is assumed. Equatorial, easterly flights were considered, although the development is equally valid for westerly flights if the sign of the Earth's rotation (ω_E) is made negative in the subsequent development of the equations of motion.

Figure 2.5 shows the coordinate system used in the following development. The angle between the inertial x-axis and the position vector from the center of the Earth to the vehicle, Φ, changes with both the tangential component of vehicle velocity (in the rotating coordinate frame), and the rotation rate of the Earth, ω_E. In other words,

$$\left(\frac{\mathrm{d}\Phi}{\mathrm{d}t}\right)_I = \frac{V\cos\gamma}{R_0} + \omega_E \tag{2.15}$$

Within the (rotating) Earth-fixed (EF) reference frame, $\dot{\Phi}$ is defined as

$$\dot{\Phi} = \frac{V\cos\gamma}{R_0} \tag{2.16}$$

Note that $\dot{\Phi} \neq \left(\frac{\mathrm{d}\Phi}{\mathrm{d}t}\right)_I$. The EF and inertial reference frames are identical if ω_E is zero.

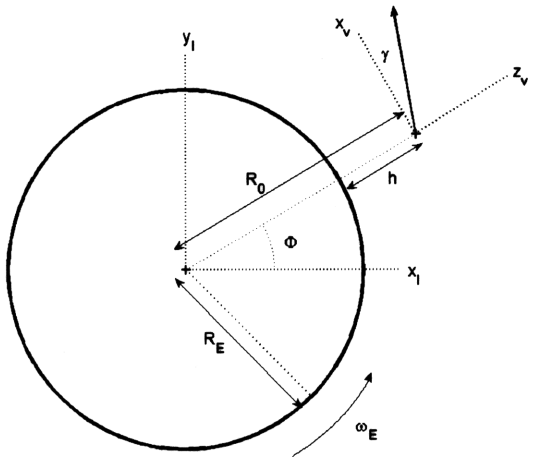

Figure 2.5: Coordinate systems (North Pole points out of the page)

The position vector, $\mathbf{r}$, is

$$\mathbf{r} = R_0 \begin{bmatrix} \cos(\Phi) \\ \sin(\Phi) \end{bmatrix} \tag{2.17}$$

The local velocity vector (velocity "seen" be the vehicle), expressed in the EF reference frame, is

$$\mathbf{V} = V \begin{bmatrix} \sin(\gamma - \Phi) \\ \cos(\gamma - \Phi) \end{bmatrix} \tag{2.18}$$

Then, the time derivative of the local velocity vector is

$$\dot{\mathbf{V}} = \dot{V}\begin{bmatrix} \sin(\gamma - \Phi) \\ \cos(\gamma - \Phi) \end{bmatrix} + V\dot{\gamma}\begin{bmatrix} \cos(\gamma - \Phi) \\ -\sin(\gamma - \Phi) \end{bmatrix} + \\ + V\dot{\Phi}\begin{bmatrix} -\cos(\gamma - \Phi) \\ \sin(\gamma - \Phi) \end{bmatrix} \tag{2.19}$$

where $\dot{\Phi}$ is defined in Equation 2.16.

The standard relation between time derivatives of vectors in inertial and rotating frames is

$$\left(\frac{\mathrm{d}\mathbf{r}}{\mathrm{d}t}\right)_{\text{inertial}} = \left(\frac{\mathrm{d}\mathbf{r}}{\mathrm{d}t}\right)_{\text{rotating}} + \omega \times \mathbf{r} \tag{2.20}$$

In this case, ω is simply ω_E. Hence, the inertial velocity, $\mathbf{V}_I$ is

$$\mathbf{V}_I = \mathbf{V} + \omega_E \times \mathbf{r} \tag{2.21}$$

where $\mathbf{V}$ is the EF velocity vector observed by the vehicle (Equation 2.18).

Taking the time derivative of Equation 2.21 gives

$$\left[\frac{\mathrm{d}\mathbf{V}}{\mathrm{d}t}\right]_I = \dot{\mathbf{V}} + 2\omega_E \times \mathbf{V} + \omega_E \times (\omega_E \times \mathbf{r}) \tag{2.22}$$

since ω_E is constant.

The gravitational force acting on the vehicle is given by

$$\mathbf{F}_g = -mg(h)\begin{bmatrix} \cos\Phi \\ \sin\Phi \end{bmatrix} \tag{2.23}$$

and $g(h)$ is

$$g(h) = \frac{\mu}{(R_E + h)^2} \tag{2.24}$$

The inertial aerodynamic forces, drag ($\mathbf{D}$) and lift ($\mathbf{L}$), are given by

$$\mathbf{D} = -D \begin{bmatrix} \sin(\gamma - \Phi) \\ \cos(\gamma - \Phi) \end{bmatrix} \tag{2.25}$$

$$\mathbf{L} = L \begin{bmatrix} \cos(\gamma - \Phi) \\ -\sin(\gamma - \Phi) \end{bmatrix} \tag{2.26}$$

According to Newton's second law, $\Sigma\mathbf{F} = m\frac{\mathrm{d}\mathbf{V}_I}{\mathrm{d}t}$. This vector equation can be expressed as its inertial x- and y-components:

$$\begin{aligned} -\frac{D}{m}\sin(\gamma - \Phi) + \frac{L}{m}\cos(\gamma - \Phi) - g(h)\cos\Phi = \\ \dot{V}\sin(\gamma - \Phi) + V\dot{\gamma}\cos(\gamma - \Phi) - V\dot{\Phi}\cos(\gamma - \Phi) - \\ -2V\omega_E\cos(\gamma - \Phi) - R_0{\omega_E}^2\cos\Phi \end{aligned} \tag{2.27}$$

$$\begin{aligned} -\frac{D}{m}\cos(\gamma - \Phi) - \frac{L}{m}\sin(\gamma - \Phi) - g(h)\sin\Phi = \\ \dot{V}\cos(\gamma - \Phi) - V\dot{\gamma}\sin(\gamma - \Phi) + V\dot{\Phi}\sin(\gamma - \Phi) + \\ +2V\omega_E\sin(\gamma - \Phi) - R_0{\omega_E}^2\sin\Phi \end{aligned} \tag{2.28}$$

Solving Equations 2.27 and 2.28 for $\dot{V}$ and $\dot{\gamma}$ gives

$$\dot{V} = -\left(\frac{\mu}{{R_0}^2} - {\omega_E}^2 R_0\right)\sin\gamma - \bar{q}S_{\text{ref}}C_D(M,\delta_s)\frac{1}{m} \tag{2.29}$$

$$\dot{\gamma} = \frac{1}{V}\left[-\left(\frac{\mu}{{R_0}^2} - {\omega_E}^2 R_0\right)\cos\gamma + \bar{q}S_{\text{ref}}C_L(M,\delta_a,\delta_s)\frac{1}{m}\right] + \frac{V}{R_0}\cos\gamma + 2\omega_E \tag{2.30}$$

For equatorial flight, the total pitching moment is unchanged between inertial and local coordinate frames (see [13]). Consequently, the 3 degrees-of-freedom (3DoF) longitudinal equations of motion are Equations 2.29 and 2.30 and

$$\dot{q} = \frac{1}{2}\rho V S d_{\text{ref}}\left(C_M(M,\delta_a,\delta_s) + \frac{d_{\text{ref}}}{2V}C_{M_q}(M)q\right)\left(\frac{1}{I_{yy}}\right) \tag{2.31}$$

$$\dot{x_d} = V\cos\gamma\frac{R_E}{R_0} \tag{2.32}$$

$$\dot{h} = V\sin\gamma \tag{2.33}$$

$$\dot{\theta} = q \tag{2.34}$$

with auxillary equations

$$\alpha = \theta - \gamma \tag{2.35}$$

$$M = \frac{V}{a} \tag{2.36}$$

$$\bar{q} = \frac{1}{2}\rho V^2 \tag{2.37}$$

$$R_0 = R_E + h \tag{2.38}$$

The interested reader is directed to [13] for a complete development of the 6DoF equations of motion, as well as [14] for additional background in modeling

atmospheric flight.

2.3 Ballistic Trajectory

A slender reentry vehicle with a fixed symmetric deflection follows a ballistic trajectory similar to that presented in Figures 2.6 and 2.7. The 1976 U.S. Standard Atmosphere is modeled, and the data are obtained from MATLAB/SIMULINK simulations employing the built-in ODE15s solver.[15][16] Note the peak dynamic pres-

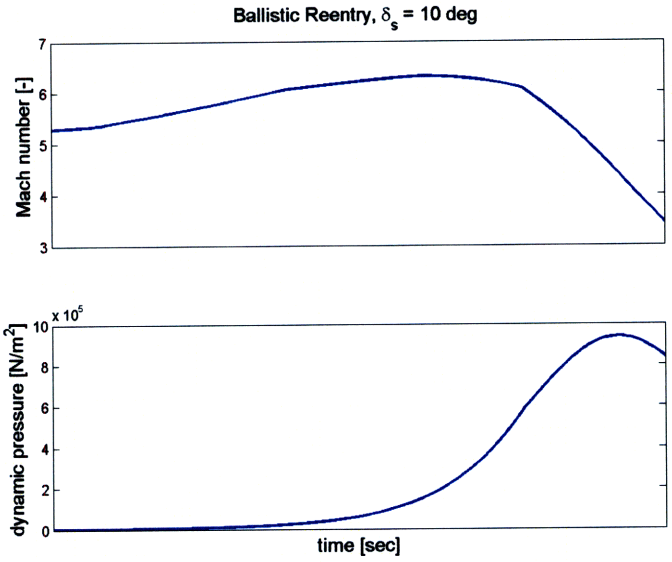

Figure 2.6: Velocity and dynamic pressure histories for a slender reentry vehicle on a ballistic trajectory, $\delta_s = 10$ degrees

sure occurs shortly before impact and does not correspond with peak Mach number, but rather the sharply increasing density as the vehicle descends. Figure 2.7 demonstrates a nearly linear flight path angle, γ, while the angle of attack and pitch rate oscillate rapidly until the dynamic pressure increases. This is characteristic of a lightly damped, marginally stable system.

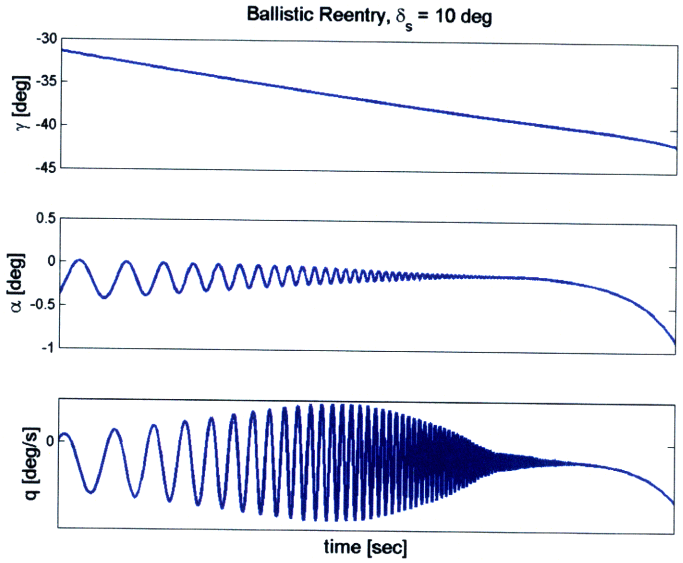

Figure 2.7: Flight path angle, angle of attack, and pitch rate histories for a slender reentry vehicle on a ballistic trajectory, $\delta_s = 10$ degrees

2.4 Maximum Trim Angle of Attack

At a trimmed angle of attack, all pitch rates are zero; that is,

$$q = 0$$
$$\dot{q} = 0$$

From Equations 2.10 and 2.31,

$$\alpha_{\text{trim}} = -\frac{C_{M_0}}{C_{M_\alpha}} \tag{2.39}$$

However, the limits in control surface deflections (see Figure 2.2) limit the combinations of δ_a and δ_s available to trim the vehicle at a specified angle of attack. Figure 2.8 presents a typical example of these limitations for a constant Mach number. The large trim angle of attack is only available for δ_s between 3.8 and 5.9 degrees, while

reduced values of $|\alpha_{\text{trim}}|$ permit larger ranges in δ_s. The trim curves in Figure 2.8 intersect at the symmetric deflection corresponding to zero static margin (neutral static stability), where (theoretically) infinite values of α_{trim} are available. However, the linearized dynamics are not assumed to be valid for $|\alpha| > 10°$ (see Section 2.1).

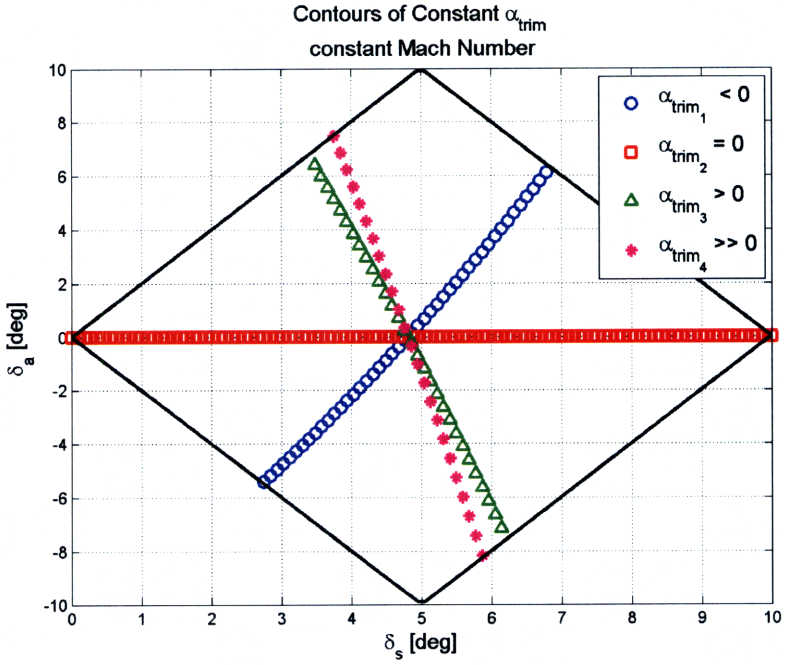

Figure 2.8: Contours of constant α_{trim} as δ_a and δ_s vary; constant Mach number

This page intentionally left blank.

Chapter 3

Baseline Control Design

To better understand the challenges and limitations of Slender Reentry Vehicle (SRV) control, a linear controller is designed to respond to step commands in angle of attack. After a simplification of the equations of motion, rapid development and analysis of this controller is accomplished to identify linear controller strengths as well as weaknesses that could be corrected with more advanced controllers.

Confining analysis to angle of attack tracking leads to a dual-input, single output system. Rather than actively controlling both inputs, this chapter treats symmetric deflection as a parameter and discusses how symmetric deflection can be set based on a performance/robustness trade.

3.1 Simplification of the Equations of Motion

As presented in Section 2.2, six differential equations represent the longitudinal motion of the vehicle:

$$\dot{V} = -\left(\frac{\mu}{{R_0}^2} - {\omega_e}^2 R_0\right)\sin\gamma - \frac{1}{2}\rho V^2 S C_D(M,\delta_s)\frac{1}{m} \tag{3.1}$$

$$\dot{\gamma} = \frac{1}{V}\left[-\left(\frac{\mu}{{R_0}^2} - {\omega_e}^2 R_0\right)\cos\gamma + \frac{1}{2}\rho V^2 S C_L(M,\delta_a,\delta_s)\frac{1}{m}\right] + \frac{V}{R_0}\cos\gamma + 2\omega_e \tag{3.2}$$

$$\dot{q} = \frac{1}{2}\rho V S d_{\text{ref}}\left(C_M(M,\delta_a,\delta_s) + \frac{d_{\text{ref}}}{2V}C_{M_q}q\right)\left(\frac{1}{I_{yy}}\right) \tag{3.3}$$

$$\dot{x_d} = V\cos\gamma\frac{R_E}{R_0} \tag{3.4}$$

$$\dot{h} = V\sin\gamma \tag{3.5}$$

$$\dot{\theta} = q \tag{3.6}$$

The SRV has two control inputs, δ_s and δ_a; δ_s enters the pitch dynamics nonlinearly (see Equation 2.13). For a constant Mach number, Equation 3.3 is approximately a second-order differential equation. From Equation 2.35,

$$\dot{\alpha} = q - \dot{\gamma} \tag{3.7}$$

While γ is certainly nonzero, it is nearly linear in time for a ballistic reentry, as shown in Figure 2.7. Furthermore, this effort assumes $\dot{\gamma}$ does not change significantly in relation to the (faster) controller; that is, $\dot{\gamma} \approx 0$. Consequently, $\ddot{\gamma}$ is nearly zero; thus,

$$\ddot{\alpha} \approx \dot{q} \tag{3.8}$$

$$\dot{\alpha} \approx q \tag{3.9}$$

Assuming the major task of the control system is to track guidance system-generated angles of attack, the pertinent equation of motion reduces to

$$\begin{aligned}\ddot{\alpha} = \Bigg(&- \left[C_{L_{\alpha_0}}(M) + C_{L_{\alpha_\delta}}(M)\delta_s\right]\left[\left(\tfrac{X_{cp}}{l}\right)_0(M) + \right. \\ &+ \left.\left(\tfrac{X_{cp}}{l}\right)_\delta(M)\delta_s - \tfrac{X_{cg}}{l}\right]\tfrac{l}{d_{\text{ref}}}\alpha + \tfrac{d}{2V}C_{M_q}\dot{\alpha} - \\ &- \tfrac{4}{\sqrt{M^2-1}}\left(\tfrac{\pi}{180^\circ}\delta_a\right)\left(\tfrac{S_{\text{flap}}}{S_{\text{ref}}}\right)\left(\tfrac{X_{\text{flap}}}{l} - \tfrac{X_{cg}}{l}\right)\Bigg)\frac{\rho V^2 S d}{2I_{yy}}\end{aligned} \tag{3.10}$$

For a constant Mach number and altitude, Equation 3.10 is of form

$$\ddot{\alpha} = \left(a_1 + a_2\delta_s + a_3{\delta_s}^2\right)\alpha + a_4\dot{\alpha} + b\delta_a \tag{3.11}$$

where δ_s and δ_a are the control inputs and α and $\dot{\alpha}$ are the states. Further inspection shows a plant that is nonlinearly dependent on the symmetric control deflection, δ_s, with δ_s coupling with the angle of attack, α.

3.2 Controller Development

Treating δ_s as a parameter, Equation 3.11 is a linear, second-order differential equation of form

$$\dot{\mathbf{x}} = \mathbf{A}\mathbf{x} + \mathbf{B}\mathbf{u} \tag{3.12}$$

with output $\mathbf{y}$

$$\mathbf{y} = \mathbf{C}\mathbf{x} \tag{3.13}$$

In this case, the only output is angle of attack, so $\mathbf{C}$ is [1 0].

Since the matrix **A** is a function of δ_s, the open-loop poles of the system vary with symmetric deflection. Figure 3.1 shows the open-loop pole locations for a constant Mach number and altitude. Increasing the symmetric deflection alters

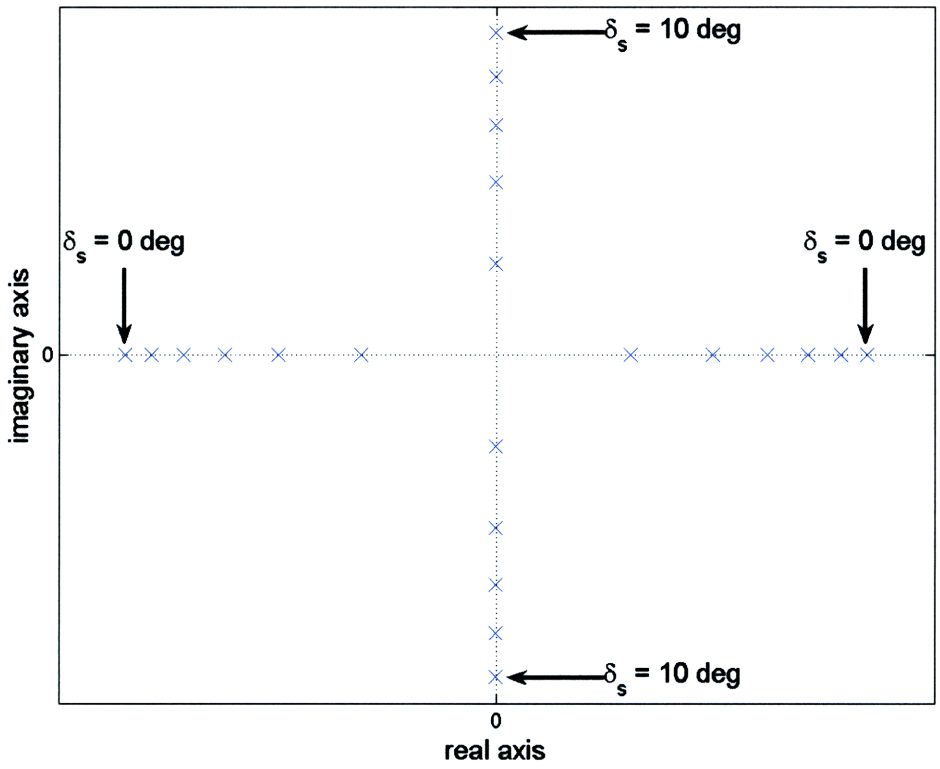

Figure 3.1: Variation in pole location with δ_s for a constant Mach number and altitude (not to scale)

the system from statically unstable to statically stable. Furthermore, static stability increases with increasing Mach numbers.[12]

Optimal control schemes for problems of this type are well-established. The reader is directed to the large body of literature addressing optimal linear control (e.g., [17],[18],[19]).

The linear quadratic regulator (LQR) optimizes the cost function

$$J = \int_0^\infty \left[\mathbf{x^T Q x} + \mathbf{u^T R u}\right] \mathrm{d}t \tag{3.14}$$

where $\mathbf{Q}$ and $\mathbf{R}$ are diagonal weighting matrices that are positive semidefinite and positive definite, respectively.[18] The control, $\mathbf{u}$, that minimizes Equation 3.14 is

$$\mathbf{u} = -\mathbf{K}\mathbf{x} = -\mathbf{R}^{-1}\mathbf{B}^T\mathbf{P}\mathbf{x} \tag{3.15}$$

where $\mathbf{P}$ is symmetric and satisfies the algebraic Riccati equation

$$\mathbf{0} = \mathbf{P}\mathbf{A} + \mathbf{A}^T\mathbf{P} + \mathbf{Q} - \mathbf{P}\mathbf{B}\mathbf{R}^{-1}\mathbf{B}^T\mathbf{P} \tag{3.16}$$

The LQR is inherently robust for linear systems: gain margins are guaranteed to be $(\frac{1}{2}, \infty)$ and phase margins greater than $\pm 60°$.[19] Of course, control saturations are inherently nonlinear; these will be treated later.

LQR is insufficient for the tracking problem because it drives all system states to zero; replacing LQR with LQ-servo by augmenting the states with

$$e_I \triangleq \int_0^t (r - \alpha(\tau))\, \mathrm{d}\tau \tag{3.17}$$

allows tracking of a reference angle of attack. This augments Equation 3.12 to

$$\begin{bmatrix} \dot{\mathbf{x}} \\ e_I \end{bmatrix} = \begin{bmatrix} \mathbf{A} & \mathbf{0} \\ -\mathbf{C} & \mathbf{0} \end{bmatrix} \mathbf{x} + \begin{bmatrix} \mathbf{B} \\ 0 \end{bmatrix} \mathbf{u} + \begin{bmatrix} \mathbf{0} \\ 1 \end{bmatrix} \mathbf{r} \tag{3.18}$$

LQ-servo is better suited than direct feedforward of the reference signal to the tracking problem when control deflection limits are present. Since e_I integrates the tracking error from zero time, and $\int_0^0 f(x)\mathrm{d}x = 0$, the control response is less aggressive and unlikely to immediately saturate from a step tracking command.

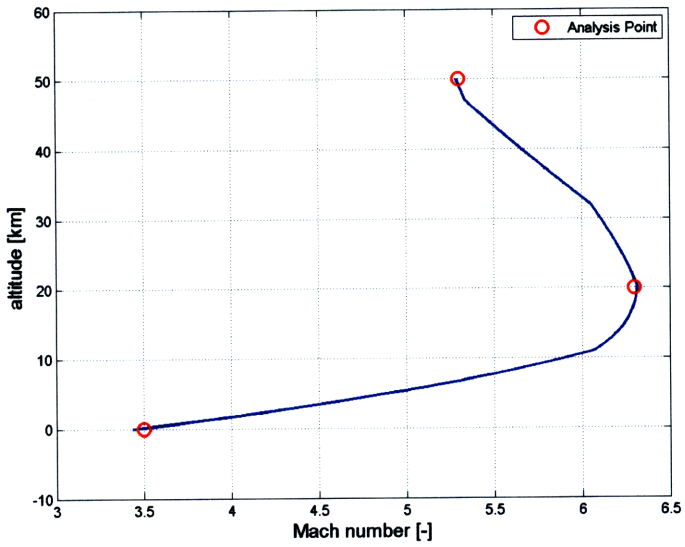

Figure 3.2: Reentry profile

For a given flight condition (Mach number and altitude), linear control gains are generated for symmetric deflections in the range [2,8] degrees. Values of δ_s outside this range give very little δ_a, since flap deflections are limited to [0,10] degrees (see Section 2.1.1). Consequently, they are assumed to be of little use in reference tracking. Three flight conditions are evaluated, as shown in Table 3.1 and Figure 3.2.

Table 3.1: Flight conditions selected for analysis of the SRV

Mach	altitude (km)
3.5	0
6.3	20
5.3	50

To simplify the performance/robustness trade for variations in symmetric deflection, the 10% to 90% rise time, t_r, for a one degree step command is selected as the primary indicator of tracking performance (see Figure 3.3 and the following section).[20] A constant rise time for all symmetric deflections sets a time domain performance standard, easing the subsequent robustness analysis. Presumably, tracking

performance becomes more critical as the vehicle descends and remaining flight time decreases. Thus, the desired rise time decreased as the vehicle descended. At the whole number symmetric deflections on [2,8] degrees, the weighting matrices **Q** and **R** are chosen such that the loop gain margin is 6 (15.6 dB) and the rise time met the desired threshold. **Q** is a 3x3 matrix with nonzero terms on the main diagonal:

$$\mathbf{Q} = \begin{bmatrix} q_\alpha & 0 & 0 \\ 0 & q_q & 0 \\ 0 & 0 & q_{e_I} \end{bmatrix}$$

With a single control input, **R** is scalar; fixing R at unity left three degrees of freedom in the search. The diagonal terms of **Q** are initialized according to Bryson's rule [17], and a bisection search algorithm determined a **Q** such that

$$J = \frac{1}{2}\left(\frac{|t_r - t_{r_{\text{des}}}|}{tol \cdot t_{r_{\text{des}}}} + \frac{|gm - gm_{\text{des}}|}{tol \cdot gm_{\text{des}}}\right) < 1 \tag{3.19}$$

where *tol* is a specified tolerance. The bisection search algorithm ceased as soon as Equation 3.19 is satisfied.

3.3 Results

At each flight condition, whole-number symmetric deflections between 2 and 8 degrees are considered. At each symmetric deflection, a single controller (i.e., set of LQ-servo gains) is selected according to the development in Section 3.2. Employing MATLAB/SIMULINK and the built-in ODE15s solver[15][16], the vehicle tracking performance with the LQ-servo controller is simulated. Then, each controller's performance and robustness are compared, allowing selection of an ideal symmetric deflection.

The ensuing development follows an incremental build-up of the system:

1. The system without actuator dynamics.
2. The system with a first-order actuator.
3. The system with a first-order actuator and lead compensator.

The gains determined in Step 1 are held constant throughout the ensuing development. This process highlights the difficulties associated with the plant itself versus those difficulties arising out of unmodeled actuator dynamics and plant/actuator interactions.

The optimal LQ-servo gains, found using the method described in Section 3.2, are employed to track step commands from 1 to 10 degrees. Rather than compare numerous time responses, three quantifiable time response characteristics are selected:[20]

- 10% to 90% rise time, t_r
- 5% settling time, t_s
- magnitude of peak overshoot, m_p

Figure 3.3 shows these values on a sample time response to a unity step command. The rise time indicates how quickly the systems responds to an input command; generally, a low time response is desirable. In this effort, the rise is fixed to standardize the time

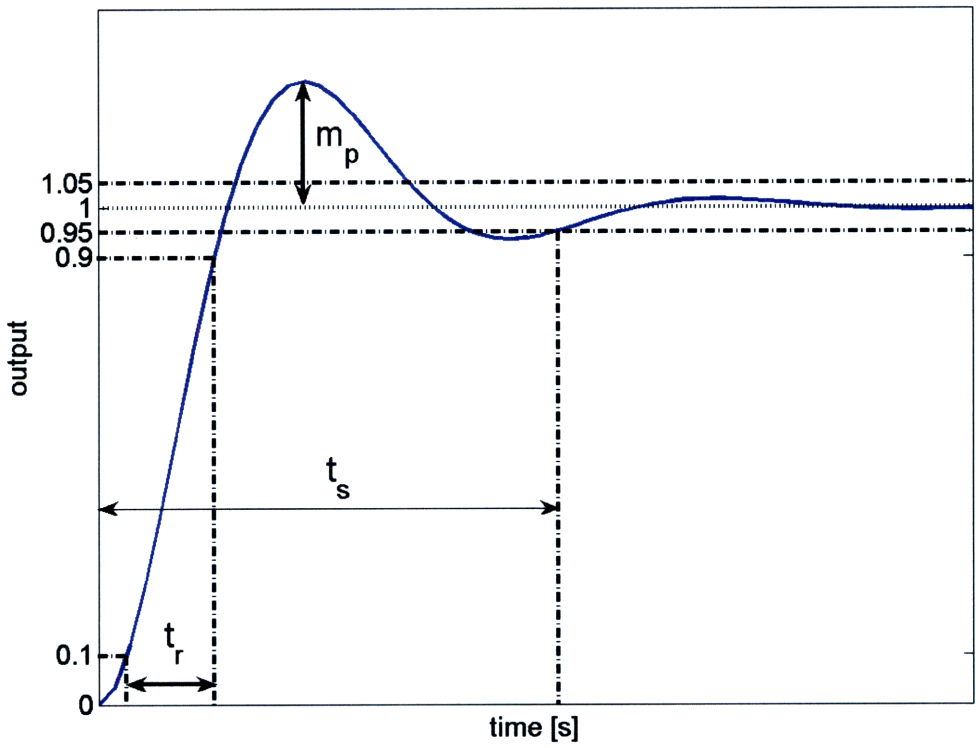

Figure 3.3: Sample time response showing rise time (t_r), settling time (t_s), and peak overshoot (m_p) for a unity step command

responses of various configurations (see Section 3.2). The settling time indicates how long it takes the response to stay "close" to the commanded value. Once again, a low settling time is usually desirable. An infinite settling time can be encountered if the system approaches a limit cycle with an oscillation about the reference command. The magnitude of the peak overshoot is the maximum difference between the reference command and the time response, often expressed as percent of the reference command. A small peak overshoot is often desirable; large peak overshoots often indicate near-instability. However, an overdamped system exhibits zero peak overshoot; in many cases, this is not desirable because overdamped systems can have high rise times. Consequently, low rise time and low peak overshoot can be antagonistic. These three time response characteristics summarize the time response in a concise, quantifiable form.

The step response characteristics for the Mach 3.5, 0 km altitude case and representative symmetric deflections can be found in Figure 3.4. Rise times are within

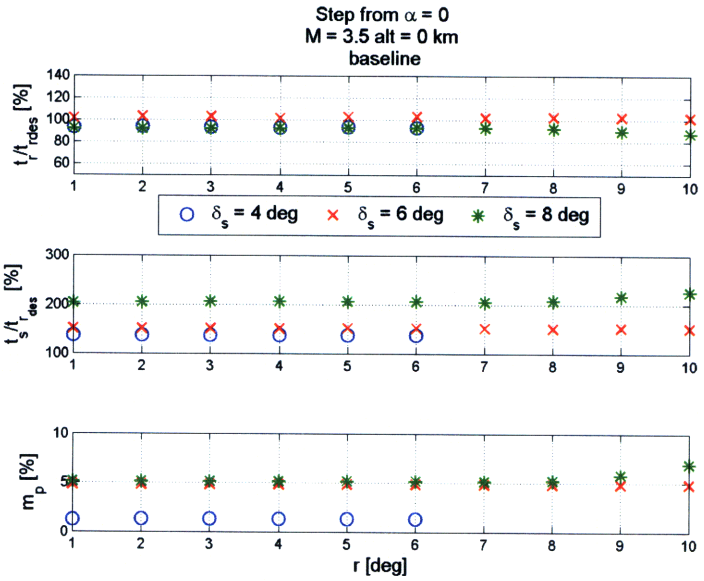

Figure 3.4: Time response characteristics for step commands from 0 degrees, Mach 3.5, 0 km altitude

10% of the specified value for the 1 degree step (the design condition). Settling times less than 250% of the desired rise time for the zero-altitude case; additionally, settling times are lower for lower symmetric deflections (reduced static stability). However, the 4 degree symmetric deflection configuration cannot track reference commands greater than 6 degrees; reference commands greater than 6 degrees result in controller saturation. The vehicle is statically unstable at Mach 3.5 and 4 degrees of symmetric deflection; without further control authority, the system remains unstable. The peak overshoot is consistently below 6%. The 4 degree symmetric deflection minimized peak overshoot for the range of commands it sucessfully tracked.

The step response characteristics for the Mach 6.3, 20 km altitude case and representative symmetric deflections is found in Figure 3.5. Once again, rise times

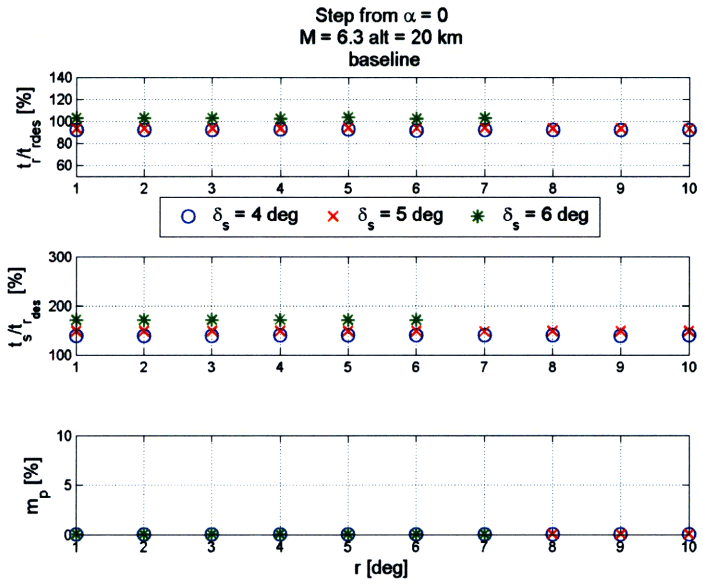

Figure 3.5: Time response characteristics for step commands from 0 degrees, Mach 6.3, 20 km altitude

are within 10% of the specified value for the range of commands shown. The 6 degrees of symmetric deflection configuration is unable to track commands greater than 7 degrees. Control saturation limits the tracking performance for this case.

The remaining representative symmetric deflections (4 and 5 degrees) show similar performance across the range of reference commands shown. Peak responses are negligible. This may motivate a faster desired rise time in later research, although low dynamic pressure and control saturation limits may prove to be the limiting factors.

The step response characteristics for the Mach 5.3, 50 km altitude case are shown in Figure 3.6. The limited range of reference commands that may be tracked

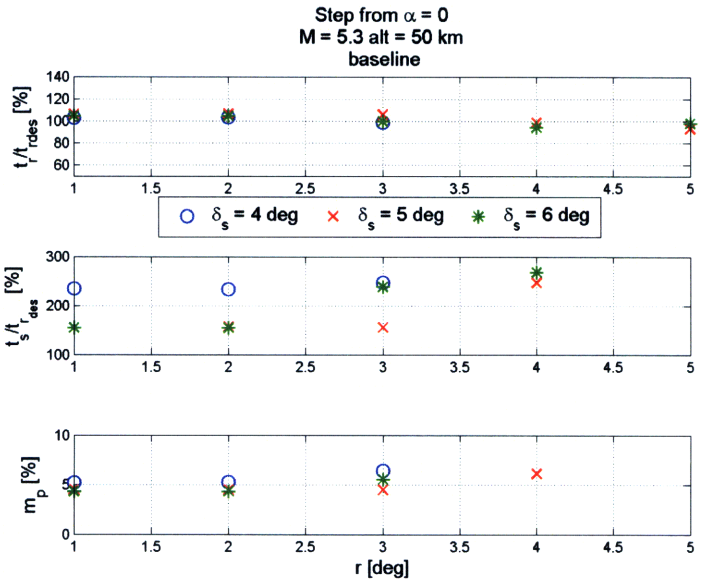

Figure 3.6: Time response characteristics for step commands from 0 degrees, Mach 5.3, 50 km altitude

is immediately apparent. Symmetric deflections outside the range shown failed to track commands greater than 5 degrees. Rise times remain within 10% of the desired value. Settling times increase for all cases shown as the magnitude of the reference command increases. Likewise, peak overshoot increases from less than 5% for 1 degree commands to well over 10% for 5 degree commands. Again, control saturation limits the system performance.

3.3.1 Linear Gain and Phase Margins

The reference to angle of attack transfer function gain and phase margins for all three flight conditions are shown in Figure 3.7. These robustness margins ignore the effects of control saturation. Control saturation can be a problem if the system is statically unstable (i.e., low values of δ_s). A statically stable system can cope with control saturation, although tracking performance may be diminished. Control saturation effects are discussed in subsequent sections. Gain margins are all between 14.5 and

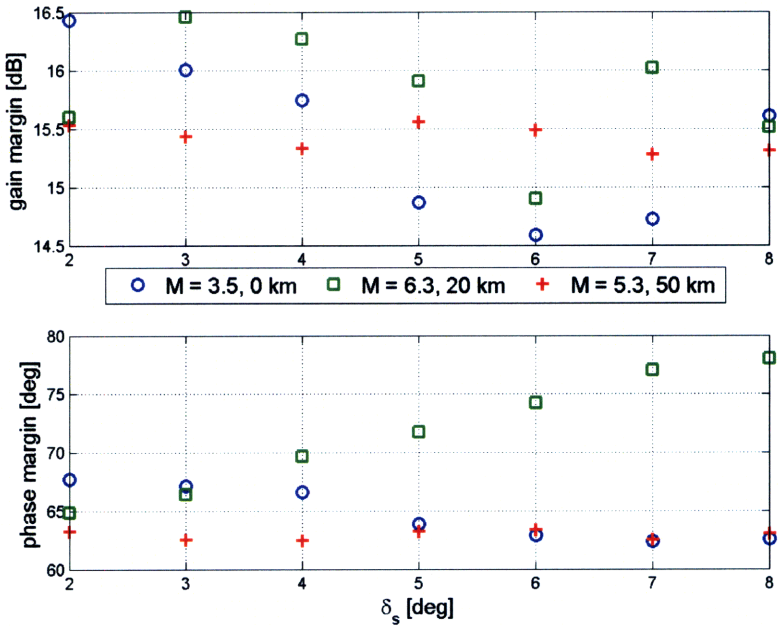

Figure 3.7: Gain and phase margins for the reference command to angle of attack loop transfer functions as δ_s varies

16.5 dB, satisfying the design criteria of Section 3.2, while phase margins are greater than 60 degrees. It is interesting to note the 13 degree rise in phase margin as δ_s increases for the Mach 6.3, 20 km altitude case. Increasing symmetric deflection decreases phase margin 5 degrees at 0 km, and has little effect at 50 km.

3.3.2 Initial Robustness Analysis

Although controller development assumed perfect knowledge of the plant dynamics, the vehicle may be poorly modeled. Three uncertainties are considered. First, the center of pressure location is likely to be known within some (possibly large) tolerance. Second, the extreme reentry environment may cause control surface ablation, reducing control effectiveness. Third, asymmetric vehicle ablation may create a nonzero pitch acceleration (moment) that modifies the trim condition. These three effects are examined below for 1 degree step commands.

The effects of variations in the center of pressure location and control surface effectiveness are summarized in Figures 3.8, 3.9 and 3.10. Here, 0% variation in X_{cp} is the nominal case; that is, there is zero variation in the center of pressure from ideal. Conversely, 100% control effectiveness indicates the controls are operating with 100% of their nominal performance. For maximum system robustness, high tolerances of X_{cp} variation and low allowable control effectiveness are desired. The nonlinear instability limit represents where the closed-loop system diverges; in practice, nonlinear instability is defined to be $|\alpha| > 20°$. The center of pressure may be unknown from unmodeled aerodynamic effects, vehicle ablation, poorly modeled flight conditions, etc.; thus, it is important to understand the bounds on center of pressure knowledge. The allowable center of pressure variations are correlated with the linear instability limits (i.e., when the closed-loop poles cross the $j\omega$ axis). Exceptions to this occur when the system is very statically unstable (low values of δ_s): then, the saturation limits keep the control system from providing closed-loop stability. The control saturation limits are where the SRV can no longer trim at the reference command (see Section 2.4).

The control surface effectiveness limits are important, especially in the face of unmodeled flap ablation during reentry. At the 0 km altitude case, the system is

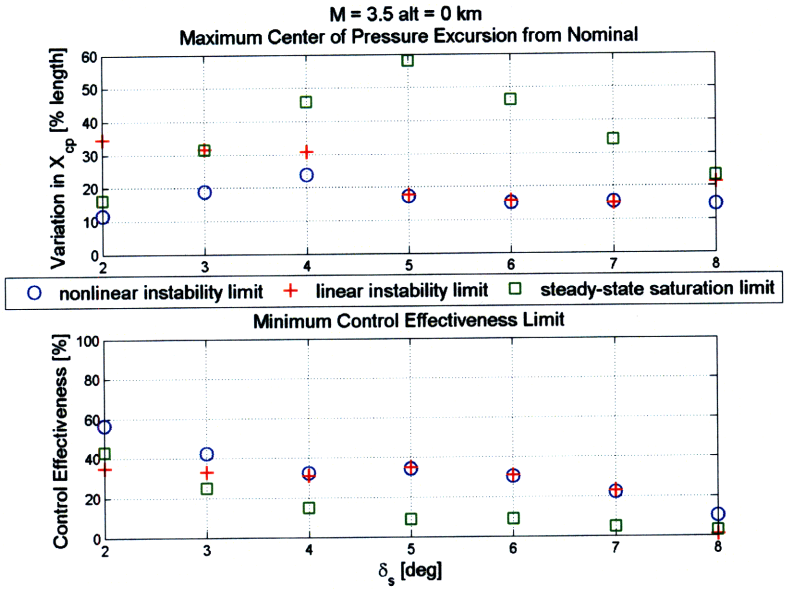

Figure 3.8: Allowable variation in center of pressure location and reduction in control effectiveness, step command from 0 to 1 degree, Mach 3.5, 0 km altitude

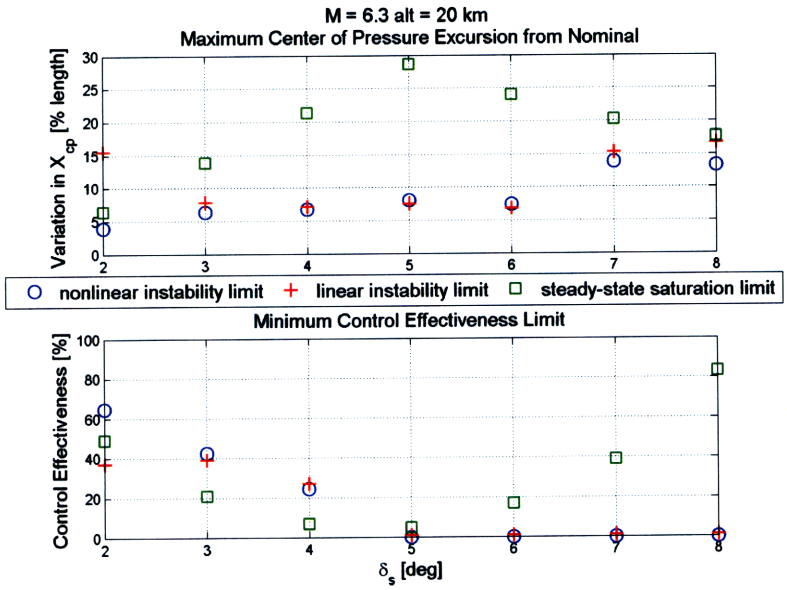

Figure 3.9: Allowable variation in center of pressure location and reduced control effectiveness, step command from 0 to 1 degree, Mach 6.3, 20 km altitude

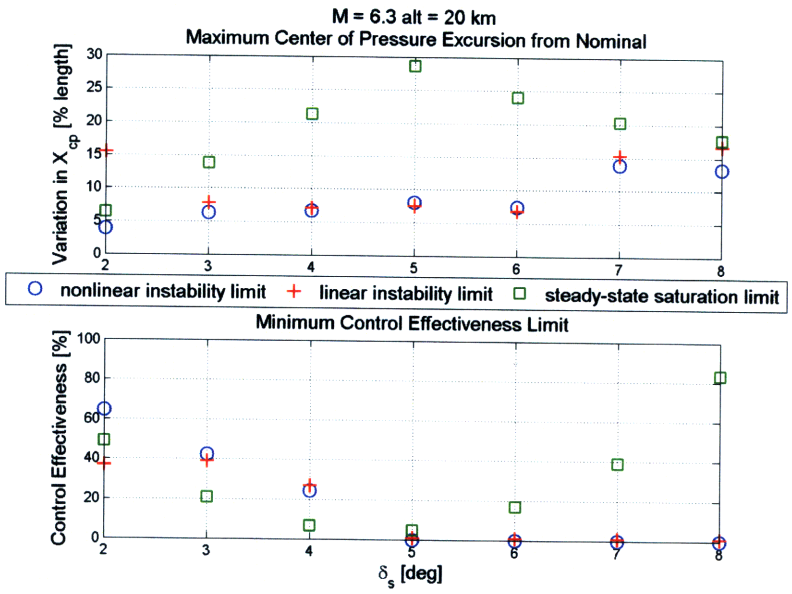

Figure 3.10: Allowable variation in center of pressure location and reduced control effectiveness, step command from 0 to 1 degree, Mach 5.3, 50 km altitude

relatively intolerant of reduced control effectiveness. This intolerance is closely related to the linear instability of the closed-loop system. Increased δ_s permits lower control effectiveness before reaching instability. Higher Mach numbers may remain stable for decreased values of control effectiveness, but these high Mach numbers occur at higher altitudes during the reentry. Consequently, dynamic pressures are reduced and overall control effectiveness is likewise reduced. Thus, control saturation limits are reached sooner in the face of reduced control effectiveness, even though these may not be destabilizing. This is apparent in the cases at 20 and 50 km altitude: for large symmetric deflections (greater static stability), the control saturation limit is reached before the trajectories diverge.

The influence of an external pitch acceleration (specific moment) is evaluated and shown in Figures 3.11, 3.12, and 3.13. This is considered because asymmetric ablation may cause an external pitching moment on the vehicle. At high dynamic pressures, the controls are more effective at reducing an external moment, while

lower dynamic pressures reduce control effectiveness. In the presence of tight control deflection limits, even a small external acceleration (on the order of 15 deg/s^2) can cause control saturation and instability. The case at 20 km (Figure 3.12) is especially

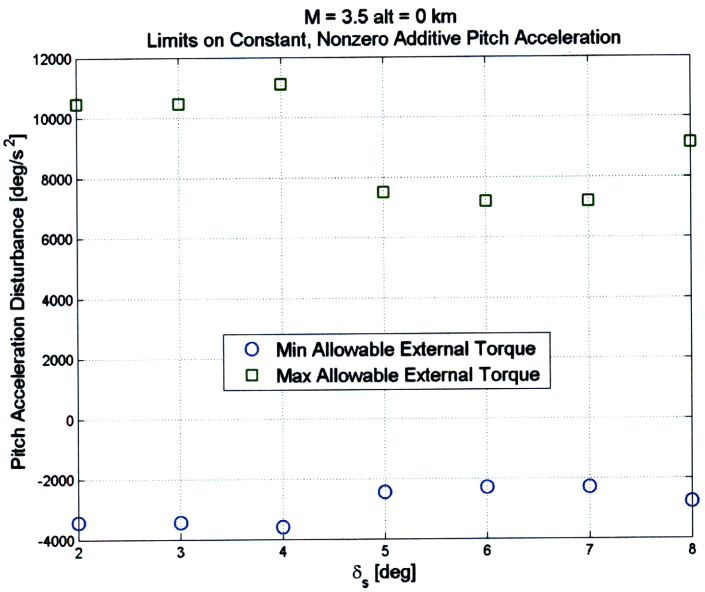

Figure 3.11: Robustness to external pitch acceleration, step command from 0 to 1 degree, Mach 3.5, 0 km altitude

interesting. The other two cases are fairly constant across the range of δ_s, but the intermediate altitude shows a minimum performance for symmetric deflections near 3 and 4 degrees. Robustness to external pitch accelerations is gained when symmetric deflections are decreased to 2 degrees or increased to 8 degrees.

Robustness for reference commands greater than 1 degree is also considered. Plots similar to Figures 3.8–3.13 for step commands from 0 to 10 degrees can be found in Appendix A; they are omitted here for the sake of brevity. The robustness of larger step commands will be revisited in subsequent sections of this chapter.

Thus far, the robustness analysis highlighted three separate behaviors. First, static instability coupled with poor plant knowledge (center of pressure variation,

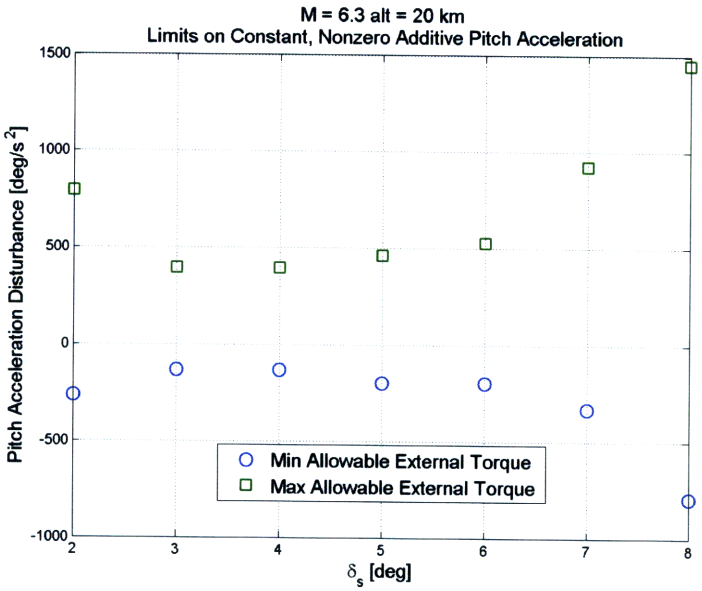

Figure 3.12: Robustness to external pitch acceleration, step command from 0 to 1 degree, Mach 6.3, 20 km altitude

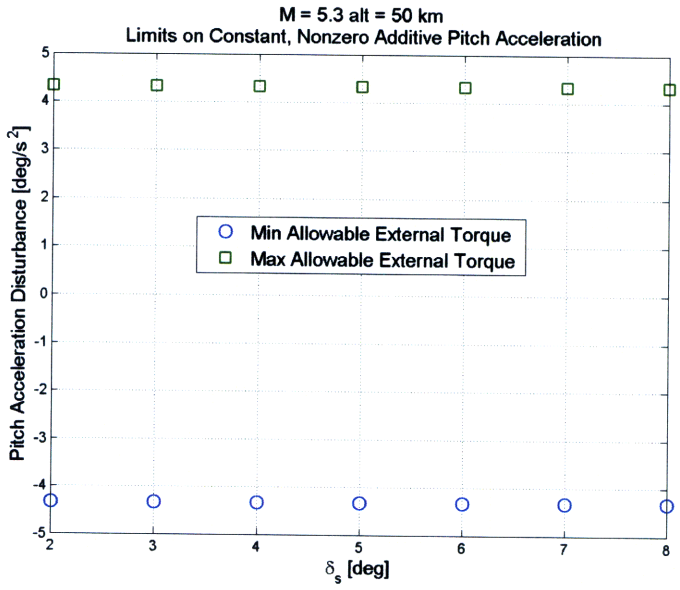

Figure 3.13: Robustness to external pitch acceleration, step command from 0 to 1 degree, Mach 5.3, 50 km altitude

reduced control effectiveness, external pitching moment) can lead to control surface saturation, effectively eliminating the active control. Thus, the system becomes unstable. Second, if the control saturates but the vehicle is statically stable, the disturbance does not destabilize the system; however, the off-nominal plant cannot track reference commands. Finally, sufficient control authority can exist to compensate for the plant disturbance. Then, the vehicle becomes unstable when the linear robustness bounds reach zero and the closed-loop poles cross the $j\omega$ axis.

As might be expected, larger reference commands require better plant knowledge to maintain sufficient tracking and closed-loop stability. Furthermore, greater total control effectiveness (i.e., higher dynamic pressures) are more tolerant of off-nominal plants.

3.3.3 Actuator Dynamics

The addition of a first-order actuator of the form $\frac{p}{s+p}$ decreased the performance of the system, especially at lower altitudes where the short period dynamics are significantly faster. Figure 3.14 demonstrates the loss of gain and phase margin for the Mach 3.5, 0 km altitude case (compare to Figure 3.7). The margins at 20 and 50 km are largely unchanged because the plant dynamics are significantly slower than the actuator dynamics.

The vehicle time response characteristics at Mach 3.5, 0 km altitude are summarized in Figure 3.15. Similar graphs for the additional two flight conditions studied are shown in Appendix A. These are omitted here because performance does not change significantly for these cases.

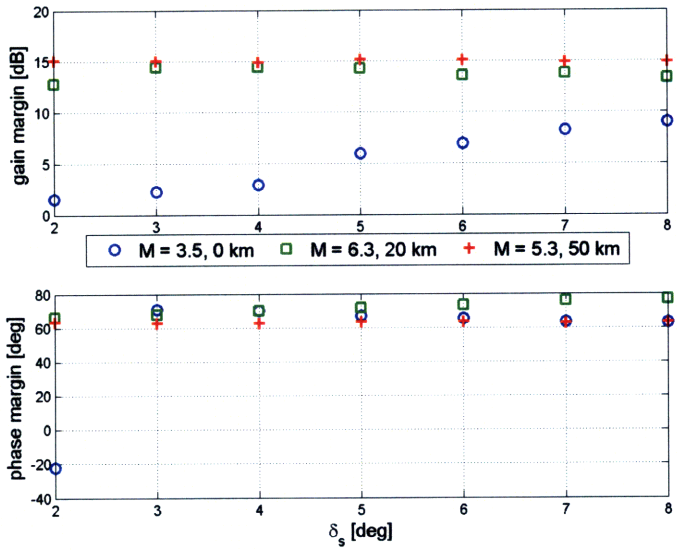

Figure 3.14: Gain and phase margins for the reference command to angle of attack loop transfer functions as δ_s varies, 1st order actuator modeled

Figure 3.15 summarize the vehicle's time response characteristics with actuator dynamics modeled. The appearance of faster rise times in Figure 3.15 contrasts the increased settling times. Additionally, peak overshoots are increased, especially as the magnitude of the reference command increases. The 1 degree step response for 4 degrees of symmetric deflection is shown in Figure 3.16. Both the 4 and 6 degrees of δ_s demonstrate a reduced tracking capability; the former reduces from a maximum of 6 degrees angle of attack to 4 degrees, while the latter reduces from 10 degrees to 9 degrees angle of attack. The loss of gain and phase margin corresponds to a general reduction in system stability. The phase lag added by the actuator, coupled with the stringent control saturations and a statically unstable plant, limit the performance of these cases. Even the 8 degrees of symmetric deflection configuration suffers reduced settling time and increased peak overshoot for large reference commands. Recall the aerodynamic approximations are only valid for $|\alpha| \leq 10$ degrees; a large peak overshoot may push the pitching moment into a highly nonlinear region that is not well-modeled.

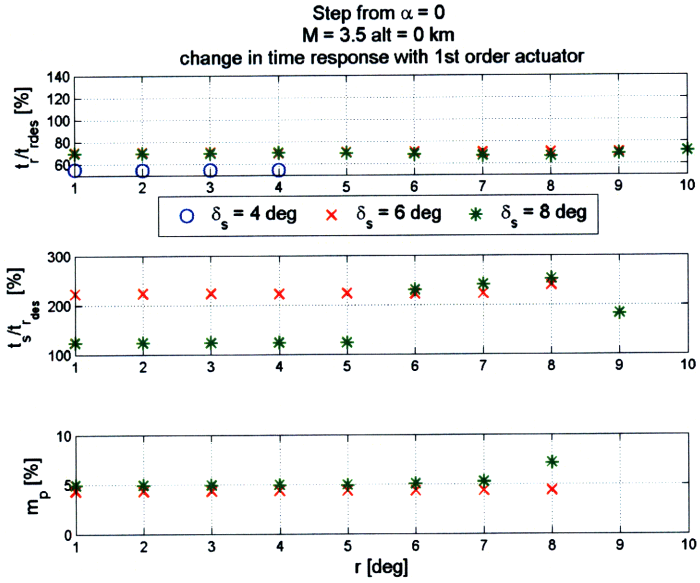

Figure 3.15: Time response characteristics for step commands from 0 degrees, Mach 3.5, 0 km altitude, 1st order actuator modeled

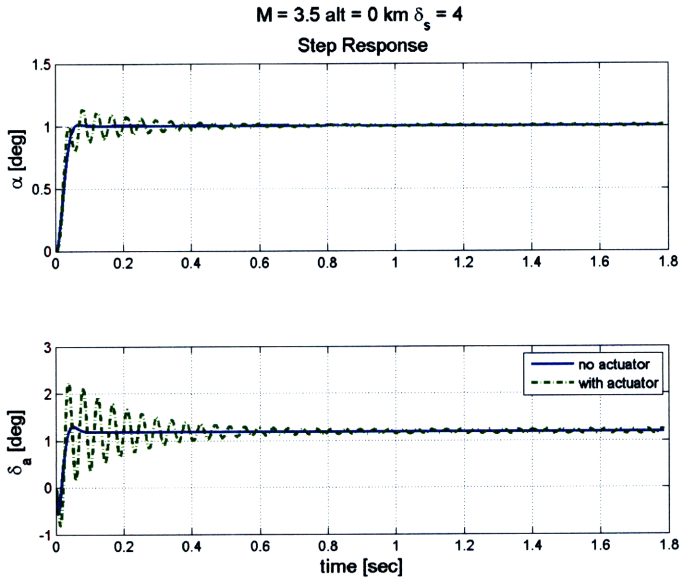

Figure 3.16: 1 degree step response with actuator, Mach 3.5, 0 km altitude

Figure 3.17 reveals the robustness to center of pressure variation is reduced for all cases to approximately 10% (compare to Figure 3.8). The robustness to external

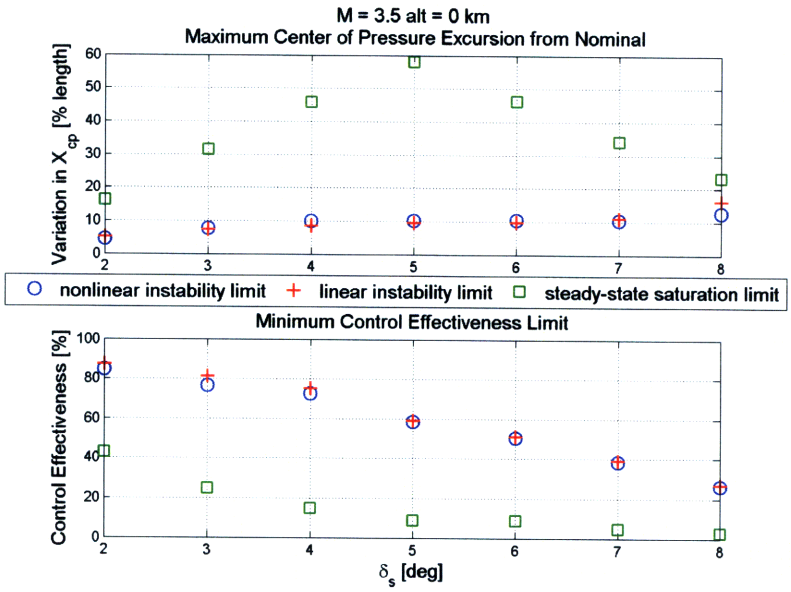

Figure 3.17: Allowable variation in center of pressure location and reduced control effectiveness, step command from 0 to 1 degree, Mach 3.5, 0 km altitude, 1st order actuator modeled

pitch accelerations is also reduced, as shown in Figure 3.18.

As previously mentioned, the actuator dynamics did not significantly affect the Mach 6.3, 20 km case or the Mach 5.3, 50 km case. The robustness summaries of these cases with the actuator dynamics included are shown in Appendix A

3.3.4 Addition of Lead Compensator

To eliminate the oscillatory effect of actuator dynamics on vehicle tracking performance, a lead compensator of the form $\frac{s+a}{s+b}, a < b$, is added. A simple pole-zero can-

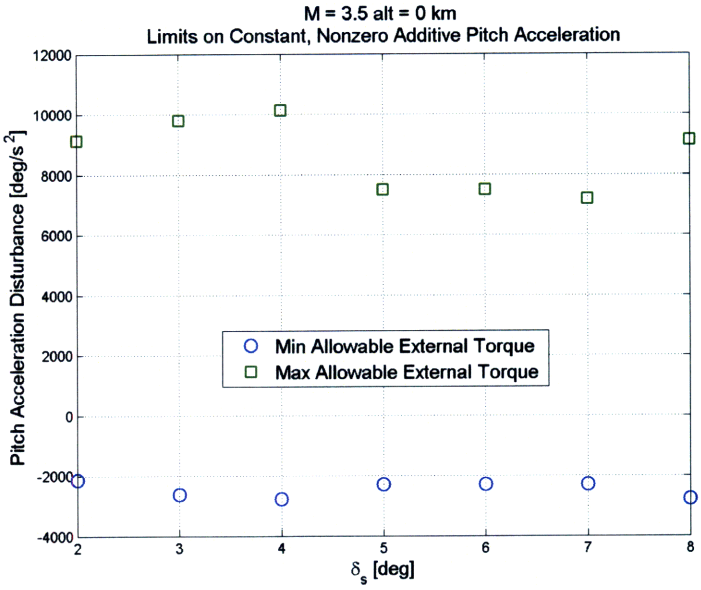

Figure 3.18: Robustness to external pitch acceleration, step command from 0 to 1 degree, Mach 3.5, 0 km altitude, 1st order actuator modeled

cellation is not desirable because actuator dynamics are not likely to be well-known. Rather, the lead compensator is designed to regain the phase loss the actuator added (see Figure 3.19). If the actuator includes significant additional dynamics beyond the first-order actuator modeled, the performance shown below is overly optimistic. However, effective design of a lead compensator may still mitigate actuator-induced difficulties. The gain and phase margins for the system are presented in Figure 3.20. The LQ-servo gains previously determined are unchanged; all changes in performance from that depicted in Section 3.2 result from the addition of the actuator and compensator. The gain margins for all cases are improved; recall the phase margin for $\delta_s = 2$ degrees at Mach 3.5, 0 km altitude is negative with the addition of the actuator (see Figure 3.14). Note the time response is improved (Figure 3.21).

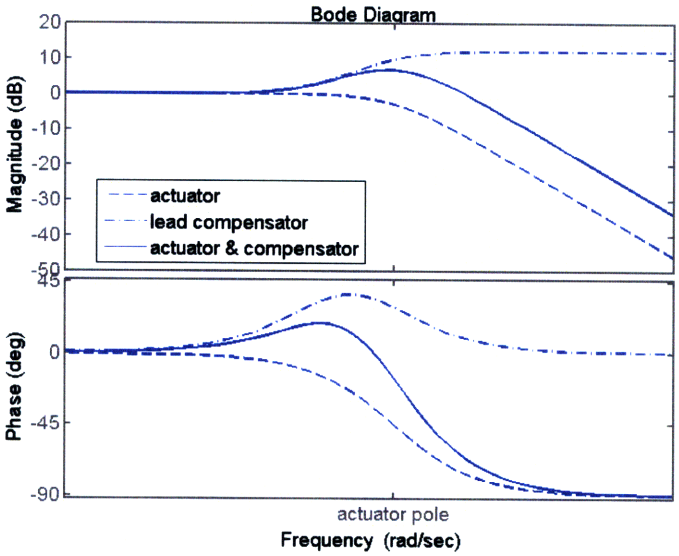

Figure 3.19: Bode plot for 1st order actuator, lead compensator, and their series

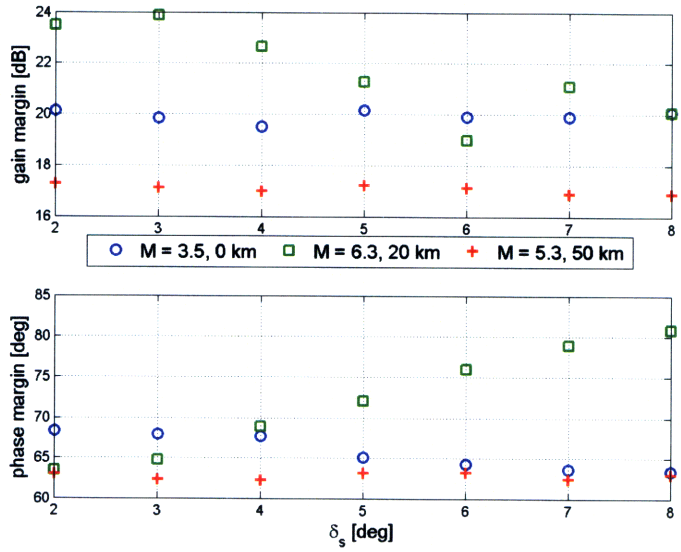

Figure 3.20: Gain and phase margins for the reference command to angle of attack loop transfer functions as δ_s varies, 1st order actuator and lead compensator modeled

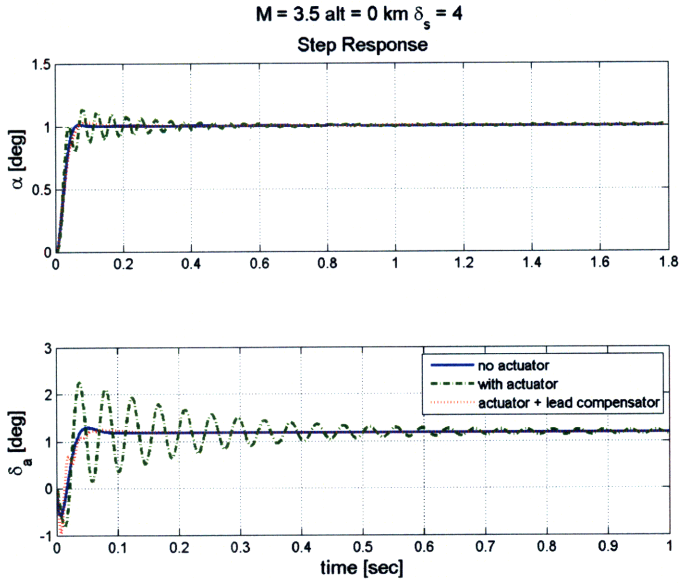

Figure 3.21: 1 degree step response, Mach 3.5, 0 km altitude, 1st order actuator and lead compensator

3.3.5 LQ-servo Performance at M = 3.5, 0 km Altitude

The time response summary for Mach 3.5, 0 km altitude with the actuator and lead compensator is presented in Figure 3.22. The rise times are increased for all cases shown, although the settling times are improved. The settling times for small reference commands and 8 degrees of symmetric deflection are improved approximately 50%. Peak overshoots are less than 8%, compared to over 20% for the actuator alone. Additionally, 4 degrees of symmetric deflection still cannot track reference commands greater than 6 degrees.

Compare the robustness to center of pressure location and control effectiveness for 1 and 10 degree step commands (Figures 3.23 and 3.24). The smaller reference command is limited by the linear instability limit, while the larger reference command

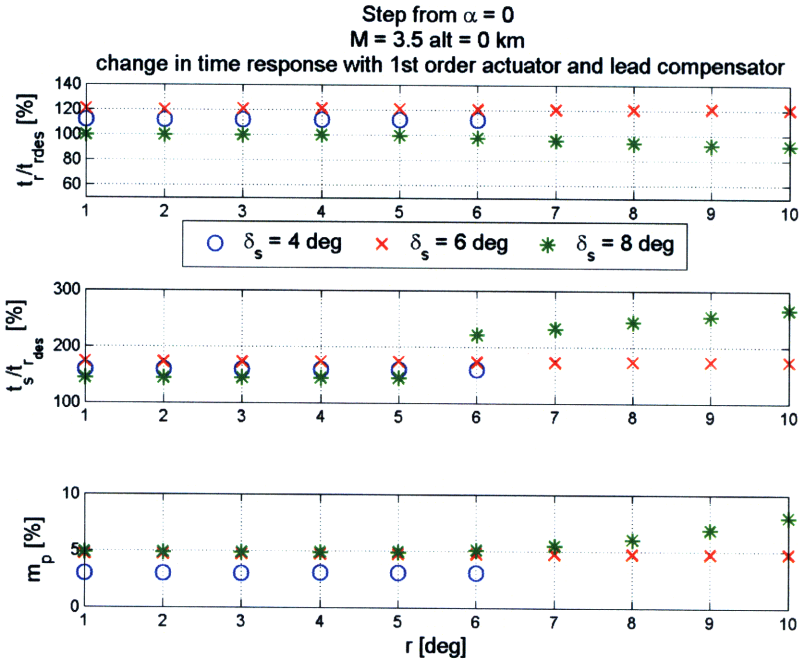

Figure 3.22: Time response characteristics for step commands from 0 degrees, Mach 3.5, 0 km altitude, actuator and lead compensator modeled

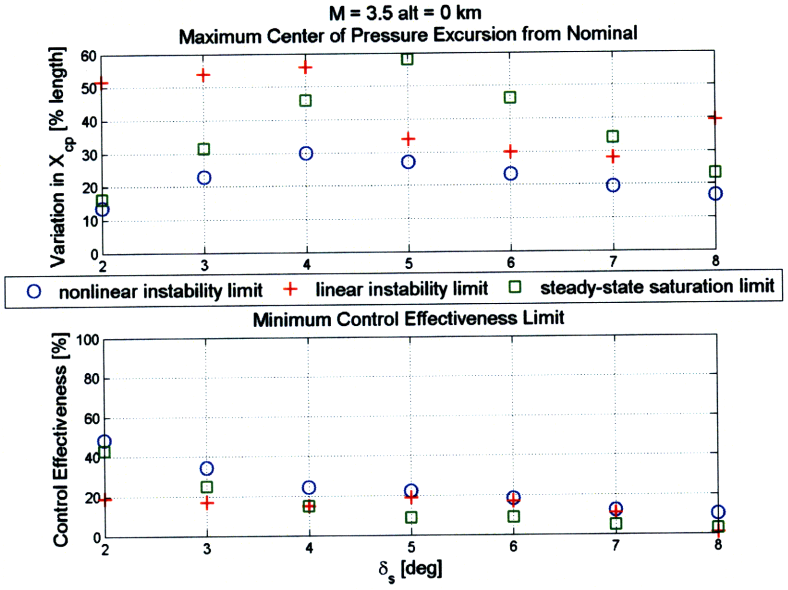

Figure 3.23: Allowable variation in center of pressure location and reduction in control effectiveness, step command from 0 to 1 degree, Mach 3.5, 0 km altitude, actuator and lead compensator modeled

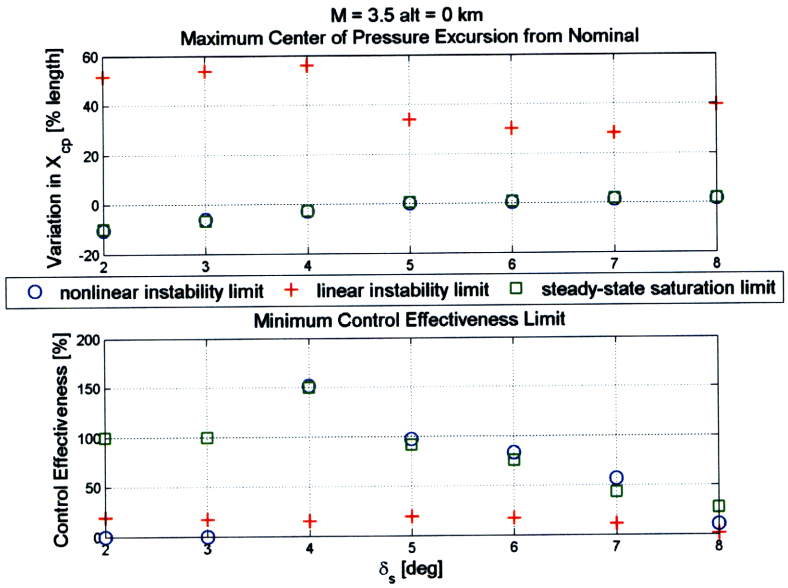

Figure 3.24: Allowable variation in center of pressure location and reduction in control effectiveness, step command from 0 to 10 degrees, Mach 3.5, 0 km altitude, actuator and lead compensator modeled

has its robustness limits tied to controller saturation. Note symmetric deflections under 5 degrees are unstable for a 10 degree command. This is apparent since the allowable variation in X_{cp} is negative, indicating the nominal case (zero variation) is unstable. Additionally, these symmetric deflections require more than 100% of available control authority. Consequently, the flaps saturate and are unable to stabilize (or control) the system for δ_s less than 5 degrees.

Figures 3.22 show a decrease in rise time and an improvement in robustness to static margin uncertainty and reduced controller effectiveness, compared to the baseline case (Figure 3.4). However, this is misleading: the actuator is modeled as an ideal, 1st order exponential rise. In fact, the actuator may have additional dynamics, and these dynamics may be poorly modeled or unknown. While it is unreasonable to assume the lead compensator can totally eliminate all undesired actuator effects, it can be effective at reducing the severity of these effects.

The robustness to external pitch accelerations for 1 and 10 degree step commands are shown in Figures 3.25 and 3.26.

As might be expected, the controller is more capable of tracking a smaller reference command in the face of an external pitching moment. Recall symmetric deflections under 5 degrees are unstable in tracking the 10 degree reference command.

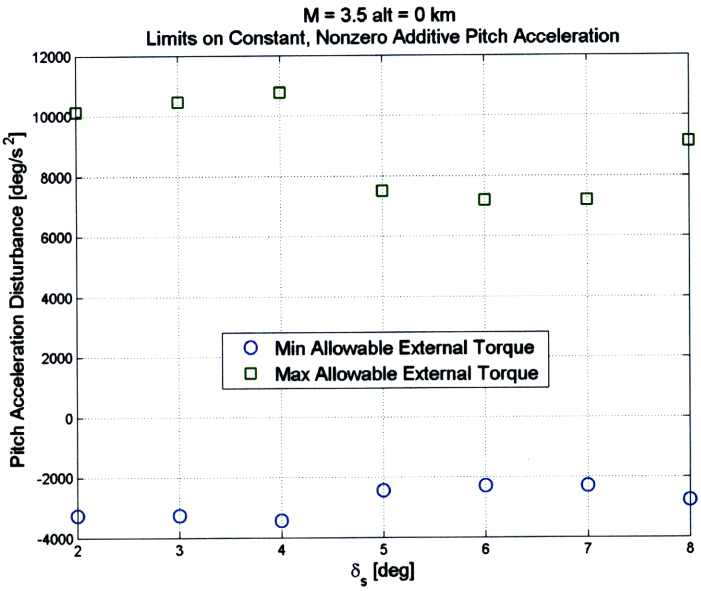

Figure 3.25: Robustness to external pitch acceleration, step command from 0 to 1 degree, Mach 3.5, 0 km altitude, actuator and lead compensator modeled

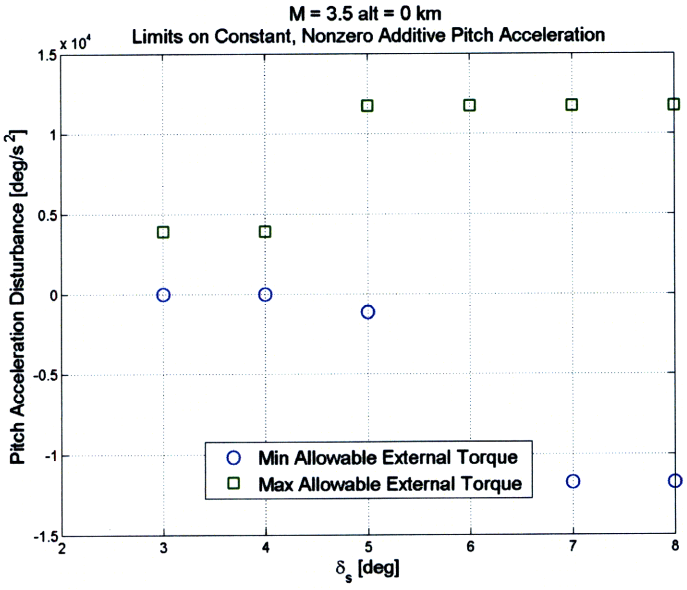

Figure 3.26: Robustness to external pitch acceleration, step command from 0 to 10 degrees, Mach 3.5, 0 km altitude, actuator and lead compensator modeled

3.3.6 LQ-servo Performance at M = 6.3, 20 km Altitude

The time response summary for Mach 6.3, 20 km altitude is presented in Figure 3.27. The 6 degree δ_s configuration is unstable for commands greater than 7 degrees, and

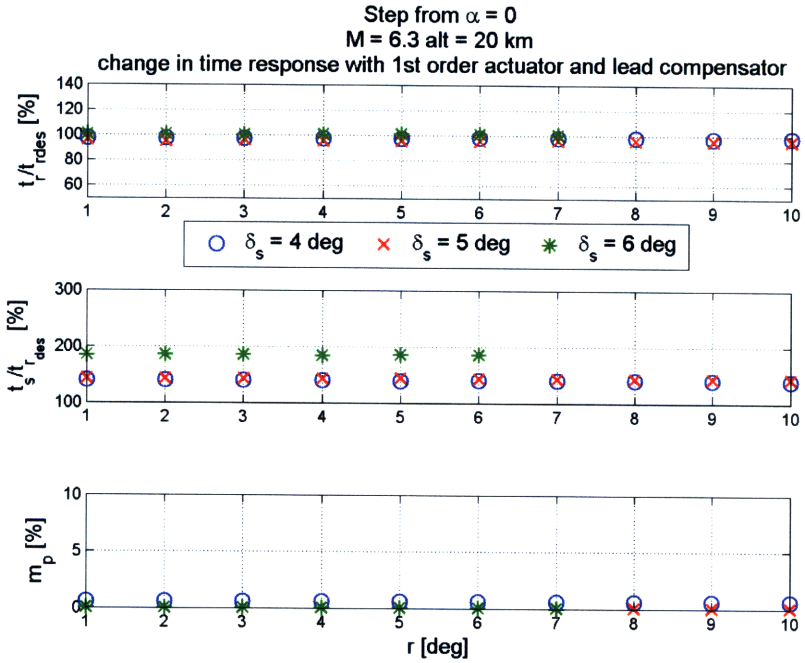

Figure 3.27: Time response characteristics for step commands from 0 degrees, Mach 6.3, 20 km altitude, actuator and lead compensator modeled

the large settling time at 7 degrees indicate this case is highly oscillatory. The cases for 4 and 5 degrees of symmetric deflection show little variation in rise time, settling time, or peak overshoot for the range of step commands presented. Peak overshoots are minimal.

The robustness to center of pressure variation and control effectiveness for 1 and 10 degree steps is shown in Figure 3.28 and 3.29. From a stability point of view, symmetric deflections of 7 and 8 degrees provide the greatest robustness to

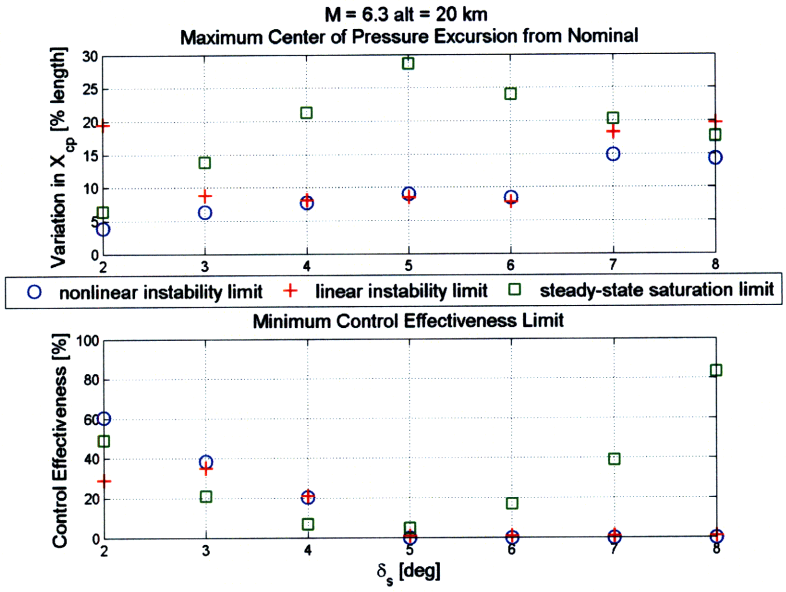

Figure 3.28: Allowable variation in center of pressure location and reduction in control effectiveness, step command from 0 to 1 degree, Mach 6.3, 20 km altitude, actuator and lead compensator modeled

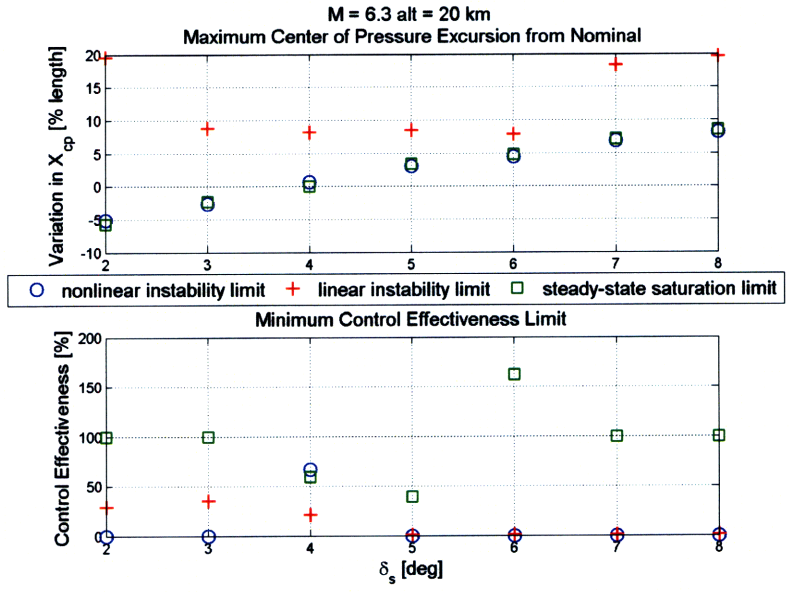

Figure 3.29: Allowable variation in center of pressure location and reduction in control effectiveness, step command from 0 to 10 degrees, Mach 6.3, 20 km altitude, actuator and lead compensator modeled

variation in static margin when reference commands are small. However, Figure 3.28 also demonstrates that a reduction in control surface effectiveness (i.e., control surface ablation) for δ_s greater than 5 degrees can result in control surface saturation before instability is reached, even for a 1 degree reference command. In such a configuration, the vehicle would remain stable but unable to track the reference command.

For a step command from 0 to 10 degrees, 2 and 3 degrees of symmetric deflection are unstable (negative value of variation in X_{cp}), while over 5 degrees of symmetric deflection are stable but require over 100% control effectiveness to meet steady-state tracking requirements. The 10 degree step responses for three symmetric deflections are shown in Figure 3.30. For 6 degrees of symmetric deflection, the

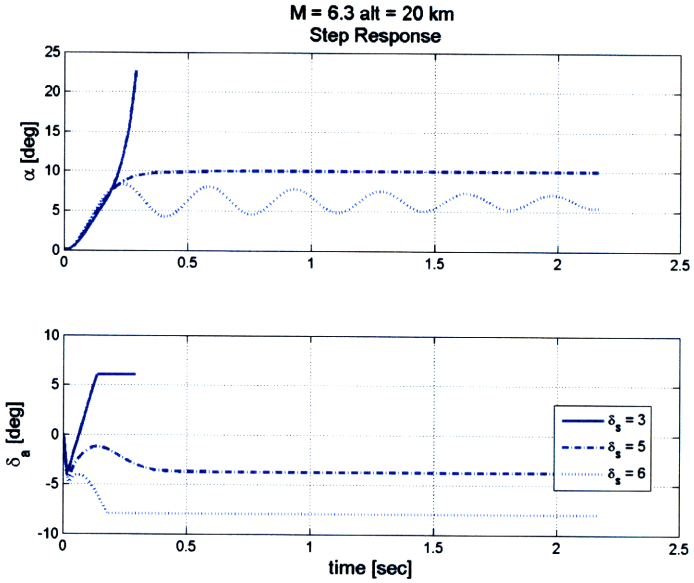

Figure 3.30: 10 degree step response, Mach 6.3, 20 km altitude, actuator and lead compensator modeled

flaps saturate and control system is unable to provide any additional damping to the statically stable system, resulting in oscillations and inability to track the reference command.

The vehicle's robustness to external pitch accelerations for both 1 and 10 degree step commands is summarized in Figure 3.31 and 3.32. For the 1 degree step, a minimum pitch acceleration rejection band is still present between 3 and 4 degrees of symmetric deflection. For a 10 degree step, symmetric deflections greater 5 degrees provide similar levels of external pitching moment rejection.

In the face of plant uncertainty, small reference commands may be better suited to symmetric deflections of 7–8 degrees, while large reference commands clearly favor 5 degrees of symmetric deflection.

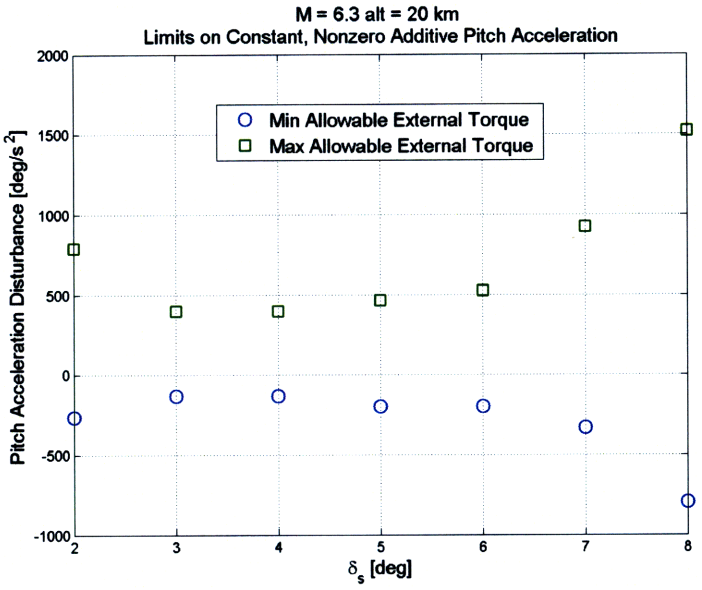

Figure 3.31: Robustness to external pitch acceleration, step command from 0 to 1 degrees, Mach 6.3, 20 km altitude, actuator and lead compensator modeled

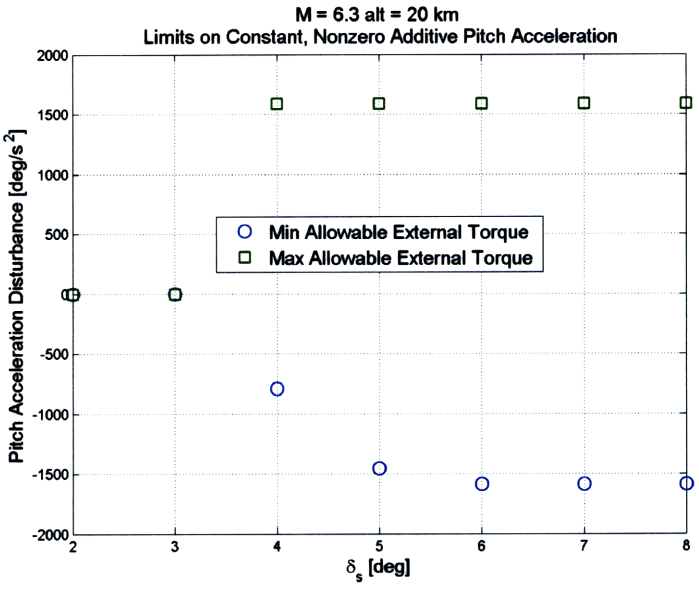

Figure 3.32: Robustness to external pitch acceleration, step command from 0 to 10 degrees, Mach 6.3, 20 km altitude, actuator and lead compensator modeled

3.3.7 LQ-servo Performance at M = 5.3, 50 km altitude

The time response summary for Mach 5.3, 50 km altitude with both the actuator and lead compensator modeled is shown in Figure 3.33. The low dynamic pressure still

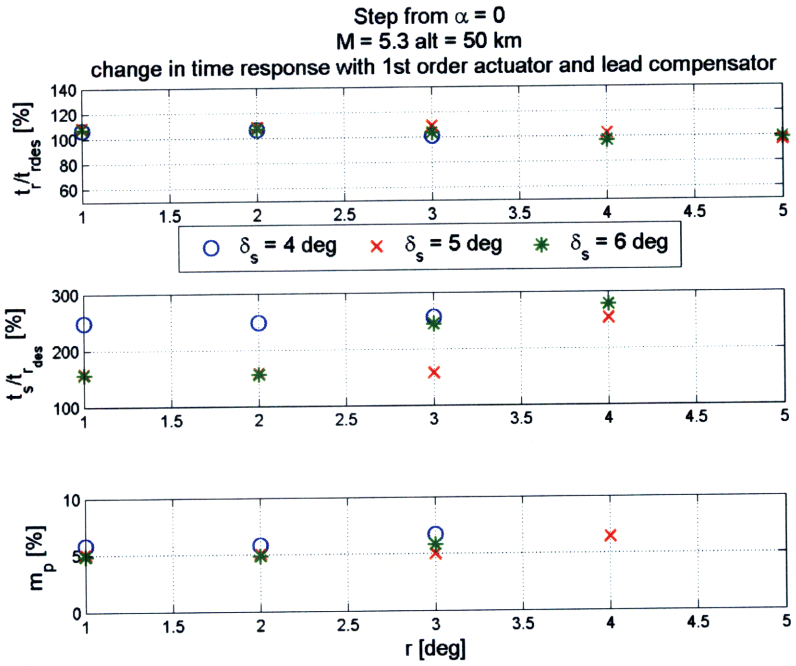

Figure 3.33: Time response characteristics for step commands from 0 degrees, Mach 5.3, 50 km altitude, actuator and lead compensator modeled

limits the maximum reference command to 5 degrees. The settling times and peak responses demonstrate marked increases as the magnitude of the reference command increases.

Figure 3.34 demonstrates a slight advantage to δ_s of 5 degrees for off-nominal static margins, while Figure 3.35 shows no change in external pitch acceleration robustness. Figure 3.35 also shows the system is poorly-suited to cope with external torques at the Mach 5.3, 50 km altitude flight condition. The robustness to center

of pressure variation appears to be highly correlated with control surface saturation limits. At 50 km, low dynamic pressure severely limits control authority, and controls are more likely to saturate than at higher dynamic pressures.

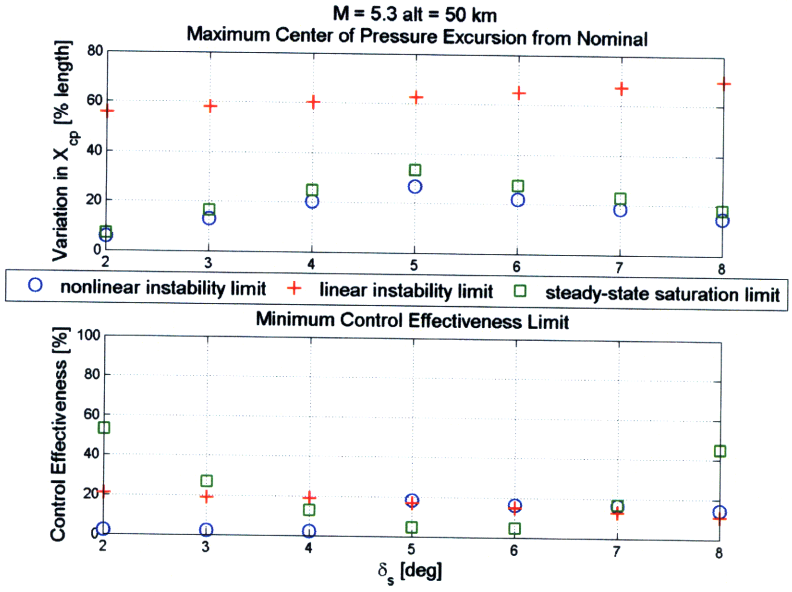

Figure 3.34: Allowable variation in center of pressure location and reduction in control effectiveness, step command from 0 to 1 degree, Mach 5.3, 50 km altitude, actuator and lead compensator modeled

In terms of tracking performance, this flight condition represents the most difficult case. The vehicle is only able to track small reference commands. Robustness is markedly lower at this flight condition. However, ablation effects may be negligible at this point during the reentry since dynamic pressures are low. It is possible large changes in angle of attack are not likely to be commanded at this phase of reentry. On the other hand, the guidance system is likely to command a constant, near-zero angle of attack until higher dynamic pressures and external sensor feedback (i.e., GPS, etc.) are available to command more aggressive trajectories. The guidance scheme for such a reentry vehicle must consider this limitation, especially if a linear controller is employed.

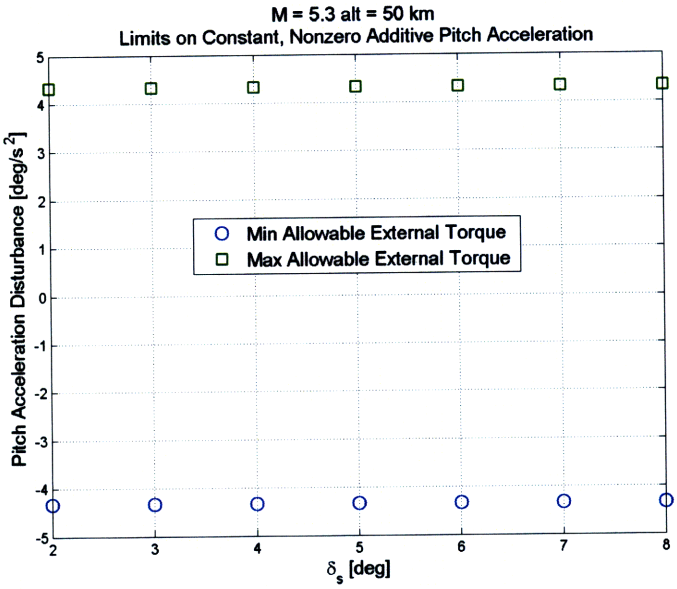

Figure 3.35: Robustness to external pitch acceleration, step command from 0 to 1 degree, Mach 5.3, 50 km altitude, actuator and lead compensator modeled

3.4 Linear Control Conclusions

The linear controller tracked small commanded angles of attack well when the vehicle aerodynamics are well known. The addition of a 1st order actuator reduced performance when vehicle dynamics are fast (e.g., at 0 km altitude), but a lead compensator demonstrated its ability to recover much of the actuator-induced phase lag. The controller handled some degree of control effectiveness reduction. However, variations in static margin, either from poorly-modeled center of pressure or movement in the center of gravity from ablation, limited the effectiveness of the LQ-servo controller. Much of the LQ-servo robust performance difficulties arose from saturation in the control surface deflections—this nonlinearity is hard to overcome with a linear SISO system. The control saturations are reached when larger angles of attack are commanded, especially at low dynamic pressures. The remainder of this effort sought to improve the performance over the LQ-servo controller.

At this point, the linear controller for each Mach/altitude combination is fixed to provide a "baseline" to evaluate other controllers. At each flight condition, Table 3.2 shows the selected symmetric deflection: While somewhat arbitrary, an emphasis

Table 3.2: Selected δ_s for each flight condition

Mach	altitude (km)	δ_s [deg]
3.5	0	8
6.3	20	5
5.3	50	5

is placed on time response and robustness to static margin uncertainty (allowable variation in X_{cp}). In any case, an "optimal" value of symmetric deflection for the LQ-servo controller can be further investigated in the future, possibly improving the performance of the control schemes presented later in this effort.

Chapter 4

Hybrid Switching-Linear Controller

The baseline Linear Quadratic Servo (LQ-servo) controller presented in Chapter 3 performed well for small step commands in the presence of perfect plant uncertainty. However, control saturation limits presented nonlinearities that limited tracking performance or introduced instabilities to the system. In an effort to exploit the performance of the LQ-servo controller but gain robust performance, a multi-mode, hybrid switching-linear controller (SLC) is developed.

4.1 Motivation

The difficulty of the linear controller commanding large steps in α lies in switching from one saturated command to the other. Many of the trajectories greatly exceed

10 degrees angle of attack. In Section 2.1, the aerodynamic model was only assumed valid for $|\alpha| \leq 10$ degrees. Consequently, these large overshoots may pose a significant problem. Consider the phase plane for a 10 degree angle of attack reference command (Figure 4.1). The trajectory that begins at 5 degrees angle of attack is of particular

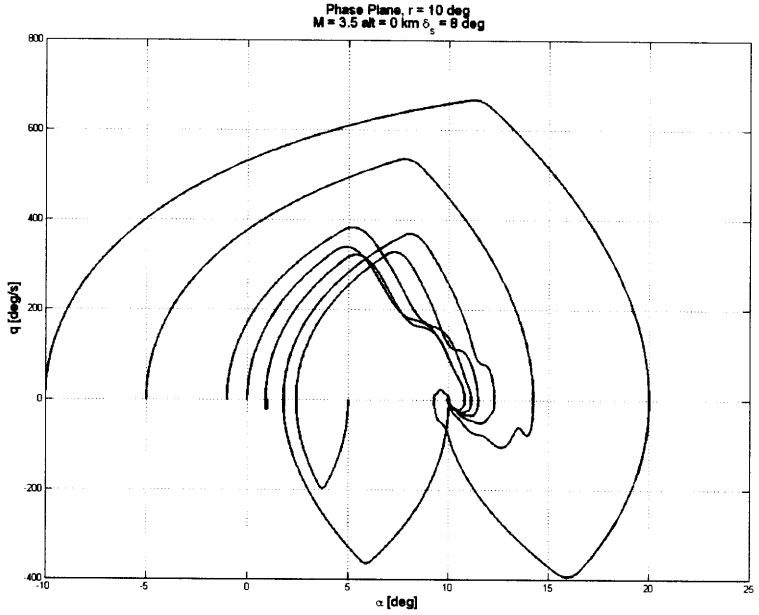

Figure 4.1: Phase plane for 10 degree reference command, M = 3.5, 0 km altitude, $\delta_s = 8$ degrees

interest. The initial behavior is in the "wrong direction"; that is, the initial behavior of the vehicle is to begin a *negative* pitch rate, even though a positive pitch rate is clearly desirable to increase the angle of attack to 10 degrees. Additionally, the control switches between saturation limits twice before remaining within the control deflection bounds (see Figure 4.2). As a result, the peak overshoot is significant, as is control activity. This "wrong direction" behavior results from the tracking error integral, e_I, being initialized to zero. It must "wind up" enough to trim the vehicle at 10 degrees. The zero initial condition is sufficient when the initial angle of attack is likewise zero, but nonzero initial angles of attack must initialize e_I at a nonzero value. The LQ-servo controller previously developed does not have a mechanism to accomplish this.

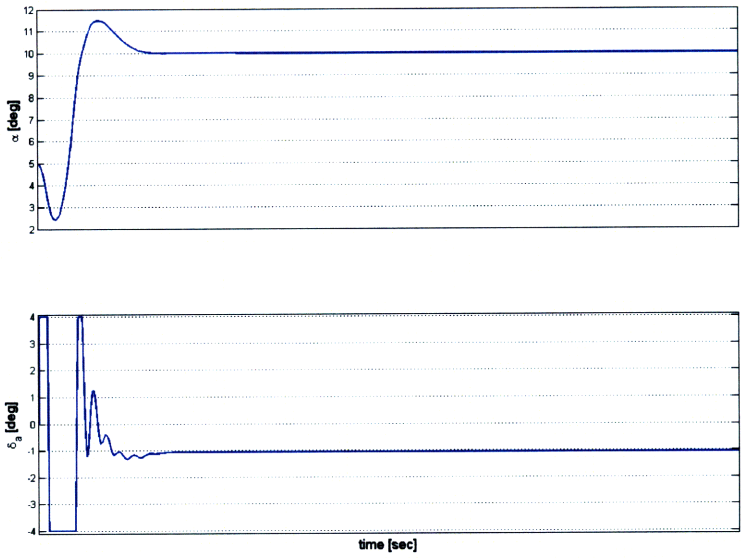

Figure 4.2: Step response from 5 to 10 degrees, M = 3.5, 0 km altitude, δ_s = 8 degrees

The SLC developed has two distinct modes. The first mode is completely saturated control at either the positive or negative limit of δ_a. Switching between these two is based on a switching curve in the phase plane. The second mode is the LQ-servo controller previously developed, with the switch occurring along another curve in the phase plane. The qualitative control strategy is to drive the phase plane trajectory as rapidly as possible into the LQ-servo control region, which causes the system to converge to the reference command. The advantage of this approach is that small commands take advantage of the linear controller's performance and robustness, while larger commands bypass the linear controller when it would be saturated and possibly near instability or a limit cycle.

4.2 Phase Plane Analysis

For each flight condition with the linear controller in place, the phase plane of initial conditions can be subdivided into three stable regions. The first region is stable with satisfactory tracking performance but possibly saturated controls during the transient response. Here, "satisfactory" tracking performance is defined by two criteria:

- rise time (10% to 90% of commanded value) meets specification, within 5%
- settling time (between 95% and 105% of commanded value) less than 4 rise times

The second region is stable, but does not meet the tracking parameters specified above. The third region is denoted by totally unsaturated controls. This last region represents a completely linear system; as such, the inherent LQR stability margins apply (see Section 3.1). Admittedly, this final region is very small in relation to the other regions, often appearing as a line segment. The 5 and 10 degree reference commands at Mach 5.3, 50 km altitude do not show regions of unsaturated control.

These three regions can be seen in Figures 4.3-4.5. Unstable initial conditions are those points without any marker.

A controller can exploit the unsaturated control conditions if all trajectories could be controlled to this region. It is interesting to note the unsaturated region does not necessarily correspond with the commanded angle of attack, especially with large reference commands. Recall, the states α and q were augmented with the integral

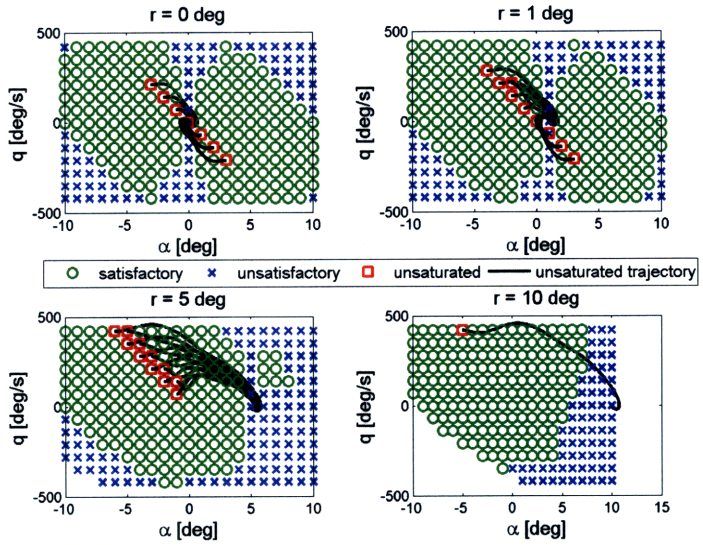

Figure 4.3: Phase plane of stable initial conditions, LQ-servo, M = 3.5, 0 km altitude, δ_s = 8 degrees

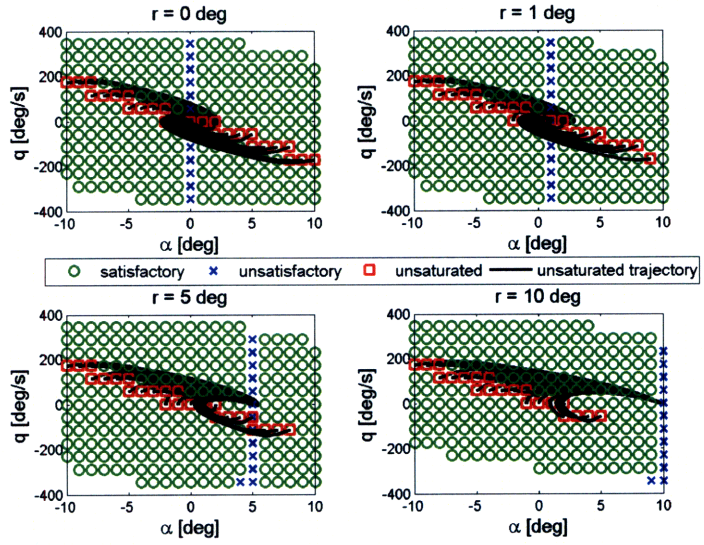

Figure 4.4: Phase plane of stable initial conditions, LQ-servo, M = 6.3, 20 km altitude, δ_s = 5 degrees

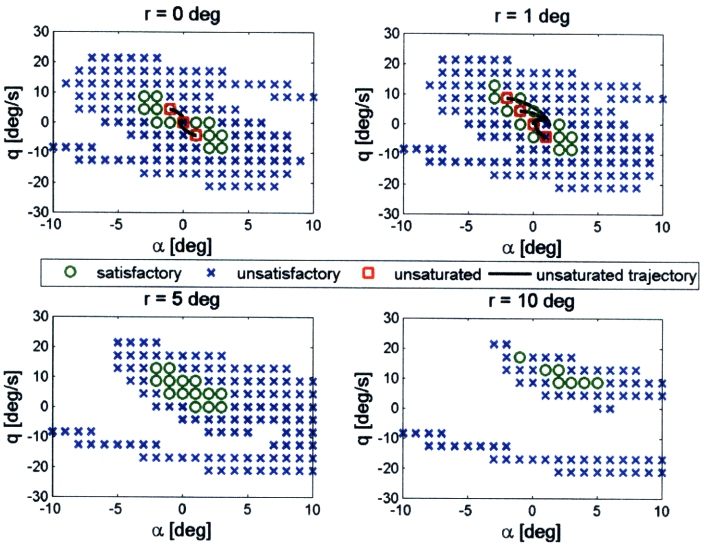

Figure 4.5: Phase plane of stable initial conditions, LQ-servo, M = 5.3, 50 km altitude, δ_s = 5 degrees

of the tracking error, e_I (Equation 3.17). Thus, the phase plane is actually three dimensional. Consider the α-e_I phase plane presented in Figure 4.6. Regardless of the initial angle of attack, all stable trajectories converge to a single, steady-state value of e_I. Compare Figure 4.6 and Figure 4.7, which is for a 10 degree reference command. The steady-state value of e_I is nonzero, but stable trajectories still converge to a point in the 3-dimensional state space. For convergence to a constant reference command, the steady-state value of q is always zero.

While these phase plane trajectories are three dimensional, the third dimension is a software state. That is, e_I can be initialized to any value desired. As noted in Section 4.1, the LQ-servo controller does not have a method to initialize e_I to nonzero values.

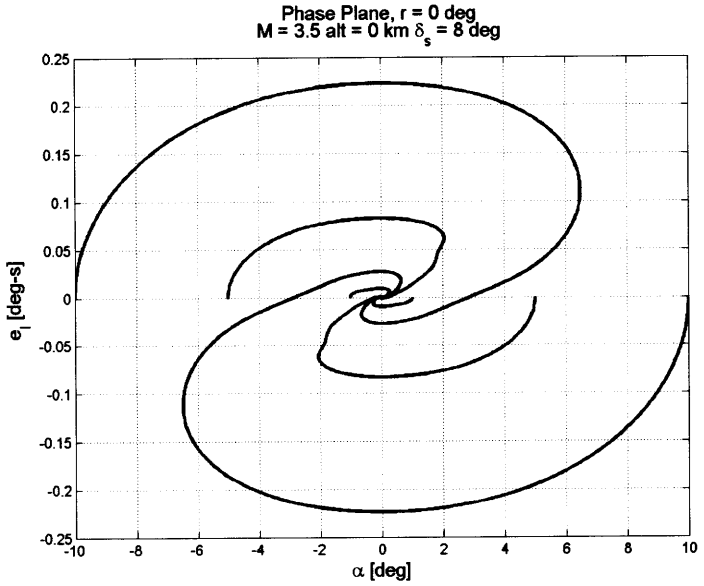

Figure 4.6: Zero pitch rate phase plane, e_I vs α for a 0 degree reference command, M = 3.5, 0 km altitude, δ_s = 8 degrees

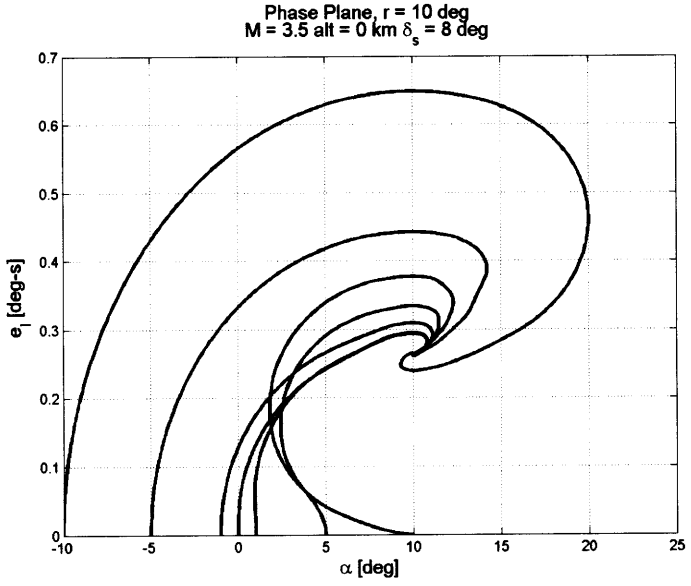

Figure 4.7: Zero pitch rate phase plane, e_I vs α for a 10 degree reference command, M = 3.5, 0 km altitude, δ_s = 8 degrees

4.3 Switching Control Design

To improve upon the LQ-servo's performance in tracking large step commands, a Switching Linear Controller (SLC) was developed. The SLC employed one of two control strategies. The first strategy employed a saturated nonlinear controller. Its purpose is to rapidly position the system to a state where the linear controller performs well. The second control strategy was the previously-developed LQ-servo controller, with an appropriate initialization of the state e_I.

Observing Figures 4.3, 4.4, and 4.5, a negative trend is apparent through the unsaturated control region of initial conditions. If the phase plane trajectory reaches these points, it converges *without control saturation* to the reference condition. Decreasing initial values of α indicate increased initial values in initial q and vice versa. For example, Figure 4.3, $r = 0$, shows a narrow region of unsaturated controls that intersects the points (-3°,250°/s), (0°,0°/s), and (3°,-250°/s). Similarly, the additional flight conditions and reference commands demonstrate regions where increasing α strictly decreases q. A linear approximation of this trend gives

$$q^* = m^*(\alpha - r) \tag{4.1}$$

where m^* is the slope of the switching line. Given a state $[\alpha \quad q]$, the value of q^* can be calculated. If $q > q^*$, the control should be $\delta_{a_{max}}$, while $q < q^*$ indicates the control should be $-\delta_{a_{max}}$. The purpose of this control is to drive the trajectory to the linear region as quickly as possible. This is similar to the classic minimum-time problem in constrained optimal control (e.g., [18]).

The centroid of the unsaturated control region (arithmetic mean of all points within this region) varies with the value of the reference command. Let the centroid

offset from the origin, $[\alpha^c \quad q^c]^T$, be

$$\begin{bmatrix} \alpha^c \\ q^c \end{bmatrix} = \begin{bmatrix} \Delta_\alpha \\ \Delta_q \end{bmatrix} r \tag{4.2}$$

Since this centroid is within the unsaturated control region of initial conditions, initializing e_I to zero results in a satisfactory time response.

At this point, it may be reasonable to expect another curve defines the reset of the error integral, e_I. That is, the q^* curve defines the switch between saturated controllers, while a separate curve defines the initialization of the LQ-servo controller state e_I (integrated tracking error). Defining this integral reset curve as the line that passes through $[\alpha^c \quad q^c]^T$ and $[r \quad 0]^T$ (the reference command) gives

$$q^s = \frac{\Delta_q}{\Delta_\alpha - 1}(\alpha - r) \tag{4.3}$$

While the saturated nonlinear controller is active, the state e_I is irrelevant. However, e_I must be properly initialized upon intersection with the q^s curve. To accomplish this, assume the steady-state value of the error integral, designated e_{I_f}, is a linear function of the reference command:

$$e_{I_f} = \epsilon r \tag{4.4}$$

Note Equation 4.4 is nonzero only for nonzero values of reference commands, which agrees with Figures 4.6 and 4.7.

Now, e_{I_0} must be parameterized along the reset line, q^s. At the reference condition, $e_{I_0} = e_{I_f} = \epsilon r$. At the point $[\alpha^c \quad q^c]^T$ (unsaturated region centroid), $e_{I_0} = 0$. The initialization of the error integral, e_{I_0}, is then

$$e_{I_0} = \frac{\epsilon}{1 - \Delta_\alpha}(\alpha - \Delta_\alpha r) \tag{4.5}$$

Upon implementation, trajectories are controlled by the saturated control until the phase plane trajectory intersects the q^s curve (Equation 4.3). At this point, the error integral state, e_I, is initialized to the value determined by Equation 4.5; the linear controller then controls the trajectory to the reference command. In practice, the initial nonlinear control is resumed each time the reference trajectory changes:

$$\frac{\partial r}{\partial t} \neq 0$$

This reset limits the guidance commands to constant angles of attack (step commands), and the frequency of these steps must be sufficiently low so steady-state tracking can be achieved. However, the controller reset method can be altered in the future to match the implemented guidance scheme.

A challenge of switching controllers occurs when the control input "chatters" along the switching boundary, oscillating between the minimum and maximum deflections. Presumably, this control chattering could continue without the control architecture switching to the linear controller, as in Figure 4.8. This chattering can be remedied by setting the switching curve slope, m^* (see Equation 4.1), to the slope of the q^s curve (Equation 4.3). Effectively, this prevents the control from switching between saturated deflections by defining one switching curve. One initially saturated input controls the phase plane trajectories, followed by a switch (along the common q^*-q^s switching curve) to the linear controller with proper initialization of e_I.

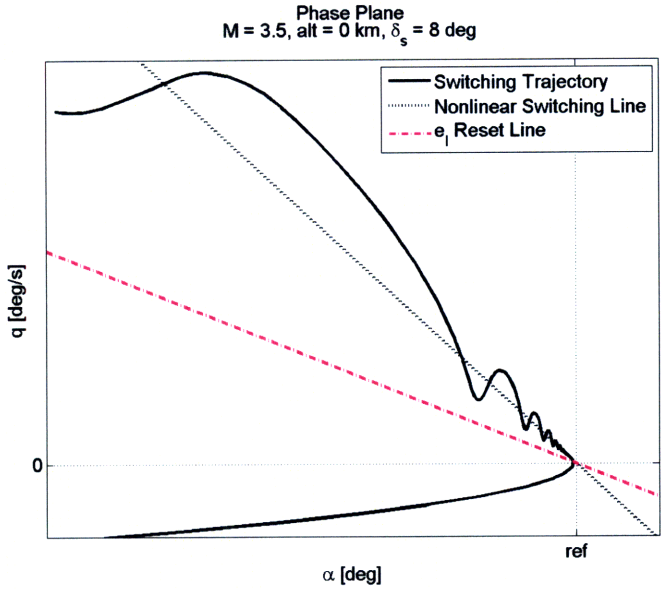

Figure 4.8: Phase plane showing chattering about switching line, M = 3.5, 0 km altitude, $\delta_s = 8$ degrees

4.4 Results

Simulations were conducted to evaluate the relative performance of the Switching Linear Controller (SLC) and the Linear Quadratic Servo (LQ-servo) controller. All simulations were conducted in MATLAB/SIMULINK using the built-in ODE15s solver. [15][16]

4.4.1 Mach 3.5, 0 km altitude

Once again, consider a step from 5 degrees to 10 degrees for the Mach 3.5, 0 km altitude flight condition. The phase planes for the LQ-servo controller and SLC are

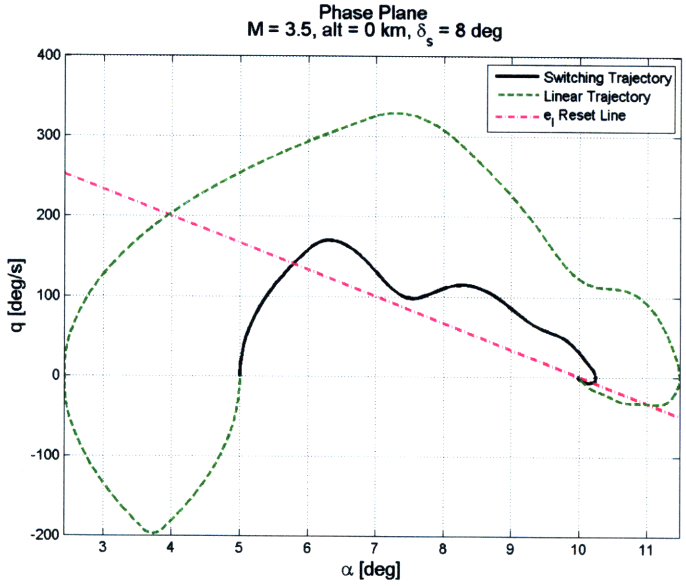

Figure 4.9: Phase plane, SLC and LQ-servo, Mach 3.5, 0 km altitude, $\delta_s = 8$ degrees

presented in Figure 4.9. The initial negative pitch rate is eliminated, as is a significant portion of the overshoot. The time responses are compared in Figure 4.10. Since the linear controller initializes e_I to 0, this integral must "wind up" enough to maintain a nonzero angle of attack. When the commanded angle of attack is greater than this initial angle of attack, the linear controller will tend to return to 0 degrees angle of attack until e_I reaches a sufficient value to overcome this negative pitch rate. The SLC eliminates this "wind up" by directly initializing e_I to an appropriate value. As expected, δ_a saturates until the phase plane trajectory intersects the e_I reset curve, when the LQ-servo controller is activated. Control activity is reduced over the linear controller, as is the peak overshoot and settling time.

Consider the especially difficult case of a step from -10 degrees to 10 degrees, presented in Figure 4.11. The magnitude of the peak overshoot is reduced approximately 90%, resulting in a much more favorable time response for the SLC. Furthermore, the peak overshoot extends very little into angle of attacks greater than 10 degrees, where the aerodynamic model may break down.

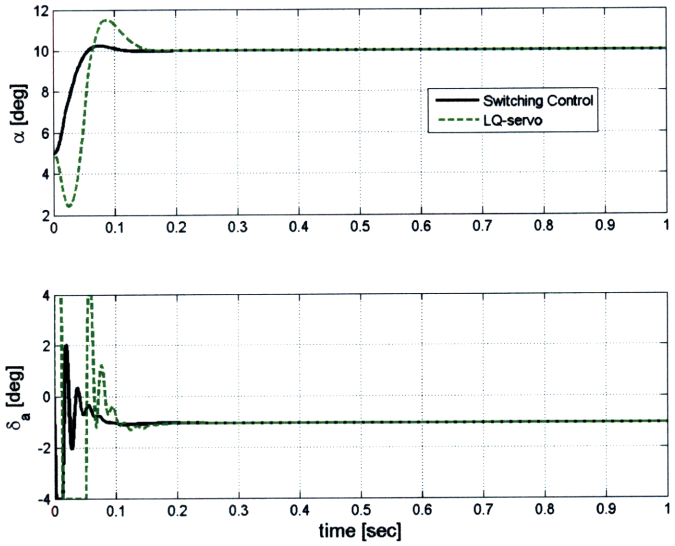

Figure 4.10: Time response to a step command from 5 to 10 degrees, SLC and LQ-servo, Mach 3.5, 0 km altitude, $\delta_s = 8$ degrees

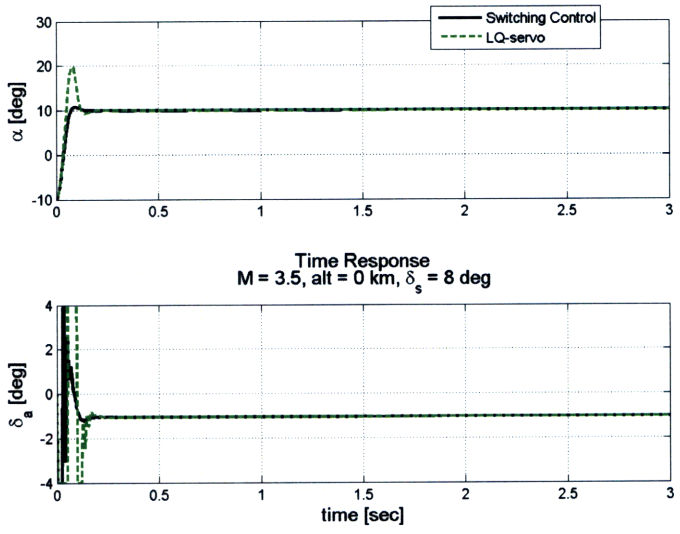

Figure 4.11: Time response to a step command from -10 to 10 degrees, SLC and LQ-servo, Mach 3.5, 0 km altitude, $\delta_s = 8$ degrees

Although the switching controller improved the time response characteristics over the LQ-servo controller, it did not provide significant robustness benefits at Mach 3.5 and 0 km altitude. Since the SLC incorporated the previously developed LQ-servo control scheme, the LQ-servo robustness bounds affect the SLC robustness bounds. Figure 4.12 summarizes the stability limits of center of pressure uncertainty and reduced control surface effectiveness.

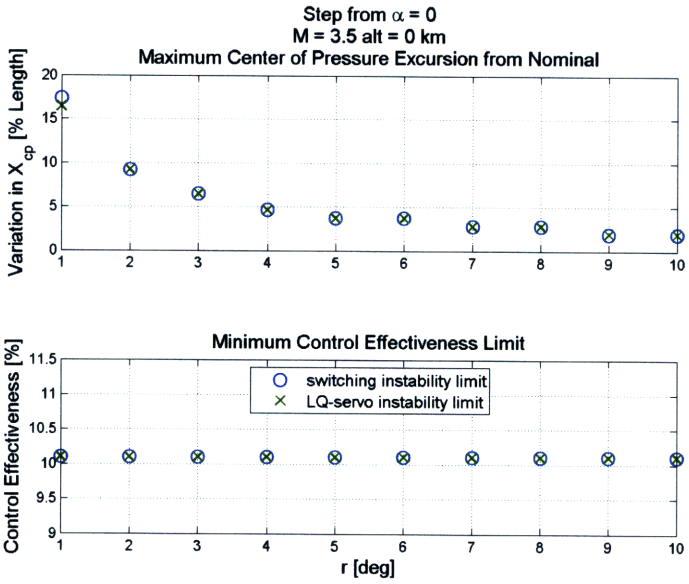

Figure 4.12: Robustness comparison of the SLC and LQ-servo from $\alpha = 0$ deg for various reference commands, Mach 3.5, 0 km altitude, $\delta_s = 8$ degrees

A summary of the improvement in rise time, settling time, and peak overshoot is presented in Figure 4.13. Rise times increased slightly, but settling times were reduced to 60 percent of the LQ-servo settling time. The SLC also provided a slight reduction in peak overshoot.

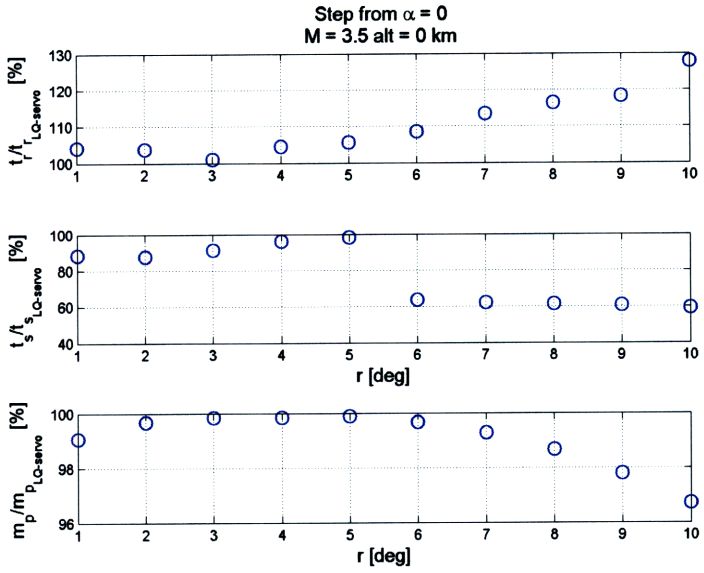

Figure 4.13: Time response characteristics for the SLC as a percent of the LQ-servo Characteristics for various step commands from 0 degrees, Mach 3.5, 0 km altitude, $\delta_s = 8$ degrees

4.4.2 Mach 6.3, 20 km altitude

For 5 degrees of symmetric deflection, a step command from 0 to 10 degrees was tracked well by the LQ-servo controller (see Figure 3.30). The SLC matched this performance well (Figures 4.14 and 4.15), but improved on the performance of a step from 5 to 10 degrees (Figures 4.16 and 4.17). This highlights the elimination in the "wind up" period describes in Section 4.4.1.

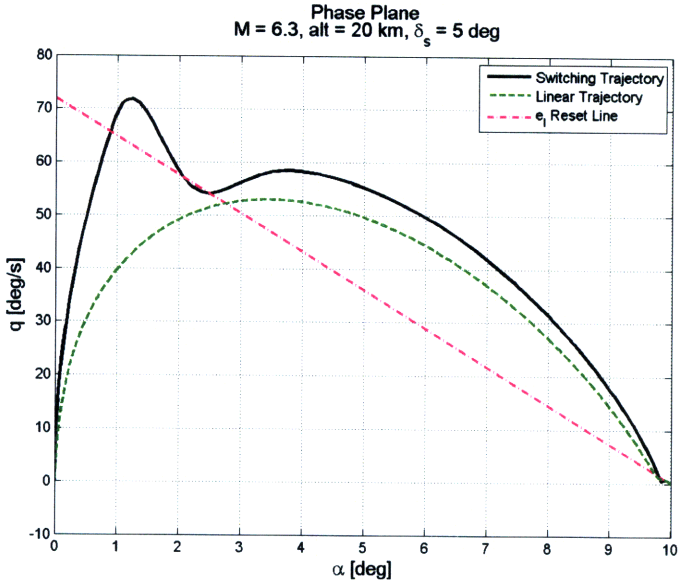

Figure 4.14: Phase plane, step command from 0 to 10 degrees, SLC and LQ-servo, M = 6.3, 20 km altitude, $\delta_s = 5$ degrees

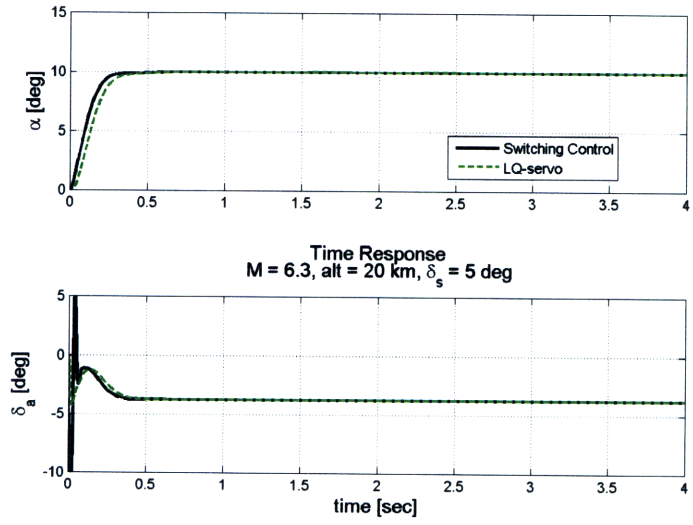

Figure 4.15: Time response to a step command from 0 to 10 degrees, SLC and LQ-servo, Mach 6.3, 20 km altitude, $\delta_s = 5$ degrees

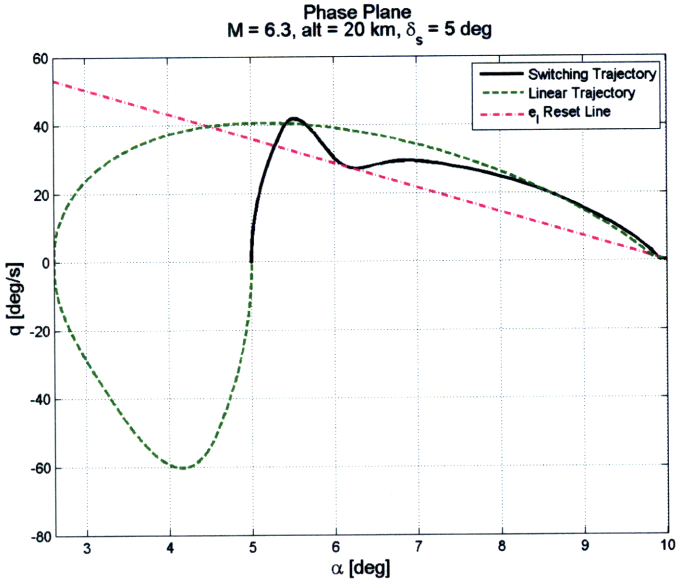

Figure 4.16: Phase plane, step command from 5 to 10 degrees, SLC and LQ-servo, Mach 6.3, 20 km altitude, $\delta_s = 5$ degrees

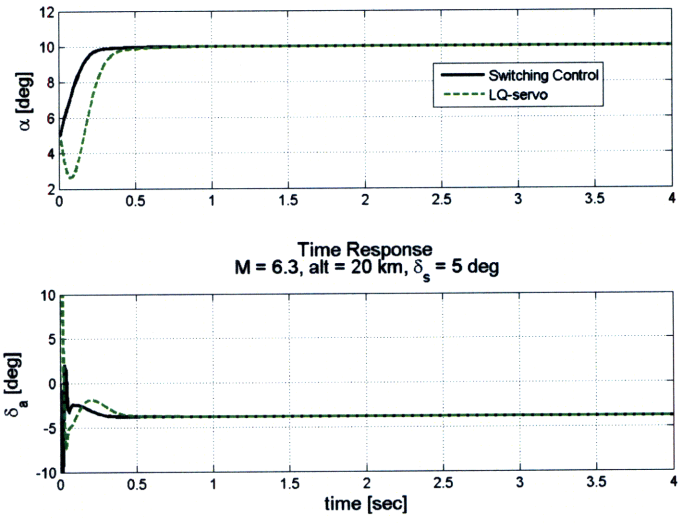

Figure 4.17: Time response to a step command from 5 to 10 degrees, SLC and LQ-servo, Mach 6.3, 20 km altitude, $\delta_s = 5$ degrees

When commanding a step from -10 to 10 degrees, the LQ-servo's overshoot is eliminated with the SRC (Figures 4.18 and 4.19).

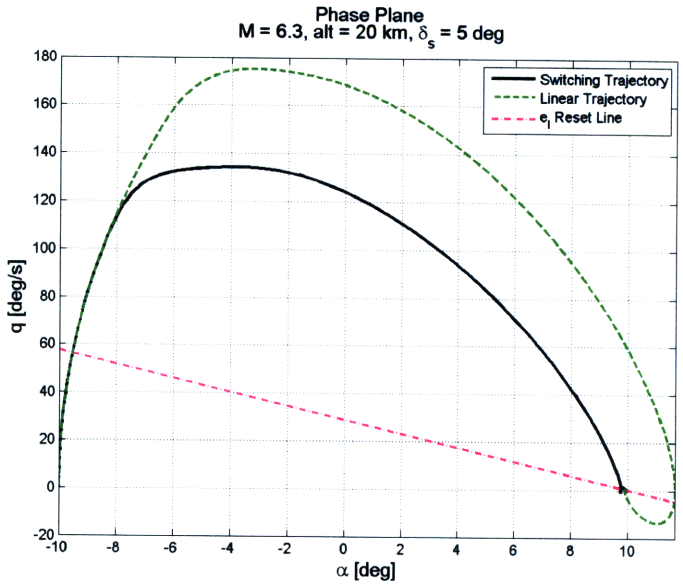

Figure 4.18: Phase plane, step command from -10 to 10 degrees, SLC and LQ-servo, Mach 6.3, 20 km altitude, $\delta_s = 5$ degrees

The SLC did not provide any additional robustness over the LQ-servo controller; a summary of the allowable center of pressure excursion and control effectiveness reduction is shown in Figure 4.20

A summary of the improvement in rise time, settling time, and peak overshoot is presented in Figure 4.21. Except for the 1 degree step, the rise times and settling times were reduced up to 15 and 30 percent, respectively. Peak responses were almost unchanged.

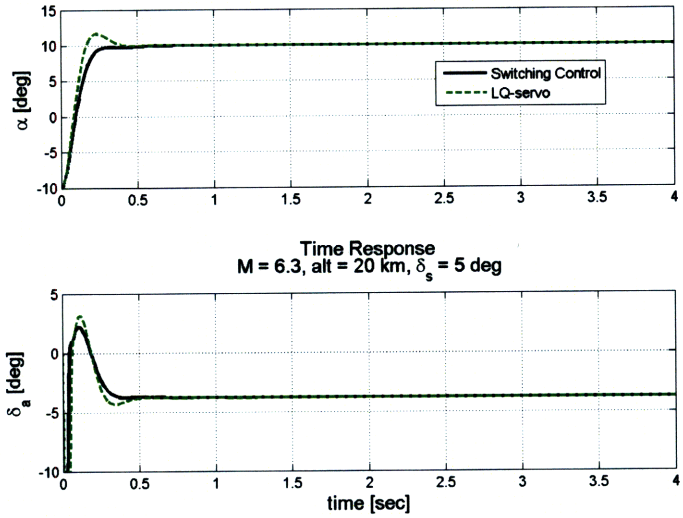

Figure 4.19: Time response to a step command from -10 to 10 degrees, SLC and LQ-servo, Mach 6.3, 20 km altitude, $\delta_s = 5$ degrees

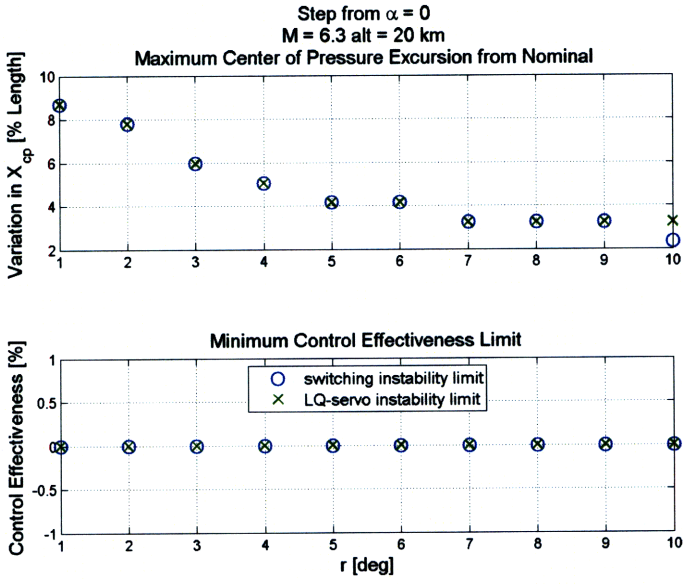

Figure 4.20: Robustness comparison of the SLC and LQ-servo from $\alpha = 0$ deg for various reference commands, Mach 6.3, 20 km altitude, $\delta_s = 5$ degrees

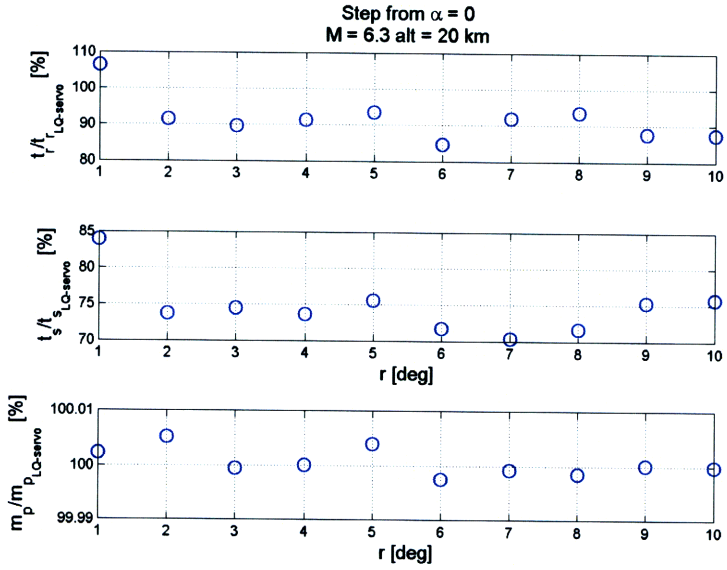

Figure 4.21: Time response characteristics for the SLC as a percent of the LQ-servo Characteristics for various step commands from 0 degrees, Mach 6.3, 20 km altitude, $\delta_s = 5$ degrees

4.4.3 Mach 5.3, 50 km altitude

Consider a step command from 0 to 5 degrees at Mach 5.3, 50 km altitude. The phase plane and time responses for the LQ-servo and SLC are shown in Figures 4.22 and 4.23, respectively. Although the SLC increased the rise time from the LQ-servo,

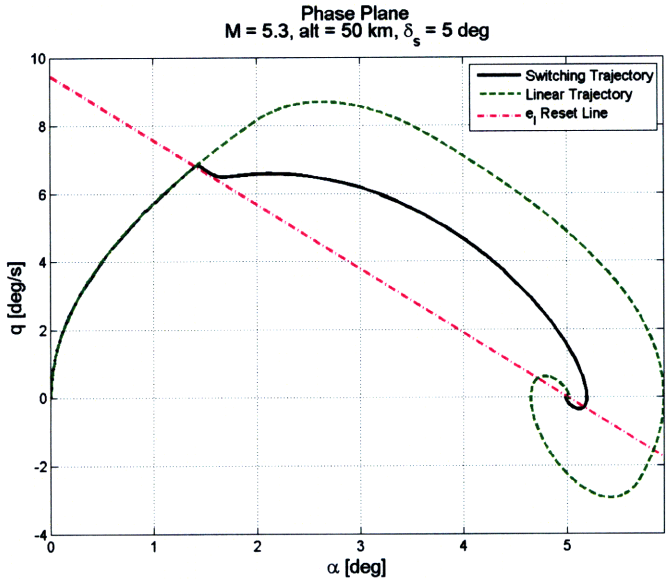

Figure 4.22: Phase plane, step command from 0 to 5 degrees, SLC and LQ-servo, M = 5.3, 50 km altitude, $\delta_s = 5$ degrees

settling time and peak overshoot were sharply reduced.

Recall the LQ-servo controller was unable to stabilize a step from 0 to 10 degrees (see Section 3.3.7). The SLC does stabilize and track a 10 degree step, albeit after a long transient period. In fact, the SLC provides a measure of robustness at Mach 5.3 and 50 km altitude when large steps are commanded, although robustness at smaller reference commands is somewhat diminished (Figure 4.26).

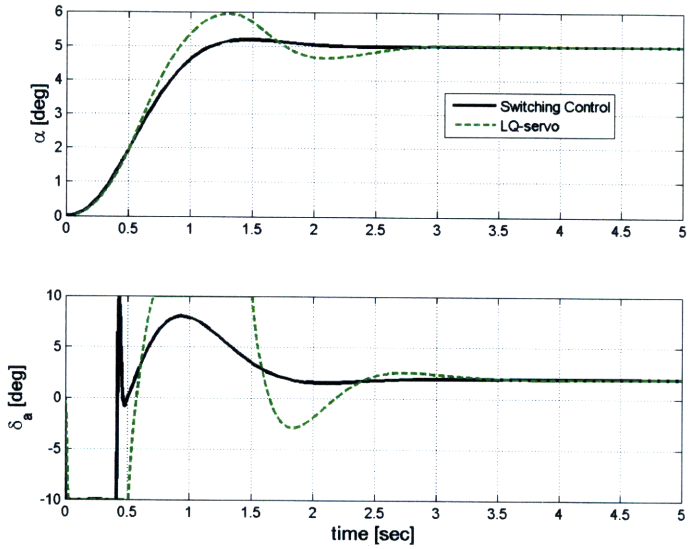

Figure 4.23: Time response to a step command from 0 to 5 degrees, SLC and LQ-servo, M = 5.3, 50 km altitude, δ_s = 5 degrees

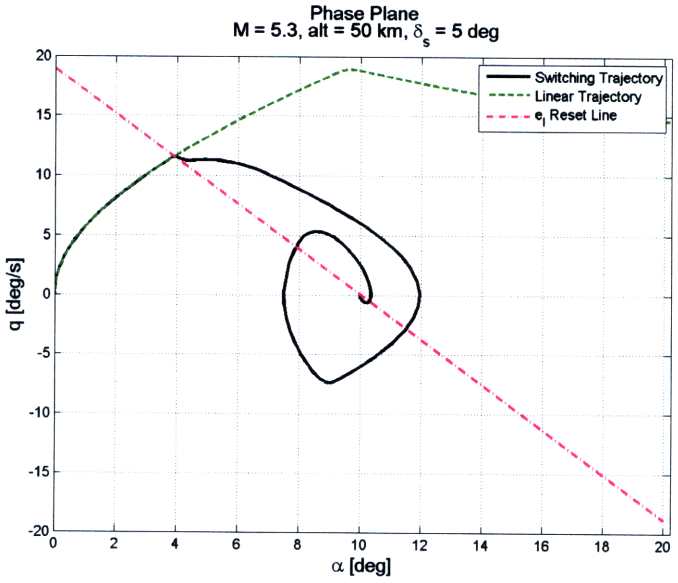

Figure 4.24: Phase plane, step command from 0 to 10 degrees, SLC and LQ-servo, M = 5.3, 50 km altitude, δ_s = 5 degrees

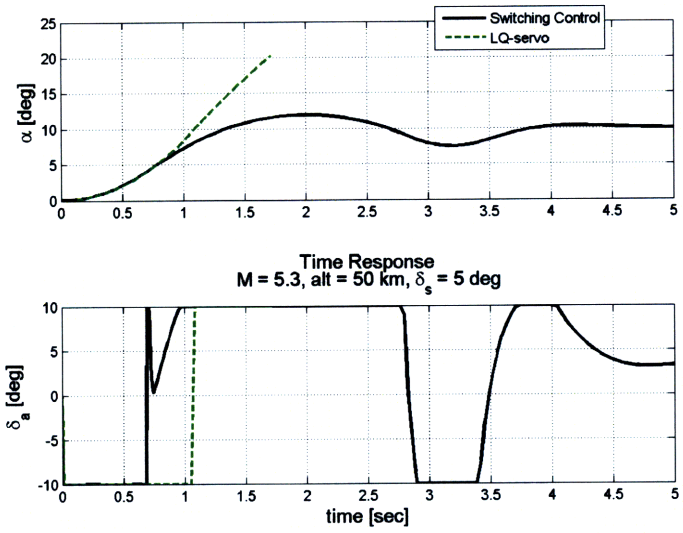

Figure 4.25: Time response to a step command from 0 to 10 degrees, SLC and LQ-servo, M = 5.3, 50 km altitude, $\delta_s = 5$ degrees

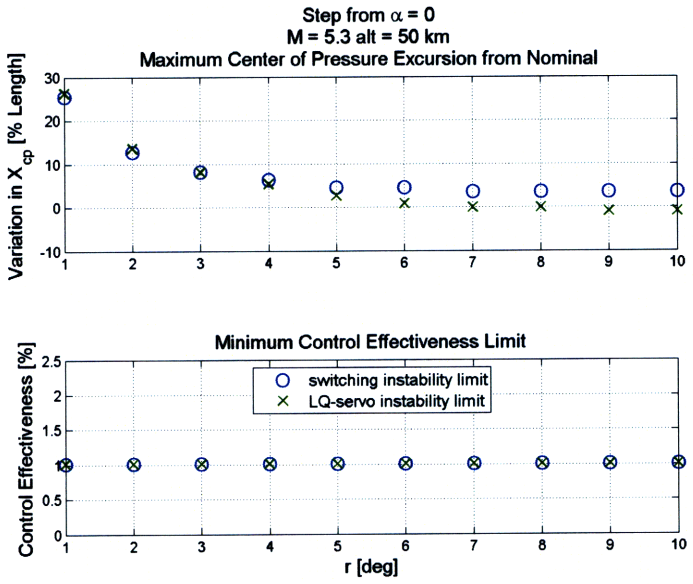

Figure 4.26: Robustness comparison of the SLC and LQ-servo from $\alpha = 0$ deg for various reference commands, M = 5.3, 50 km altitude, $\delta_s = 5$ degrees

A summary of the improvement in rise time, settling time, and peak overshoot is presented in Figure 4.27. The SLC tends to increase rise times for values of r

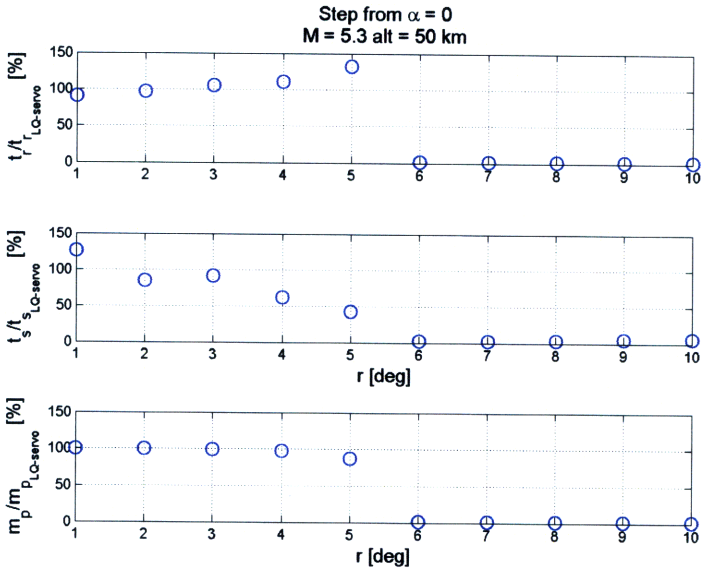

Figure 4.27: Time response characteristics for the SLC as a percent of the LQ-servo characteristics for various step commands from 0 degrees, Mach 5.3, 50 km altitude, $\delta_s = 5$ degrees

between 3 and 5 degrees, but settling time is significantly reduced. The LQ-servo controller was unable to track step commands above 5 degrees without instability; this is reflected in the near zero-values of rise time, settling time, and peak response in Figure 4.27.

4.5 SLC Conclusions

A hybrid switching/linear controller (SLC) was developed to improve the time response over the linear controller. The initial phase of this controller saturates the control input to drive the phase plane trajectory to the switching line as rapidly as possible. At the switching line, the software state, e_I, is initialized to an appropriate value, and the LQ-servo controller controls the vehicle until the reference state is reached.

The SLC improved the time response over the LQ-servo controller, especially for large reference inputs. The peak overshoot and settling time were significantly decreased. The SLC was more capable at handling irregular initial states (e.g., a step from 5 to 10 degrees) because of its error integral initialization scheme. Additionally, it allowed the vehicle to track a 10 degree step command at Mach 5.3 and 50 km altitude, which was not possible with the LQ-servo controller. Finally, the SLC provided this flight condition with some measure of robustness to uncertainty in center of pressure location and control surface effectiveness. The SLC did not provide any robustness benefits in static margin or control effectiveness for the Mach 3.5/0 km altitude or Mach 6.3/20 km altitude cases.

This page intentionally left blank.

Chapter 5

Model Reference Adaptive Controller

The Linear Quadratic Servo controller developed in Chapter 3 performed well with perfect plant knowledge; however, performance was degraded with reduced knowledge of the aerodynamics. A model-reference adaptive controller (MRAC) was developed to exploit the performance of the nominal controller while maintaining flexibility in the face of plant uncertainty.

5.1 Theoretical Background

The author assumes the reader has a general understanding of Lyapunov stability and Lyapunov functions. The relevant definitions, theorems, and proofs relating to these topics can be found in the extensive literature on nonlinear systems (e.g., [21],[22]).

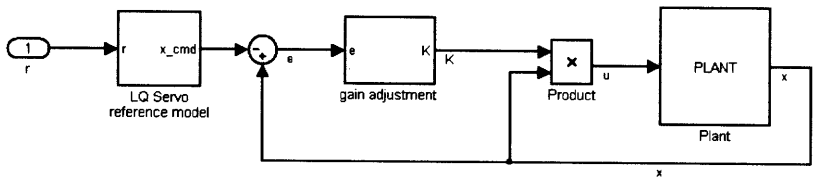

Figure 5.1: Model-Reference Adaptive Control Framework

The model reference control framework is pictured in Figure 5.1. The qualitative control strategy involves running a "reference" model that exhibits desired time-response characteristics. The reference states and plant states are compared to form an error vector. Ensuring the error dynamics have a stable equilibrium point at $\mathbf{e} = \mathbf{0}$ guarantees the plant will converge to the (favorable) reference model behavior after some transient. This stable error equilibrium is guaranteed by adjusting the gains according to dynamics that satisfy a Lyapunov function.

5.2 Adaptive Control Design

The initial adaptive control design chose δ_s as a fixed parameter, leaving the state differential equation in the form of Equation 3.12, and δ_a is the sole input. This

development follows that outlined in [23] and [24]. Assuming the control input is of form

$$\delta_a = -\hat{\mathbf{K}}^T\mathbf{x} + \hat{k_I}e_I \tag{5.1}$$

where e_I is defined in Equation 3.17, the plant can be modeled as

$$\dot{\mathbf{x}} = \mathbf{A}\mathbf{x} + \lambda\mathbf{B}\left(-\hat{\mathbf{K}}^T\mathbf{x} + \hat{k_I}e_I\right) \tag{5.2}$$

The matrix $\mathbf{A}$ is constant but not well-known, $\mathbf{B}$ is well-known, and λ is positive but unknown. This limit on λ allows a reduced control effectiveness (the nominal value for λ is 1), but does not allow control reversals.

The reference model is set as the nominal LQ-servo control with closed loop dynamics

$$\dot{\mathbf{x}}_{\text{ref}} = \mathbf{A}_{\text{ref}} + \mathbf{B}k_e e_I \tag{5.3}$$

where A_{ref} represents the nominal closed-loop dynamics

$$\mathbf{A}_{\text{ref}} = \mathbf{A}_{\text{nom}} - \mathbf{B}\mathbf{K}^T_{\text{LQservo}} \tag{5.4}$$

and k_e is the nominal LQ-servo gain on the error integral.

Forcing $\mathbf{e}$ (the error between the reference model and plant) to zero implies that the real plant converges to the (stable and well-performing) reference plant. Assuming there exist (unknown) constant gains $\mathbf{K}^*$ and k_I^* such that

$$\mathbf{A}_{\text{ref}} = \mathbf{A} - \lambda\mathbf{B}\mathbf{K}^{*T} \tag{5.5}$$

$$k_e = \lambda k_I^* \tag{5.6}$$

the error dynamics can be written as

$$\begin{aligned}\dot{\mathbf{e}} &= \dot{\mathbf{x}} - \dot{\mathbf{x}}_{\text{ref}} \\ &= \mathbf{A}\mathbf{x} - \mathbf{A}_{\text{ref}}\mathbf{x}_{\text{ref}} + \lambda\mathbf{B}\left(-\mathbf{K}^T\mathbf{x} + k_I e_I\right) - \mathbf{B}k_e e_I \\ &= \mathbf{A}_{\text{ref}}\mathbf{e} - \lambda\mathbf{B}\tilde{\mathbf{K}}^T\mathbf{x} + \lambda\mathbf{B}\tilde{k_I}e_I \end{aligned} \tag{5.7}$$

with

$$\begin{aligned}\tilde{\mathbf{K}} &= \hat{\mathbf{K}} - \mathbf{K}^* \\ \tilde{k_I} &= \hat{k_I} - k_I^*\end{aligned}$$

Choosing the positive-definite Lyapunov function

$$\mathcal{L} = \tfrac{1}{2}\mathbf{e}^T\mathbf{e} \tag{5.8}$$

gives

$$\dot{\mathcal{L}} = \mathbf{e}^T\mathbf{A}_{\text{ref}}\mathbf{e} + \mathbf{e}^T\left(-\lambda\mathbf{B}\tilde{\mathbf{K}}^T\mathbf{x} + \lambda\mathbf{B}\tilde{k_I}e_I\right) \tag{5.9}$$

The term $\mathbf{e}^T\mathbf{A}_{\text{ref}}\mathbf{e}$ is negative definite since the eigenvalues of $\mathbf{A}_{\text{ref}}$ are necessarily left of the $j\omega$ axis (see Equation 5.3), but the remainder of Equation 5.9 is not necessarily negative definite (or even zero). Consequently, the Lyapunov function must be augmented:

$$\mathcal{L} = \tfrac{1}{2}\left(\mathbf{e}^T\mathbf{e} + \lambda\tilde{\mathbf{K}}^T\mathbf{\Gamma}_x^{-1}\tilde{\mathbf{K}} + \lambda\Gamma_I^{-1}\tilde{k_I}^2\right) \tag{5.10}$$

where the adaptation rates, $\mathbf{\Gamma}_x$ and Γ_I, are positive definite (and thus their inverses are positive definite [25]). $\mathbf{\Gamma}_x$ is a diagonal matrix with nonzero terms on the main diagonal. Now,

$$\dot{\mathcal{L}} = \mathbf{e}^T\mathbf{A}_{\text{ref}}\mathbf{e} + \mathbf{e}^T\left(-\lambda\mathbf{B}\tilde{\mathbf{K}}^T\mathbf{x} + \lambda\mathbf{B}\tilde{k_I}e_I\right) + \lambda\tilde{\mathbf{K}}^T\mathbf{\Gamma}_x^{-1}\dot{\hat{\mathbf{K}}} + \lambda\Gamma_I^{-1}\tilde{k_I}\dot{\hat{k_I}} \tag{5.11}$$

To ensure 5.11 is negative definite, the adaptation law is chosen as

$$\dot{\hat{\mathbf{K}}} = \mathbf{e}^T \mathbf{B} \mathbf{\Gamma}_x x \tag{5.12}$$

$$\dot{\hat{k}}_I = -\mathbf{e}^T \mathbf{B} \Gamma_I e_I \tag{5.13}$$

5.3 Initial Results

The single input (δ_a) adaptive controller described in Section 5.3 fails to provide a significant benefit to the SRV robustness. Figure 5.2 compares the robustness to center of pressure location and control effectiveness for the LQ-servo controller (Chapter 3) and the adaptive controller. The adaptive controller provides an additional 3%

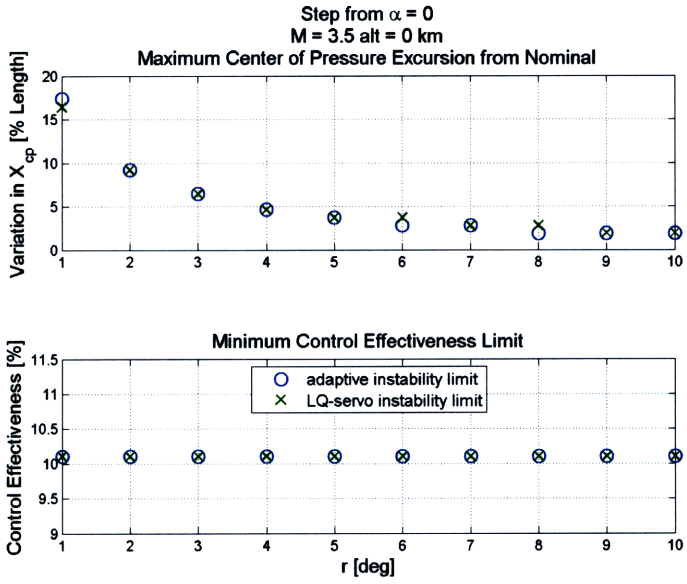

Figure 5.2: Robustness comparison of the MRAC and LQ-servo from $\alpha = 0$ deg for various reference commands, M = 3.5, 0 km altitude, $\delta_s = 8$ degrees, 1 MHz adaptation rate

of center of pressure robustness for the 1 degree step, but no additional robustness

at larger steps. Furthermore, the minimum allowable controller effectiveness is unaffected. The gains stabilize at steady-state values in the face of center of pressure uncertainty; however, the total gain variation is of the order 10^{-4} percent. Increasing the adaptation rate increases allowable center of pressure variation and thus greater gain variation, but the adaptation rate cannot be increased without bound. Processor speed, unmodeled structural modes, and unmodeled delays all limit the maximum adaptation rate that can be sucessfully implemented on an actual system.[21]

Control surface saturation limits the adaptive controller and LQ-servo alike. If both the adaptive and LQ-servo systems demand an asymmetric deflection outside the deflection bounds, tracking will be similarly limited. A more effective approach may be to control δ_s rather than fix it at the deflection determined in Chapter 3.

5.4 Dual-input Adaptive Control

In the presence of controller saturation, Equation 5.2 can be written as

$$\dot{\mathbf{x}} = \mathbf{A}\mathbf{x} + \lambda\mathbf{B}\left(\hat{\delta}_a + \Delta_a\right) \tag{5.14}$$

where $\hat{\delta}_a$ is the commanded control deflection and

$$\Delta_a = \delta_a - \hat{\delta}_a \tag{5.15}$$

Thus, Δ_a is nonzero when the commanded control deflection, $\hat{\delta}_a$, is outside the saturation limits. Alternately,

$$\delta_a = \delta_{a_{max}} \text{sat}\left(\frac{\hat{\delta}_a}{\delta_{a_{max}}}\right) \tag{5.16}$$

and

$$\text{sat}\phi = \begin{cases} \phi, & |\phi| \leq 1 \\ 1, & \phi > 1 \\ -1, & \phi < 1 \end{cases}$$

The single-input MRAC indicated control saturation hampered both LQ-servo and adaptive control of the SRV. Ajami, Hovakimyan, and Lavretsky employ the excess control, Δ_a, to modify the reference states in the presence of saturation.[24] For the SRV, it may be beneficial to use the excess control to manipulate the symmetric deflection.

The dual-input adaptive control sought to eliminate controller saturation; that is, $\Delta_a \rightarrow 0$. The dynamics of the excess control are simply

$$\dot{\Delta}_a = \dot{\delta}_a - \dot{\hat{\delta}}_a \tag{5.17}$$

Recalling the definitions of symmetric and asymmetric flap deflections (Equations 2.1 and 2.2) and the allowable range for each flap is [0,10] degrees gives

$$\delta_{a_{max}} = \begin{cases} 2\delta_s, & \delta_s \leq 5 \\ 2\left(10 - \delta_s\right), & \delta_s \geq 5 \end{cases} \tag{5.18}$$

and $-\delta_{a_{max}} = \delta_{a_{min}}$.

The obvious Lyapunov candidate function is

$$\mathcal{L} = \tfrac{1}{2}\Delta_a{}^2 \tag{5.19}$$

which is nonzero only when the excess control is nonzero.

Consider the case where $\Delta_a < 0$, which corresponds to $\hat{\delta}_a > \delta_{a_{max}}$. Then,

$$\dot{\Delta}_a = \dot{\delta}_{a_{max}} - \dot{\hat{\delta}}_a \tag{5.20}$$

Now consider the case where $\Delta_a > 0$; that is, $\hat{\delta}_a < -\delta_{a_{max}}$:

$$\dot{\Delta}_a = -\dot{\delta}_{a_{max}} - \dot{\hat{\delta}}_a \tag{5.21}$$

The time derivative of $\dot{\delta}_{a_{max}}$ can be expressed as

$$\dot{\delta}_{a_{max}} = \begin{cases} 2\dot{\delta}_s, & \delta_s < 5 \\ -2\dot{\delta}_s, & \delta_s > 5 \end{cases} \tag{5.22}$$

which is undefined at $\delta_s = 5$. To overcome this, defining $\delta_{a_{max}} = 0$ at $\delta_s = 5$ gives

$$\dot{\delta}_{a_{max}} = 2\dot{\delta}_s \text{sign}\,(5 - \delta_s) \tag{5.23}$$

Then the time derivative of the Lyapunov candidate function in Equation 5.19 is

$$\dot{\mathcal{L}} = 2\dot{\delta}_s \left|\Delta_a\right| \text{sign}\,(\delta_s - 5) - \Delta_a \dot{\hat{\delta}}_a \tag{5.24}$$

To ensure Equation 5.24 is negative definite, the obvious choice for $\dot{\delta}_s$ is

$$\dot{\delta}_s = -k_s \left|\Delta_a\right| \text{sign}\,(\delta_s - 5) + \tfrac{1}{2}\dot{\hat{\delta}}_a \text{sign}\,(\delta_s - 5)\,\text{sign}\Delta_a \tag{5.25}$$

where $k_s > 0$.

Inspection of Equation 5.25 reveals a singularity at $\delta_s = 5$ degrees that is stable only when Δ_a and $\dot{\hat{\delta}}_a$ have the same sign. This is satisfied in two cases:

- δ_a is at the negative saturation limit AND the commanded deflection is increasing
- δ_a is at the positive saturation limit AND the commanded deflection is decreasing

Obviously, these conditions are not guaranteed. Furthermore, the sign $(\delta_s - 5)$ terms in Equation 5.25 ensure the symmetric deflections cannot move upon reaching 5 degrees.

In the future, it may be possible to augment the Lyapunov function in Equation 5.19 with additional terms to remove the singularity at $\delta_s = 5$.

5.5 Adaptive Control Conclusions

A model-reference adaptive controller was developed to control the asymmetric deflection while maintaining a fixed symmetric deflection. This single-input, single-output system approach paralleled the approach developed in the previous chapters. The adaptive control failed to provide any additional appreciable robustness over the baseline LQ-servo controller of Chapter 3. Small gains in robustness to center of pressure variation were demonstrated for small reference commands and clock speeds

of 1 MHz. The control saturation effects that limited the linear controller likewise hampered the effectiveness of the adaptive controller.

In an initial attempt to alleviate some saturation problems, an additional adaptive controller was designed to drive the control saturation to zero. The control scheme presented above was unsuccessful at ensuring stability, but a similar approach may prove useful in future work. The major difficulty in designing such a dual-input adaptive controller is the choice of a satisfactory Lyapunov function candidate and associated control strategy.

The dual-input adaptive controller presented treated the control of the asymmetric deflection, δ_a, as independent of the symmetric deflection, δ_s. Then, δ_s was modulated to alleviate the saturation on δ_a. A more suitable approach may be to treat both inputs simultaneously.

Chapter 6

Conclusions

6.1 Summary

The primary objective of this research was to design an angle of attack tracking controller for a variable-stability slender reentry vehicle (SRV). The vehicle was controlled by two flaps mounted near the base of the 2-dimensional, wedge-shaped (or 3-dimensional, conical) vehicle. These flaps altered both the pitch static stability and trim characteristics of the vehicle through two separate control inputs: symmetric flap deflection and asymmetric flap deflection, respectively. This flap controlled configuration had significant control deflection limits that introduced nonlinearity to the system. Additionally, the symmetric deflection input entered the equation of motion nonlinearly and coupled with the angle of attack. In practice, the aerodynamic data of the SRV may be poorly known. Specifically, this effort assumed the center of pressure location may be poorly known, control surfaces may experience ablation

and reduced effectiveness, and asymmetric ablation may induce a nonzero pitching acceleration (specific moment) on the vehicle.

A linear quadratic servo (LQ-servo) tracking controller was designed that augmented the two pitch states (angle of attack and pitch rate) with the integrated tracking error. Three design points along a typical ballistic reentry trajectory were selected for controller analysis: Mach 5.3 and 50 km altitude, Mach 6.3 and 20 km altitude, and Mach 3.5 and 0 km altitude. The LQ-servo was selected because it enjoys guaranteed stability and robustness margins in the absence of nonlinearities. For whole-number symmetric deflections from 2 degrees to 8 degrees, the LQ-servo was designed to meet a specified rise time and gain margin. Robustness to center of pressure variation, reduced control effectiveness, and unmodeled pitch accelerations were determined. The addition of a first order actuator reduced vehicle tracking performance when vehicle dynamics were relatively fast (high dynamic pressures). A lead compensator demonstrated the ability to alleviate some of the actuator-caused performance degradation. Robustness to center of pressure variation at high dynamic pressures was correlated with the linear instability limits, while nonlinear control saturation effects limited the robustness at low dynamic pressures or large reference commands. Additionally, low dynamic pressure reduced the the system tolerance for less effective controls and external pitch accelerations. A symmetric deflection was selected at each flight condition that maximized robustness and demonstrated favorable time responses at both 1 degree and 10 degree step commands in reference angle of attack.

A hybrid switching linear controller (SLC) was designed to exploit the favorable performance of the LQ-servo but improve the time response and robust performance, especially for large reference commands. The LQ-servo phase plane was analyzed for regions of satisfactory and unsatisfactory performance. A region of satisfactory, unsaturated LQ-servo performance was determined, and a linear initialization of the integrated tracking error was designed along this region. Outside the LQ-servo

region, a saturated controller employs the maximum deflection to drive the phase plane trajectory to the LQ-servo region. The SLC reduced settling times, especially for large reference commands and nonzero initial angles of attack. The SLC did not provide additional robustness for the Mach 3.5, 0 km altitude or Mach 6.3, 20 km altitude case; however, the SLC did allow large reference commands to be tracked at Mach 5.3, 50 km altitude that were unstable with the LQ-servo controller.

With the goal of improving robustness, a model-reference adaptive controller (MRAC) was developed. The MRAC attempted to match the performance of the nominal system controlled by the LQ-servo controller. The adaptive controller did not provide additional robustness over the LQ-servo controller because control saturation effects continued to limit performance. An initial attempt to design a dual-input adaptive control for both the symmetric and asymmetric deflections was described; however, the Lyapunov candidate function and control scheme did not guarantee stability for all symmetric deflections.

6.2 Recommendations Future Research

The SLC was dependent on accurate center of pressure knowledge (up to 2% of the length for large reference commands). In reality, the static margin is not likely to be known *a priori* within these margins. Consequently, on-line estimation of the static margin may be necessary. A small angle of attack oscillation command may be useful in estimation of the static margin. With a more accurate static margin, the control strategy (LQ-servo gains, switching curve, etc.) may be adjusted on-line as static margin knowledge improves.

An adaptive controller may be useful in adjusting to plant uncertainty, but the single-input controller developed was still limited to flight profile-scheduled symmetric deflections. Furthermore, the control saturations still limited the adaptive controller. It may be possible to design an adaptive controller that manipulates the symmetric deflection based on control saturation. The dual-input scheme similar to that presented in Section 5.4 can potentially provide a means to control both symmetric and asymmetric deflections during reference-command tracking. On the other hand, it may be beneficial to design a controller that simultaneously controls both δ_s and δ_a, rather than employing independent adaptations. An adaptation on the SLC switching line and integrated tracking error initialization may provide additional robustness.

Bibliography

[1] Bertin, J. J., *Hypersonic Aerothermodynamics*, AIAA, Washington D.C., 1994.

[2] Kolodziej, P., Bowles, J. V., and Roberts, C., "Optimizing hypersonic sharp body concepts from a thermal protection system perspective," *AIAA International Space Planes and Hypersonic Systems and Technologies Conference*, April 27–30 1998, pp. 556–571.

[3] Cavallo, A., De Maria, G., and Ferrara, F., "Attitude control for low lift/drag re-entry vehicles," *Journal of Guidance, Control, and Dynamics*, Vol. 19, No. 4, 1965, pp. 816–822.

[4] Dukeman, G., "Profile-Following Entry Guidance Using Linear Quadratic Regulator Theory," *AIAA Guidance, Navigation, and Control Conference and Exhibit*, August 2002.

[5] Bibeau, R. and Rubinstein, D., "Trajectory optimization for a fixed-trim reentry vehicle using direct collocation and nonlinear programming," *AIAA Guidance, Navigation, and Control Conference and Exhibit*, August 2000.

[6] Juliana, S., Chu, Q., Mulder, A., and van Baten, T., "Nonlinear Flight Control for Re-entry Flight Vehicle," *55th International Astronautical Congress*, August 2004.

[7] Mooij, E., Mease, K., and Benito, J., "Robust Re-Entry Guidance and Control System Design and Analysis," *AIAA Guidance, Navigation, and Control Conference and Exhibit*, August 2007.

[8] Lu, P., "Entry Guidance and Trajectory Control for Reusable Launch Vehicle," *Journal of Guidance, Control, and Dynamics*, Vol. 20, No. 1, 1965, pp. 143–149.

[9] Shtessel, Y., Tournes, C., and Krupp, D., "Reusable launch vehicle control in sliding modes," *AIAA Guidance, Navigation, and Control Conference*, New Orleans, LA, August 11–13 1997.

[10] Burkhardt, J. and Schoettle, U. M., "Flight performance and control aspects of a semi-ballistic reentry capsule," *Atmospheric Flight Mechanics Conference*, July 29–31 1996.

[11] Casey, J. J., "Influence of ablation on the dynamics of slender re-entry configurations," *Journal of Spacecraft and Rockets*, Vol. 2, No. 1, 1965, pp. 106–108.

[12] Bertin, J. J., *Aerodynamics for Engineers*, Prentice Hall, Upper Saddle River, NJ, 4th ed., 2002.

[13] Chamitoff, G., *Robust Intelligent Flight Control for Hypersonic Vehicles*, Ph.D. thesis, Massachusetts Institute of Technology, 1992.

[14] Etkin, B., *Dynamics of Atmospheric Flight*, John Wiley & Sons, Toronto, Ontario, 1972.

[15] Shampine, L. F. and Reichelt, M. W., "The MATLAB ODE Suite," *SIAM Journal on Scientific Computing*, Vol. 18, 1997, pp. 1–22.

[16] Shampine, L. F., Reichelt, M. W., and Kierzenka, J., "Solving Index-1 DAEs in MATLAB and Simulink," *SIAM Review*, Vol. 41, 1999, pp. 538–552.

[17] Arthur E. Bryson, J. and Ho, Y.-C., *Applied Optimal control: Optimization, Estimation, and Control*, Hemisphere Publishing Corporation, Washington, D.C., 1975.

[18] Kirk, D. E., *Optimal Control Theory: An Introduction*, Dover, Mineola, NY, 1998.

[19] Stengel, R. F., *Optimal Control and Estimation*, Dover, Mineola, NY, 1994.

[20] Yechout, T., Morris, S., Bossert, D., and Hallgren, W., *Introduction to Aircraft Flight Mechanics: Performance, Static Stability, Dynamic Stability, and Calssical Feedback Control*, AIAA, Reston, VA, 2003.

[21] Slotine, J.-J. E. and Li, W., *Applied Nonlinear Control*, Prentice Hall, Upper Saddle River, NJ, 1991.

[22] Vidyasagar, M., *Nonlinear Systems Analysis*, SIAM Publications, Philadelphia, 2nd ed., 2002.

[23] Lavretsky, E. and Hovakimyan, N., "Stable Adaptation in the Presence of Actuator Constraints with Flight Control Applications," *Journal of Guidance, Control, and Dynamics*, Vol. 30, No. 2, 2007, pp. 337–345.

[24] Ajami, A., Hovakimyan, N., and Lavretsky, E., "Design examples: Adaptive Tracking Control in the Presence of Input Constraints for a Fighter Aircraft and a Generic Missile," *AIAA Guidance, Navigation, and Control Conference*, San Francisco, CA, August 15–18 200.

[25] Strang, G., *Applied Linear Algebra*, Wellesley-Cambridge Press, Welleslye, MA, 1986.

[26] Brandt, S., Stiles, R., Bertin, J., and Whitford, R., *Introduction to Aeronautics: A Design Perspective*, AIAA, Reston, VA, 1997.

[27] Hillje, E. R., "Entry Aerodynamics at Lunar Return Conditions," NASA Technical Note TN D-5399, NASA, October 1969.

[28] Wingrove, R., "Trajectory Control Problems in Planetary Entry of Manned Vehicles," *Journal of Spacecraft and Rockets*, Vol. 2, No. 6, 1965, pp. 883–886.

This page intentionally left blank.

Appendix A

Additional Graphs

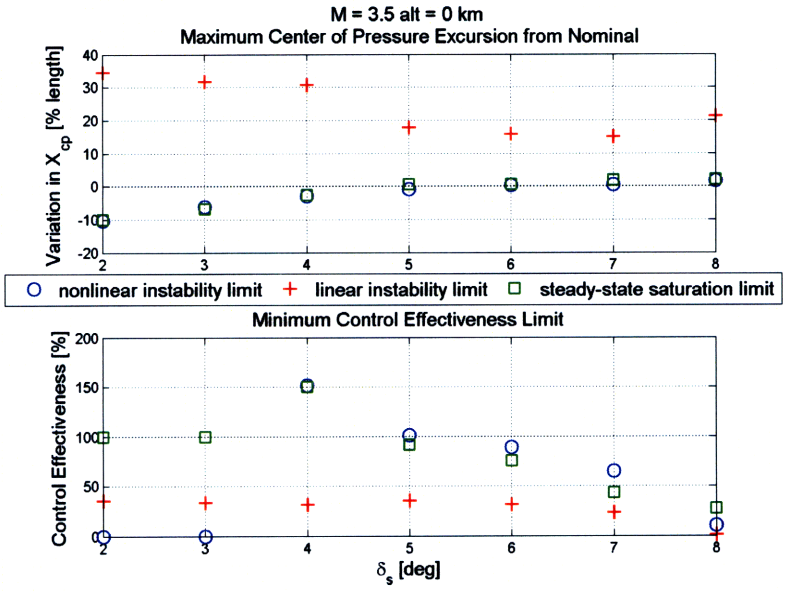

Figure A.1: Allowable variation in center of pressure location and reduction in control effectiveness, step command from 0 to 10 degrees, Mach 3.5, 0 km altitude

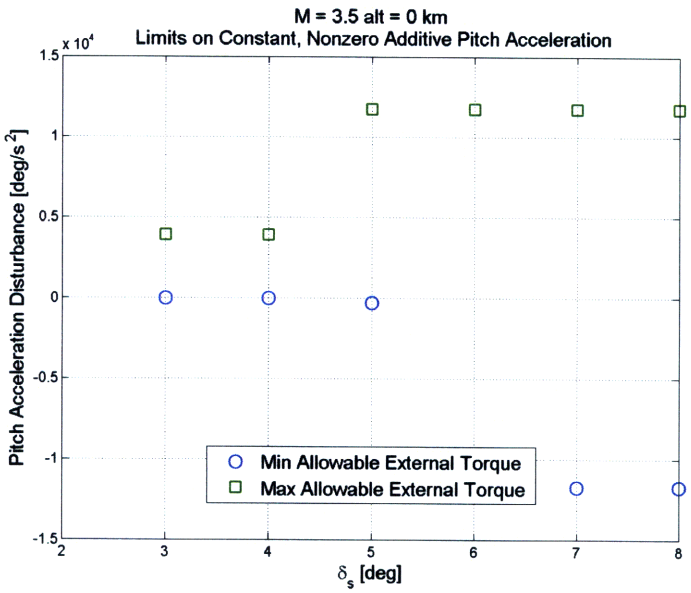

Figure A.2: Robustness to external pitch acceleration, step command from 0 to 10 degrees, Mach 3.5, 0 km altitude

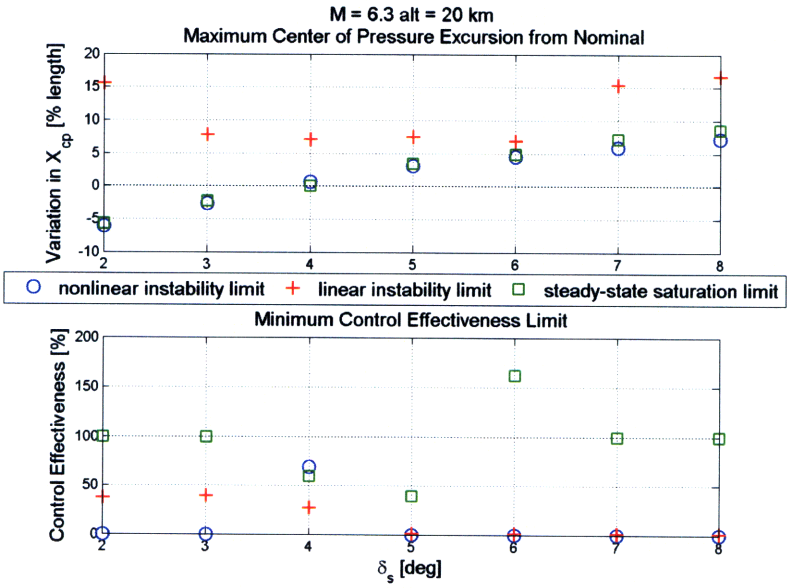

Figure A.3: Allowable variation in center of pressure location and reduction in control effectiveness, step command from 0 to 10 degrees, Mach 6.3, 20 km altitude

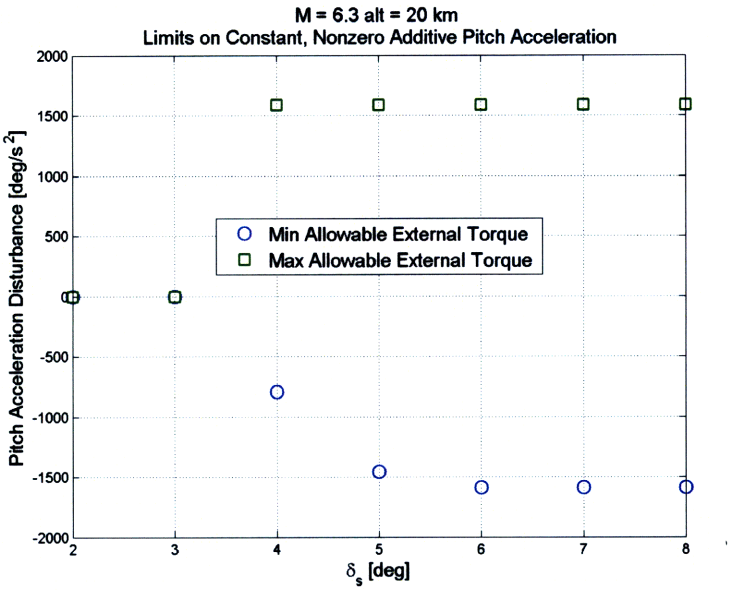

Figure A.4: Robustness to external pitch acceleration, step command from 0 to 10 degrees, Mach 6.3, 20 km altitude

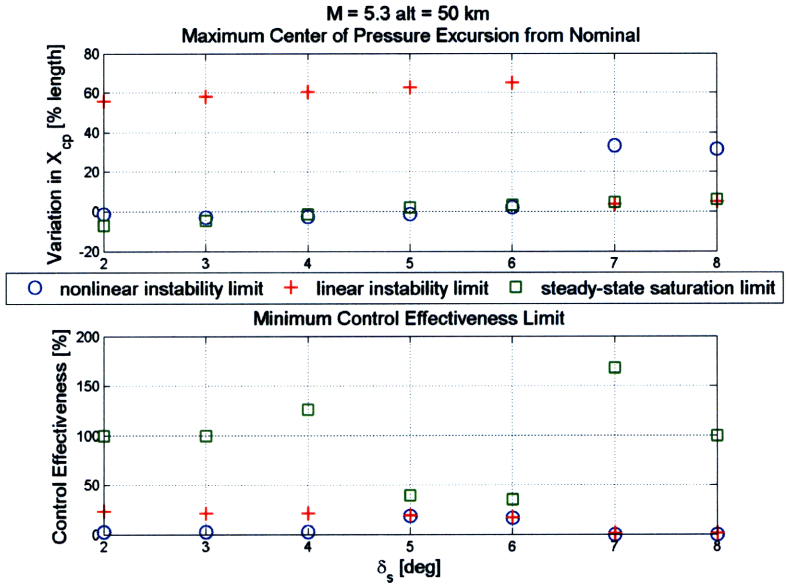

Figure A.5: Allowable variation in center of pressure location and reduction in control effectiveness, step command from 0 to 10 degrees, Mach 5.3, 50 km altitude

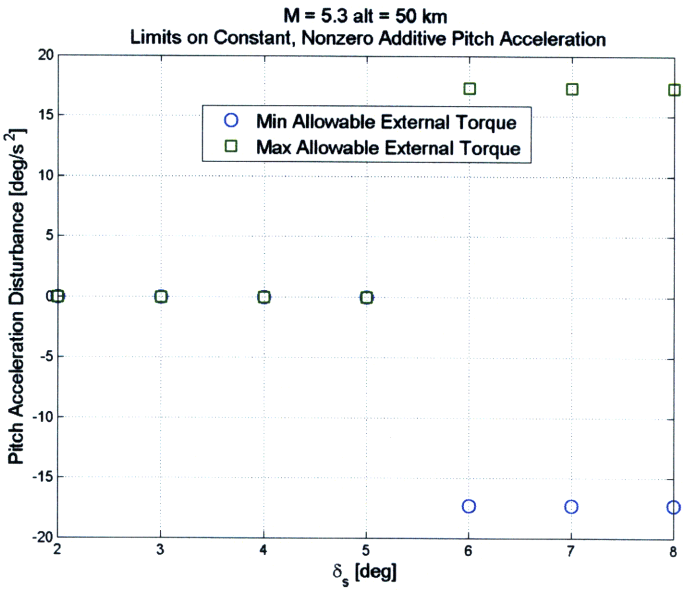

Figure A.6: Robustness to external pitch acceleration, step command from 0 to 10 degrees, Mach 5.3, 50 km altitude

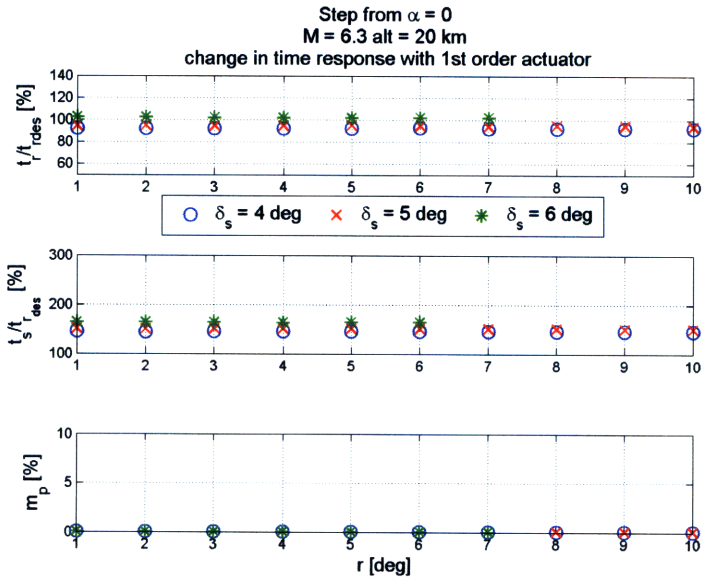

Figure A.7: Time response characteristics for step commands from 0 degrees, Mach 6.3, 20 km altitude, 1st order actuator Modeled

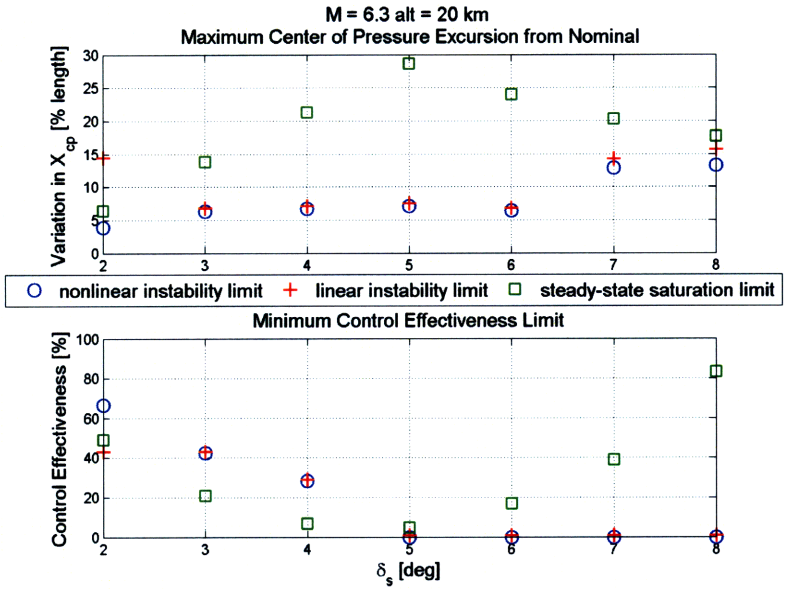

Figure A.8: Allowable variation in center of pressure location and reduction in control effectiveness, step command from 0 to 1 degree,Mach 6.3, 20 km altitude, 1st order actuator modeled

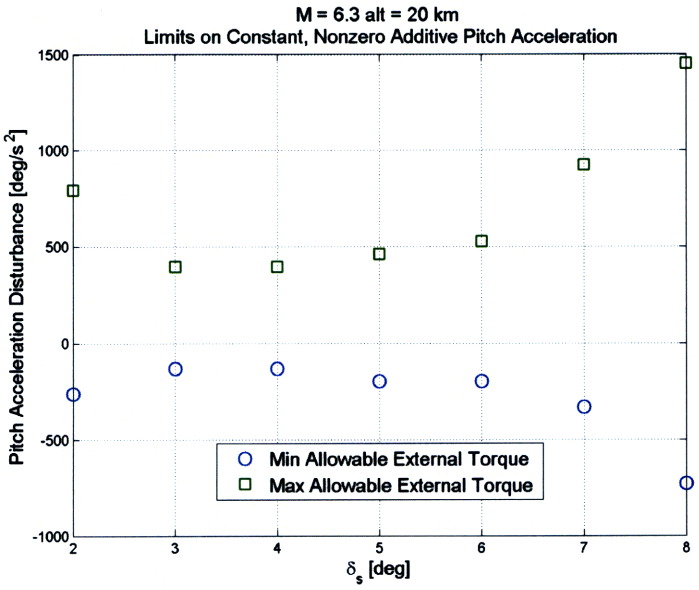

Figure A.9: Robustness to external pitch acceleration, step command from 0 to 1 degree, Mach 6.3, 20 km altitude,1st order actuator modeled

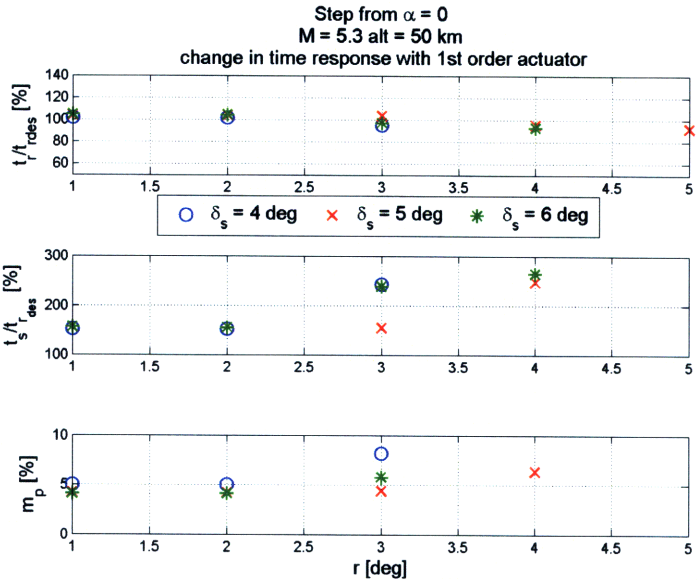

Figure A.10: Time response characteristics for step commands from 0 degrees, Mach 5.3, 50 km altitude, 1st order actuator Modeled

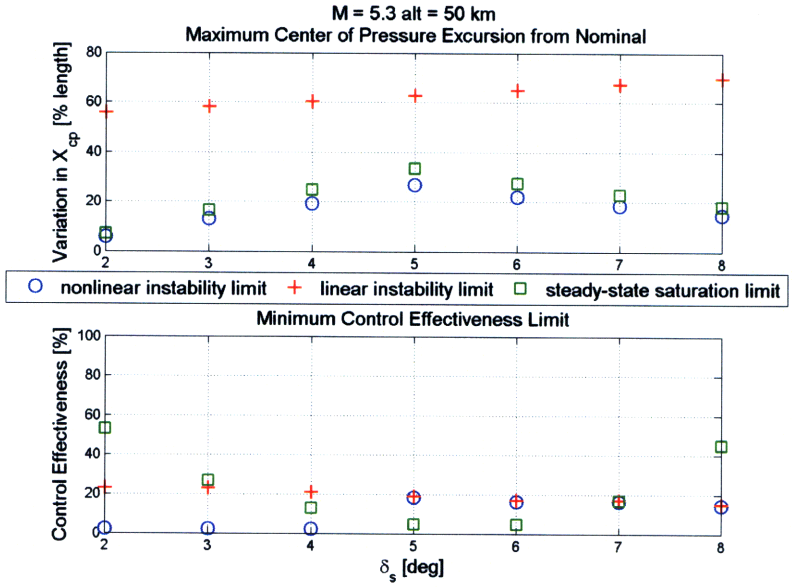

Figure A.11: Allowable variation in center of pressure location and reduction in control effectiveness, step command from 0 to 1 degree, Mach 5.3, 50 km altitude, 1st order actuator modeled

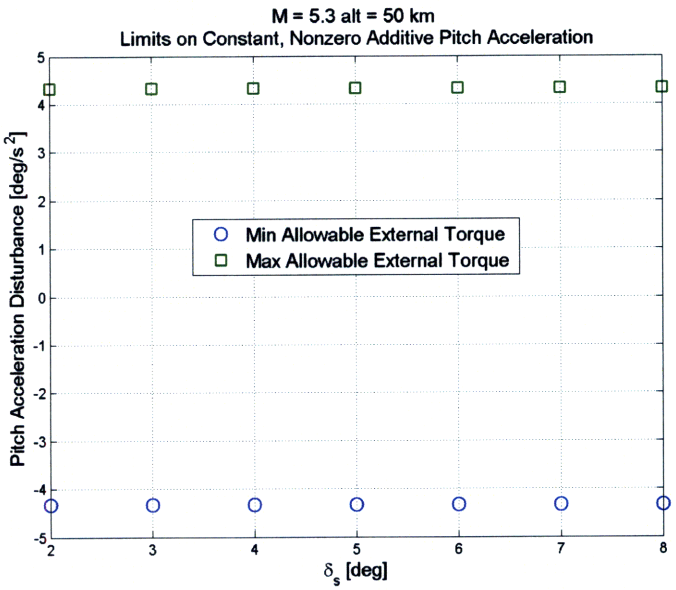

Figure A.12: Robustness to external pitch acceleration, step command from 0 to 1 degree, Mach 5.3, 50 km altitude, 1st order actuator modeled